THE HONG KONG
POLYTECHNIC UNIVERSITY
香港理工大學
Pao Yue-kong Library
包玉剛圖書館

Copyright Undertaking

This thesis is protected by copyright, with all rights reserved.

By reading and using the thesis, the reader understands and agrees to the following terms:

1. The reader will abide by the rules and legal ordinances governing copyright regarding the use of the thesis.
2. The reader will use the thesis for the purpose of research or private study only and not for distribution or further reproduction or any other purpose.
3. The reader agrees to indemnify and hold the University harmless from and against any loss, damage, cost, liability or expenses arising from copyright infringement or unauthorized usage.

IMPORTANT

If you have reasons to believe that any materials in this thesis are deemed not suitable to be distributed in this form, or a copyright owner having difficulty with the material being included in our database, please contact lbsys@polyu.edu.hk providing details. The Library will look into your claim and consider taking remedial action upon receipt of the written requests.

Pao Yue-kong Library, The Hong Kong Polytechnic University, Hung Hom, Kowloon, Hong Kong

http://www.lib.polyu.edu.hk

MULTISCALE MODELLING APPROACHES FOR ESTIMATING WIND DISTRIBUTIONS AT PEDESTRIAN LEVEL IN REAL URBAN ENVIRONMENTS

WANG JUE

PhD

The Hong Kong Polytechnic University

2025

The Hong Kong Polytechnic University
Department of Building Environment and Energy Engineering

Multiscale Modelling Approaches for Estimating Wind Distributions at Pedestrian Level in Real Urban Environments

WANG Jue

A thesis submitted in partial fulfillment of the requirements for the Degree of Doctor of Philosophy

February 2025

CERTIFICATE OF ORIGINALITY

I hereby declare that this thesis is my own work and that, to the best of my knowledge and belief, it reproduces no material previously published or written, nor material that has been accepted for the award of any other degree or diploma, except where due acknowledgement has been made in the text.

(Signed)

WANG Jue (Name of Student)

Department of Building Environment and Energy Engineering
The Hong Kong Polytechnic University
Hong Kong, China
February 2025

ABSTRACT

Abstract of the thesis entitled: Multiscale Modelling Approaches for Estimating Wind Distributions at Pedestrian Level in Real Urban Environments

Submitted by WANG Jue

For the Degree of: Doctor of Philosophy

at The Hong Kong Polytechnic University in February 2025.

Accurately estimating wind distributions at pedestrian level in real urban environments is crucial for predicting pollutant dispersion within street canyons, assessing public exposure levels, and evaluating pedestrian comfort. Field measurements can be conducted to capture pedestrian-level wind conditions. However, experimental methods provide data only at limited sampling points, restricting the ability to obtain comprehensive spatial information of urban wind distributions. Therefore, this study aimed to apply multiscale modelling by combining the Weather Research and Forecasting (WRF) model with computational fluid dynamics (CFD) methods to accurately calculate detailed wind distributions at the pedestrian level in real urban environments.

To calculate pedestrian-level wind distributions in real urban environments using the multiscale modelling approaches, it is crucial to investigate the applicability of various turbulence models used in CFD for outdoor wind simulations. In this investigation, the performance of steady-state and unsteady-state Reynolds-averaged Navier-Stokes simulation (SRANS/URANS) and large-eddy simulation (LES) were evaluated in calculating airflow and pollutant dispersion in street canyons with generic and real urban layouts. For each layout, wind tunnel experiments with measured wind speed and pollutant concentration were available as benchmarks. In addition, instantaneous concentration fields were analyzed to assess the transient models. The results showed that in the generic urban layout, URANS with the SST $k-\omega$ model captured

the large-scale fluctuations, while instantaneous results from URANS with the SST model did not change over time in the real urban layout. In both generic and real urban layouts, the RNG $k-\varepsilon$ model and SST $k-\omega$ model provided similar results for time-averaged wind speed and concentration distributions in SRANS and URANS simulations. Among all the selected RANS models, SRANS/URANS with the SST $k-\omega$ model showed best agreement with measured data in calculating wind speed. LES performed best in calculating wind speed and pollutant dispersion, but it was the most time-consuming model.

Apart from the turbulence modelling approaches, setting appropriate inflow wind profiles for CFD simulations is also important for predicting the wind distributions in real urban environments. Wind profiles within the atmospheric boundary layer are significantly affected by local atmosphere circulation and diurnal variation. The WRF model is a powerful mesoscale weather prediction model that can be used to provide realistic inflow boundary conditions for CFD simulations. To investigate the accuracy and applicability of a combined WRF and CityFFD method (WRF-CityFFD) for calculating urban wind distributions, this study first validated the WRF and CFD models and then used the validated models in WRF-CityFFD to calculate the wind distributions in the Kowloon district of Hong Kong within an area of $3.5\ \text{km} \times 2.4\ \text{km}$. The wind speed data at two weather stations were used as a benchmark. To evaluate the performance WRF-CityFFD, a comparison with CityFFD using inflow boundary conditions derived from a commonly used semi-empirical method (semi-empirical-CityFFD) was conducted. In this method, power-law wind profiles were used as the inflow wind profiles for CityFFD simulations. The results showed that, at KP and HKO stations, WRF-CityFFD achieved lower RMSEs (1.31 and 1.26 m/s) compared to 2.24 and 1.50 m/s for the semi-empirical approach. Thus, WRF-CityFFD performed better than semi-empirical-CityFFD in in calculating wind speed in urban microclimates. Moreover, WRF provided more accurate wind profiles in coastal areas with onshore winds, indicating such locations are more suitable for defining inflow boundaries in the combined WRF-CityFFD method. This combined method can help improve the model's ability to reproduce urban wind patterns, which is essential for applications such as urban ventilation assessment, pollutant dispersion modelling, and the evaluation of outdoor comfort.

Although the potential of the combined WRF and CFD method for urban wind simulations has been preliminarily demonstrated, previous investigations indicate that mesoscale models such

as WRF simulations are not sufficiently precise to predict wind profiles in built-up areas, and existing improvement methods remain computationally expensive and time-consuming. To improve the accuracy and efficiency of estimating wind profiles in built-up areas using WRF simulations, this study proposed a method that combines WRF with a porosity model. WRF provides the wind profile at the urban edge, and the porosity model calculates the airflow pressure drop across the selected urban area using a parametrized urban layout. The urban wind profile is then analytically determined with the momentum integral method. The performance of the proposed method was first evaluated in three generic urban layouts, with validated CFD simulations used as benchmarks. The proposed method was then applied in a real urban layout to demonstrate its performance, and the Kowloon district of Hong Kong, with an area of $2{,}350\ \mathrm{m} \times 643\ \mathrm{m}$, was selected as the target area. The wind profile measured with a radiosonde in the same region was used as a benchmark, and the WRF-calculated wind profile in the built-up area was also evaluated for comparison. The results showed that the method accurately estimated wind profiles in the generic urban layouts. In the real urban layout, the proposed method estimated the urban wind profile reasonably well in the densely built-up area with complex building configurations and performed better than WRF.

Based on the above investigations, a multiscale modelling approach was proposed by this study. To further assess the performance of the proposed approach in predicting pedestrian-level wind conditions, wind profiles estimated by the combined WRF and porosity model were used as inflow boundary conditions for CFD simulations. This implementation is hereafter referred to as the analytical-inlet-CFD method. To assess the accuracy of this multiscale approach, a public housing estate covering an area of $578\ m \times 560\ m$ was selected as the target area, and field measurements were conducted to collect pedestrian-level wind data in this real urban environment. The measured data then served as the benchmark for evaluating the accuracy of the analytical-inlet-CFD for outdoor wind simulations. Additionally, results from CFD with inflow boundary conditions directly extracted from WRF outputs (WRF-inlet-CFD) were also analyzed for comparison. The results showed that analytical-inlet-CFD performed better than WRF-inlet-CFD in calculating pedestrian-level wind distributions in real urban environments.

Overall, this thesis systematically evaluated the combined WRF–CFD method for calculating wind distributions in real urban environments and identified its limitations in accurately predicting wind profiles within densely built-up areas. To address these issues, an analytical

method combined WRF and a porosity model was proposed to improve the estimation of inflow wind profiles in urban areas. The resulting multiscale modelling approach incorporates mesoscale WRF simulations, analytical wind profile estimation, and CFD modelling. To assess the performance of the proposed approach, field measurements were conducted in a public housing estate to collect pedestrian-level wind data, which served as benchmark for evaluation of simulations. The results showed that the proposed approach improved both accuracy and computational efficiency compared to conventional methods, providing a reliable tool for calculating urban wind distributions in real urban environment, with further implications for pollutant dispersion modelling and pedestrian thermal comfort assessment.

LIST OF PUBLICATIONS

Peer Reviewed Journal Papers

- **J. Wang**, L. (Leon) Wang, R. You, Evaluating a combined WRF and CityFFD method for calculating urban wind distributions, *Building and Environment*. 234 (2023) 110205. https://doi.org/10.1016/j.buildenv.2023.110205.

- **J. Wang**, R. You, Evaluating different categories of turbulence models for calculating air pollutant dispersion in street canyons with generic and real urban layouts, J. Wind *Journal of Wind Engineering and Industrial Aerodynamics*. 255 (2024) 105948. https://doi.org/10.1016/j.jweia.2024.105948.

- **J. Wang**, R. You, Analytical prediction of urban wind profile in built-up areas using a combined method of WRF and a porosity model, Submitted to *Urban Climate*, under review.

- **J. Wang**, W. Wang, Y. Hou, J. Niu, R. You, Applying a combined analytical model and CFD method for calculating pedestrian-level wind distributions in real urban environments with field measurements as the benchmark, under preparation.

Conference Papers

- **J. Wang**, L. (Leon) Wang, R. You, A combined WRF and CityFFD method for calculating urban wind fields in a high-density city, 11th international conference on indoor air quality, ventilation & energy conservation in buildings (IAQVEC 2023). May 20-23, Tokyo, Japan.

- **J. Wang**, R. You, Evaluation of different categories of turbulence models for calculating air pollutant dispersion in real urban layout, 18th Conference of the

International Society of Indoor Air Quality and Climate, INDOOR AIR 2024 (IA2024). July 7-11, Honolulu, Hawaii.

- **J. Wang**, R. You, Estimation of urban wind profiles in built-up areas from GIS and WRF with a porosity model, Healthy Buildings Europe 2025 (HB2025). June 8-12, Reykjavik, Iceland.

- **J. Wang**, R. You, Pedestrian-level wind distributions simulation using an integrated method of WRF, GIS, and CFD in real urban environments (ICUC12). July 7-11, 2025, Rotterdam, Netherlands.

ACKNOWLEDGEMENTS

First and foremost, I would like to express my deepest gratitude to my supervisor, Prof. Ruoyu You, for her invaluable academic guidance and unwavering support throughout my research journey. Beyond academia, her care and encouragement in my personal life have provided me with immense comfort and strength during challenging times. I would also like to extend my thanks to Prof. Liangzhu Leon Wang and Prof. Jianlei Niu for their insightful suggestions and constant support in my research.

Gratitude is owed to the friends whose companionship made this journey more bearable and fulfilling. Thanks to Dr. Yichen Yu for providing invaluable support during the experimental work. Special appreciation goes to Xi Li, whose companionship during the early days in Hong Kong helped navigate the difficult period of Covid-19. Gratitude is also owed for teaching countless play card games and inviting me over for hotpot at her home. We shared so many unforgettable moments that brought warmth and joy during challenging times. Yunge Hou deserves heartfelt thanks for patiently teaching mesh generation techniques and offering timely assistance whenever issues arose. Thanks to Dr. Yiding Zhou for providing useful advice that greatly benefited the research. Thanks to Houzhi Wang for assembling my computer, and thanks to Rui Zhao for engaging in in-depth discussions about CFD model setups. Thanks are also extended to Wei Wang for always being a reliable gaming companion. Thanks to Dharma for providing constant support, especially during moments of difficulty. Appreciation is also extended to Jie Liang, Xuan Feng, and all friends in ZS869, for sharing snacks and souvenirs from around the world.

To friends from afar, their unwavering support has been invaluable. Thanks to Dr. Yuhao Guo for always being there to listen to late-night ramblings, providing a comforting presence despite the distance. Thanks to Zirui Xu for always sharing the latest gossip, bringing color and liveliness to an otherwise monotonous research life. Thanks to Shanshan Hou showed heartfelt concern for both research and well-being, even taking time from her wedding to offer words of encouragement. Thanks to Chenxi Wu for brightening my days by sharing beautiful sceneries, offering a window into distant places. Special acknowledgment goes to Xinyu Zhao, an online friend of over ten years, whose steadfast companionship and daily support have been a pillar

of strength. The emotional support and encouragement from all of these friends have made it possible to navigate this challenging period with resilience.

Lastly, the deepest appreciation goes to my parents, Jianping Wang and Changqing Wang, whose unconditional love, encouragement, and belief have been the foundation of strength. Their unwavering support has guided every step of this journey. I would also like to express my heartfelt gratitude to my beloved, Minqi Lin, whose patience, understanding, and constant encouragement have been an anchor during the most challenging times. Together, we navigated this challenging period, and it is hoped that in the days to come, we will continue to move forward hand in hand.

TABLE OF CONTENTS

LIST OF TABLES

LIST OF FIGURES

NOMENCLATURE

Abbreviations

IPCC	Intergovernmental Panel on Climate Change
GBD	Global Burden of Disease Study
CFD	Computational fluid dynamics
WRF	Weather Research and Forecasting model
SRANS	Steady-state Reynolds-averaged Navier-Stokes simulation
URANS	Unsteady-state Reynolds-averaged Navier-Stokes simulation
LES	Large-eddy simulation
TKE	Turbulence kinetic energy
SGS	Subgrid scale
ABL	Atmospheric boundary layer
TKE	Turbulence kinetic energy
CFL	Courant–Friedrichs–Lewy
FAC2	Friction of the prediction within a factor of 2 of the observations
NMSE	Normalized mean square error
ITGT	Inflow turbulence generation technique
LSM	Noah land surface model
UCM	Urban canopy model
SF	Star Ferry
SOD	Shell Oil Depot
HKO	Hong Kong Observatory
KP	King’s Park
KT	Kai Tak
MBE	Mean bias error
RMSE	Root mean square error
MOST	Monin-Obukhov similarity theory
UBL	Urban boundary layer

Variables

$\bar{u}$	Mean velocity $[m/s]$
u'	Fluctuating velocity $[m/s]$
$\bar{p}$	Mean pressure [Pa]
ρ	Density $[kg/m^3]$
υ	Viscosity $[N \cdot s/m^2]$
t	Time [s]
k	Turbulence kinetic energy $[m^2/s^2]$
ε, ω	Dissipation rate $[m^2/s^3]$, $[s^{-1}]$
υ_t	Turbulent kinematic viscosity $[N \cdot s/m^2]$
P_k	Production term of k $[N/s \cdot m^2]$
τ^s	Sub-grid stress $[N/m^2]$
$\overline{S}$	Large-scale strain rate
Δ_{sgs}	Grid size that defines the sub-grid length scale
$\Delta x, \Delta y, \Delta z$	Discrete lengths in the x, y, and z directions, respectively
C	pollutant concentration
$\mathbf{V}$	Velocity vector $[m/s]$
D_c	Molecular diffusion coefficient $[m^2/s]$
Sc_t	Turbulent Schmidt number
t^*	Time required for the airflow to pass through the domain once
u^*	Friction velocity $[m/s]$
z_0	Aerodynamic roughness length [m]
κ	Von Karman constant
c^*	Normalized concentration
c	Simulated gas concentration [ppm]
c_0	Reference concentration of tracer gas [ppm]
Q_{gas}	Emission rate of tracer gas $[m^3/s]$
H_{ref}	Reference height of each case [m]
u_{ref}	Velocity at the reference height $[m/s]$
M_i	Measured results
P_i	Predicted results
N	Number of sampling points

T	Temperature [K]
P	Pressure [Pa]
Re	dimensionless Reynolds number
Gr	Grashof number
Pr	Prandtl number
ϑ_t	Turbulent thermal diffusivity $[m^2/s]$
S	Characteristic curve of the fluid particle
C_s	Smagorinsky constant
l	Filter width [m]
$\overline{S}$	Large-scale strain rate
$U(z)$	Wind velocity at the height of z $[m/s]$
z_{ref}	Height of the wind-measurement point at the station [m]
U_{ref}	Velocity at a reference height $[m/s]$
α	Power-law coefficient
τ_w	Shear stress $[N/m^2]$
δ	Momentum thickness [m]
H_{UBL}	Depth of the UBL [m]
H	Height of the porous medium [m]
L	Length of the porous medium [m]
W	Width of the porous medium [m]
u_e	Free-stream velocity $[m/s]$
∇p	Pressure gradient $[Pa/m]$
a	Darcy coefficient
μ	Viscosity of the fluid $[Pa \cdot s]$
K	Permeability of the porous media $[m^2]$
β	Forchheimer coefficient
A_h	Flow sectional area $[m^2]$
Q	Volumetric flow rate $[m^3/s]$
V	Volume of the porous medium $[m^3]$
θ_i	Angle between the fracture and the inflow wind direction [°]
$\overline{B}$	Average width of fractures [m]
n	Number of fractures

u_0	Average velocity of the inflow wind profile within the urban canopy $[m/s]$
ε	Porosity of the porous medium
ΔP	Pressure drop across the selected urban layout [Pa]
τ	Average tortuosity of the fractures
d_p	Equivalent spherical diameter of buildings in the porous medium [m]
$V_{buildings}$	Average volume of the buildings in the porous medium $[m^3]$
$S_{buildings}$	Average surface area of the buildings in the porous medium $[m^2]$
c	An empirical parameter determined through experiments

CHAPTER 1. Introduction

1.1. Background and significance

According to the Intergovernmental Panel on Climate Change (IPCC), more than half of the world's population presently lives in urban regions, and this number will rise to 70% by 2050 [1]. Rapid urbanization has created many challenges, such as assessing air quality [2], improving thermal comfort [3], and adapting to climate change [4]. These issues are increasingly affecting the health and well-being of urban populations [1]. Urban wind plays an important role in addressing these challenges. It helps disperse pollutants [5], regulate temperatures [6], and improve natural ventilation [7]. Therefore, understanding wind distributions in real urban environments is important for developing sustainable and liveable cities.

To study urban wind distributions, it is critical to understand wind patterns at the pedestrian level. The pedestrian level refers to the height from 1.5 m to 2 m above the ground level [8], and this is the level where urban residents directly experience the effects of wind in their daily lives. At pedestrian level, wind plays a significant role in dispersing pollutants, influencing air quality and public health, particularly in densely populated urban areas [4,9]. It also affects natural ventilation, which can provide cooling in hot climates and reduce energy consumption in urban buildings [6]. Additionally, wind conditions significantly influence pedestrian comfort, determining whether walking through a city is a pleasant experience or a struggle due to strong gusts [3,10]. Thus, it is essential to accurately predict wind distributions at the pedestrian level.

Research into pedestrian-level wind environments has generally relied on wind tunnel experiments or simulations based on simplified building configurations and idealized inflow wind profiles. Common investigations often use generic urban layouts, such as single buildings, isolated street canyons, or arrays of aligned or staggered buildings [2,11–13]. In contrast, the layout of buildings in real cities is highly variable, with complex arrangements and varying heights. Generic urban layouts cannot fully represent the characteristics of real urban layouts, as airflow in cities is significantly influenced by the irregular placement of buildings [14,15]. Furthermore, inflow wind profiles for simulations or wind tunnel tests are typically set

empirically, relying on topography and wind speeds measured at meteorological stations [7,16]. However, the atmospheric conditions have significant impact on the urban wind profiles [17], and these dynamic factors are limitedly considered by previous studies. To sum up, it is necessary to incorporate real urban layouts and realistic wind profiles to precisely capture wind patterns in real urban environments.

A potential solution to this issue is the utilization of a multi-scale modelling approach that combines mesoscale and microscale models. Mesoscale models, such as the Weather Research and Forecasting (WRF) model, can calculate meteorological phenomena with spatial resolutions ranging from several hundred meters to several hundred kilometers [18], effectively capturing the influence of weather, terrain, and regional airflows [19]. In terms of microscale simulations, computational fluid dynamics (CFD) has been widely utilized [20–23], as it can fully model the topography and building geometries within the target areas, and provide detailed wind patterns across the entire domain. By linking these two scales, complex building configurations can be explicitly modelled, and atmospheric conditions can be detailed considered. Therefore, it is crucial to comprehensively investigate the performance and applicability of the multiscale modelling approach in calculating urban wind distributions at pedestrian level in real urban environments.

The objective of this thesis is to develop and validate a multiscale modelling approach for accurately estimating pedestrian-level wind distributions in real urban environments. A key innovation of this study lies in the systematic evaluation of different turbulence models across both generic and real urban layouts, resulting in the identification of a model most suitable for simulating airflow in complex built-up areas. Additionally, field measurements were conducted in a public housing estate to obtain high-resolution wind data at the pedestrian level, which were used to validate the proposed multiscale modelling approach under real-world conditions. This research offers a validated solution for pedestrian-level wind simulations by integrating mesoscale and microscale modelling methods. The proposed multiscale modelling approach contributes to accurate predictions of wind flow in urban environment, thereby providing strategies for enhancing thermal comfort, reducing pollutant exposure, and promoting healthier and more sustainable urban environments.

1.2. Outline of this thesis

This thesis research focuses on multiscale modelling approaches for estimating wind distributions at pedestrian level in real urban environments. The outline of this thesis is shown as follows.

Chapter 2 reviews prior research on experimental measurement methods and numerical simulations of wind distributions at the pedestrian level. It provides a comprehensive overview of turbulence modelling approaches, and the inflow wind profiles in CFD simulations. Additionally, the chapter explores studies on the multiscale modelling approach, which combines mesoscale modelling with CFD to calculate the urban wind distributions.

Chapter 3 evaluates performance of the different categories of turbulence models used in the CFD method for calculating airflow and pollutant dispersion in street canyons with generic and real urban layouts. For each layout, wind tunnel data on airflows and pollutant concentrations served as the benchmarks. This chapter helps determine suitable turbulence models that balance accuracy and computational efficiency for urban wind simulations.

Chapter 4 evaluates the performance and applicability of a combined WRF and CityFFD method for calculating urban wind distributions. A 3.5 km × 2.4 km area in the Kowloon district was selected, with wind speed data from two weather stations used as benchmarks. In addition to demonstrating the potential of the multiscale modelling approach, this chapter identifies limitations of using WRF-calculated wind profiles in densely built-up areas, motivating further refinement of inflow boundary conditions in subsequent chapters.

Chapter 5 proposes an analytical method that improves wind profile estimation in built-up areas by combining WRF with a porosity model. The method was first evaluated in a generic urban layout and then applied to a real area near the King's Park station with available radiosonde data for validation. This chapter addresses the limitations identified in Chapter 4 and improves the applicability of the multiscale modelling approach for calculating wind distributions in dense urban areas.

Chapter 6 investigates the potential of a multiscale modelling approach for calculating pedestrian-level wind distributions by combining CFD simulations with inflow wind profiles estimated using the analytical method proposed in Chapter 5. A public housing estate was selected for field measurements, providing benchmark data to evaluate the accuracy of the multiscale modelling approach. This chapter demonstrates the practical applicability of the proposed approach in real urban environments.

Chapter 7 summarizes the conclusions and proposes future work.

CHAPTER 2. Literature Review

2.1. Experimental measurement

The most direct way to obtain pedestrian-level wind distributions in the real urban environment is to conduct the experimental measurements. Down-scaled wind tunnel experiments, conducted on a fully controlled experimental platform, are widely used to investigate wind conditions in urban areas [7,22,24–26]. For example, Yoshie et al. [24] selected a high-rise building located in a city as the target area and conducted wind tunnel experiments. The scale factor of the building geometries was 1/400, and the sampling points were placed 5 mm above the ground (2 m at full scale) to measure the pedestrian-level wind speed. Shen et al. [25] investigated the wind speed at the pedestrian level in a central urban area in Changsha, China, using wind tunnel experiments, as shown in Fig. 2.1. The scale factor of the building model was 1/250, and the sampling points were located 6.4 mm (1.6 m at full scale) above ground. However, down-scaled wind tunnel experiments may suffer from incompatible similarity requirements [27]. For instance, Tachibana et al., [27] conducted wind tunnel experiments with down-scaled models at scale factors ranging from 1/300 to 1/2000 of the Tokyo Polytechnic University (TPU) campus. They found that the distribution of concentrations was different at the scale of 1/2000 than at the other scale factors. Therefore, field measurements need to be taken in real environments to get realistic data.

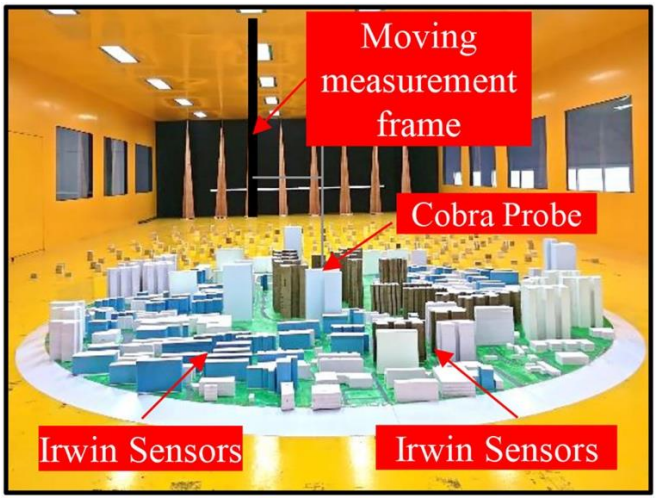

Fig. 2.1 An example of the configuration of down-scaled wind tunnel test used by Shen et al. [25]

Field tests allow direct access to the most realistic wind distributions in the real urban environment, capturing the complex interactions between atmospheric conditions and urban geometries. Meteorological stations are commonly available in many cities [16,28–30]. For example, the Hong Kong Government has established a network of meteorological stations to monitor urban wind speeds, with station heights ranging from 3 m to 593 m above sea level (see Fig. 2.2) [28]. Additionally, several studies have utilized onsite measurements to investigate urban wind patterns [27,31–34]. For instance, Eliasson et al., [32] conducted a one-year measurement campaign in a street canyon in Göteborg, Sweden. They placed 11 sensors at heights ranging from 3.1 m to 14 m to obtain the mean flow patterns within the selected canyon. Zou et al., [33] performed onsite wind measurement over a period of four months in Sydney, Australia. Their sampling points were placed at 0.6 m, 1.2 m, and 1.8 m respectively to capture the wind distributions within pedestrian height in urban areas. Despite these efforts, field measurements at pedestrian level remain limited. Further efforts are necessary to expand onsite measurements specifically at pedestrian heights to address this limitation. Moreover, both wind tunnel experiments and field tests provide data only at limited sampling points, which cannot fully capture the spatial variability of urban wind distributions. Therefore, numerical simulations are required to achieve a detailed understanding of airflow in real urban environments.

Fig. 2.2 Network of meteorological stations in Hong Kong

2.2. Numerical simulations of wind distributions at pedestrian level

Numerical modelling has become a popular approach for investigating urban wind distributions, as they can provide detailed data across the entire computational domain. Computational Fluid Dynamics (CFD) is widely utilized due to its capability to explicitly model the topography and built-up areas within the target region [35–38]. For instance, van Hoof et al. [35] established a complex geometry for a football stadium with a 500-m radius with detailed windows and steel roof constructions. Toparlar et al. [36] explicitly modelled the buildings located in a circular area with a diameter of 1200 m to investigate the urban microclimate of the Bergpolder Zuid region in the Netherlands. The accuracy of CFD simulations for calculating pedestrian-level wind distributions has been well proven in previous studies [22,25,39,40]. For example, Blocken et al. [39] conducted CFD simulations to calculate the pedestrian-level wind distributions (at the height of 1.75 m) for the campus of Eindhoven University of Technology in the Netherland. Their simulated results showed good agreement with field measurement data, with a deviation of 14%. Shui et al. [40] selected seven representative configurations of actual urban residential areas in China as the study areas, and used CFD to calculate pedestrian-level wind patterns (at the height of 1.5 m). They found that, for most sampling locations, the differences between simulated and measured wind speed ratios were less than 20%. Therefore, CFD simulations were conducted in this study to predict pedestrian-level wind distributions in real urban environments.

2.2.1. Turbulence modelling approaches in CFD

Turbulence modelling approach is crucial for CFD simulations, as turbulence models have varying effects on the accuracy of the predicted wind patterns [36,41–45]. Reynolds-averaged Navier-Stokes simulations (RANS) and large-eddy simulation (LES) are two prevalent turbulence modelling approaches for calculating airflow in urban areas [2,12,46,47]. LES can resolve large eddies and model small eddies, capturing the transient motions for unsteady fluctuations (referred to as small-scale fluctuations shown in Fig. 2.3) with high computational cost [42–44]. For example, Gousseau et al. [43] compared the wind patterns provided by LES and steady-state RANS (SRANS) with the standard $k-\varepsilon$ model for several buildings in

downtown Montreal. They found that, in comparison to SRANS, LES showed better agreement with wind tunnel data, but the computation time was seven times longer. Therefore, LES is a more accurate approach than RANS for calculating airflow in urban street canyons, but it requires more computational resources. RANS solves ensemble-averaged flow, and all scales of turbulence are modelled. This results in limited accuracy for reproducing wind distributions in the outdoor environment [12,43,47]. For instance, Zheng and Yang [12] assessed steady-state RANS (SRANS) simulations using five turbulence models for wind distributions in a street canyon between two buildings, finding that all models underestimated the spanwise velocity in comparison with to wind tunnel experiments. Among the various turbulence models used in SRANS studies, the RNG $k-\varepsilon$ model, standard $k-\varepsilon$ model, realizable $k-\varepsilon$ model, and shear stress transport (SST) $k-\omega$ model are widely used for calculating wind distributions in urban areas [13,45,48,49]. Tominaga and Stathopoulos [45] investigated the accuracy of SRANS with different types of $k-\varepsilon$ models in predicting the airflow around a single building. They found that SRANS with the RNG $k-\varepsilon$ model showed better agreement with the wind tunnel data than other selected models. Yu and Thé [48] calculated the wind distributions and pollutant dispersion concentration around an isolated building using SRANS with the standard $k-\varepsilon$ model and SST $k-\omega$ model. They compared the simulated data with wind tunnel data, and found that the SST $k-\omega$ model performed better than the standard $k-\varepsilon$ model for SRANS simulations. Therefore, the RNG $k-\varepsilon$ model and SST $k-\omega$ model with the SRANS scheme were the most promising turbulence models for outdoor wind simulations. Moreover, previous studies revealed that even when the same turbulence model was used, different results were provided by steady-state and unsteady-state RANS simulations [13,49]. For example, Tominaga [49] found that, unlike SRANS simulations, unsteady-state RANS (URANS) with the SST $k-\omega$ model could calculate periodic fluctuations (referred to as large-scale fluctuations as shown in Fig. 2.3) of airflow around an isolated building. To sum up, SRANS/URANS with the RNG $k-\varepsilon$ model and SST $k-\omega$ model, along with the LES approach, are popular turbulence modelling approaches for calculating airflows in urban street canyons. LES can capture small-scale turbulence, though it is computationally demanding. In contrast, URANS is computationally efficient but lack the precision needed for complex turbulence modelling. Considering these differences, it is crucial to investigate whether URANS can be a justifiable alternative to LES approach for calculating airflows in urban street canyons. Therefore, further investigations are needed to compare and assess the performance of these selected turbulence modelling approaches in urban street canyons.

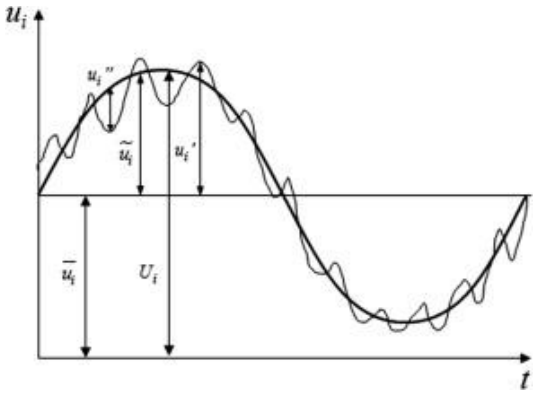

Fig. 2.3 Large-scale and small-scale velocity fluctuations in the turbulent vortex-shedding flow [49]

Although extensive studies have been conducted to assess different turbulence models for predicting airflows in urban areas, the majority of these studies have focused on generic urban layouts [2,11,12,38,46,50–52]. The building configurations in most studies are idealized and highly simplified, such as a single building, an isolated street canyon, or an array of aligned or staggered buildings. For example, Liu and Niu [11] evaluated the performance of SRANS with the RNG $k-\varepsilon$ model and LES in calculating airflow around an isolated building model with dimensions of 0.8 m in length and width and 1.6 m in height. Tominaga and Stathopoulos [51] selected as the target configuration an ideal street canyon consisting of two buildings, each with an aspect ratio of 2, where the width of the street was equal to the width of the building. URANS with the RNG $k-\varepsilon$ model and LES were used to calculate the wind patterns in this street canyon. Tominaga and Stathopoulos [38] further assessed the performance of SRANS with the RNG $k-\varepsilon$ model and LES in predicting the airflow and pollutant dispersion in an ideal 6×5 array of cubic buildings. However, it has been reported that generic urban layouts cannot adequately represent real urban layouts, as wind patterns are significantly affected by the uneven placement of buildings [14,15,53]. For example, Nosek et al. [14] used LES to calculate pollutant dispersion patterns in two sets of building arrays. The buildings in one set were all of equal height, while the heights in the other set were randomly assigned. The researchers found that variability in building height enhanced velocity fluctuations in the lateral direction. To date, only a limited number of comparative studies have focused on real urban layouts. Therefore, further efforts should be made to investigate the performance and applicability of different turbulence modelling approaches for calculating airflow in real urban layouts.

2.2.2. Inflow wind profiles of CFD

For CFD modelling, setting inflow boundary conditions is critical for obtaining an appropriate flow field [9,47]. The wind profile within the urban ABL features a power-law [54–56] or a log-law expression [57,58]. Experimental studies have found that the log law is suitable to describe the wind speed profile below 200 meters [54,55], while the power law provides a better fit for wind profiles above 200 meters [56]. The power-law profile has an exponent ranging from 0.1 to 0.5 [59]. The power-law coefficient is normally determined empirically from the urban surfaces and topography as a constant for CFD inflow boundaries [60]. The wind speed at a reference height, such as the speed measured at a meteorological station, is also needed [16,61]. Therefore, this method for setting the inflow boundary conditions is a semi-empirical method. However, it has been reported that the power-law exponents of the ABL can vary strongly with spatial and temporal factors [62–66]. He et al. [64] investigated the wind profiles in Hong Kong under typical summer conditions with Doppler LiDAR. They observed that wind profiles were significantly modified by urban layouts, and the power of the wind profile was much higher in built-up areas. Halios and Barlow [65] reported the morning transition of the ABL in London, attempting to explain the diurnal variation of the ABL's power-law value. Lim et al. [66] found that the power-law index for wind profiles was time-dependent in Tokyo due to the diurnal cycle, with higher values (0.2-0.3) at night and lower values (0.1) during the daytime. Therefore, the semi-empirical methods for generating the inflow boundary conditions for CFD models, especially the wind profiles, are idealized and oversimplified.

2.3. The multi-scale modelling approach

2.3.1. Inflow wind profiles from mesoscale modelling

To provide more realistic inflow boundary conditions for CFD simulations, mesoscale modelling is a potential solution, such as the Weather Research and Forecasting model (WRF) [67,68]. Simulations with the WRF model are mainly conducted with spatial resolution from

several hundred meters to several hundred kilometers. These grand spatial scale models can rationally reproduce meteorological phenomena, including diurnal variation, sea breezes, and heat waves [68]. Given the situation above, multiscale modelling has been proven to be a potential method for providing CFD models with more accurate inflow boundary conditions [69–72]. Tewari et al. [71] used WRF output data, including wind velocity components, turbulence kinetic energy (TKE), and potential temperature, as the initial and boundary conditions. They found that the accuracy of the CFD-Urban model has improved when using WRF output for pollutant propagation simulations, compared with using measured data as initial and boundary conditions. Mortezazadeh et al. [72] integrated CFD models and WRF to investigate the urban temperature distribution during heat waves. They used WRF results such as the wind velocity at the height of 10 m, air temperature, and street surface temperature as input for the CFD simulation and found that it is important to use microclimate simulations to study urban heatwaves. However, there has been only limited research on the use of wind profiles obtained by mesoscale modelling for CFD models. Therefore, it is meaningful to evaluate the performance and applicability of the time-varying wind profiles obtained from mesoscale models.

2.3.2. Enhancing wind profiles provided by mesoscale models

When conducting WRF simulations to provide inflow wind profiles for CFD models, land surfaces are parameterized as drag forces [73]. Studies have shown that WRF can provide accurate wind profiles in areas with simple land cover, such as coastal regions, mountainous areas, and suburbs. However, for built-up areas with complex and highly heterogeneous land cover, the wind profiles calculated by WRF tended to significantly overestimate wind speeds near the ground [17,64,74]. For example, He et al. [64] compared wind profiles from WRF with measured data for an undeveloped peninsula and the downtown area in Hong Kong. They found that WRF performed well in the undeveloped region, but overestimated wind speeds by more than 25% compared to the measured data in the downtown area. Wang et al. [74] compared the performance of WRF in calculating wind distributions in coastal and built-up areas, and wind speed measured by meteorological stations was used as benchmark. The finding showed that WRF results closely matched the benchmarks in the coastal area, but in the built-up area, WRF overestimated wind speeds by more than 30% most of the time.

However, when using multiscale modelling approach to calculate pedestrian-level wind distributions, the target area is not always located near the urban edge. Therefore, it is necessary to improve the performance of WRF in calculating wind profiles within built-up areas.

To accurately estimate wind profiles in built-up areas, previous studies have used wind profiles from the urban edge as inflow conditions for CFD simulations, with the entire region between the urban edge and the target area included in the CFD computational domain [17,23,74–76]. For example, Peng et al. [76] conducted CFD simulations to investigate the urban wind distributions in Kowloon, Hong Kong, over an area of 6 km × 6 km. They explicitly resolved all the buildings in the selected urban area and used wind profiles from coastal areas as inflow boundary conditions, as shown in Fig. 2.4. However, CFD simulations are time consuming in practical applications, as it involves complex geometric modelling, mesh generation, and iterative computations to achieve convergence. For instance, Ricci and Blocken [30] conducted CFD simulations to investigate the wind conditions of the IJmuiden Sea lock in Amsterdam, Netherlands. They established the computational grid based on the building geometries within the domain, resulting in a total grid number of 74 million. The simulation required up to 144 hours of computation time. Therefore, it is necessary to develop a method that is both easy to apply and fast in calculating wind profiles in built-up areas.

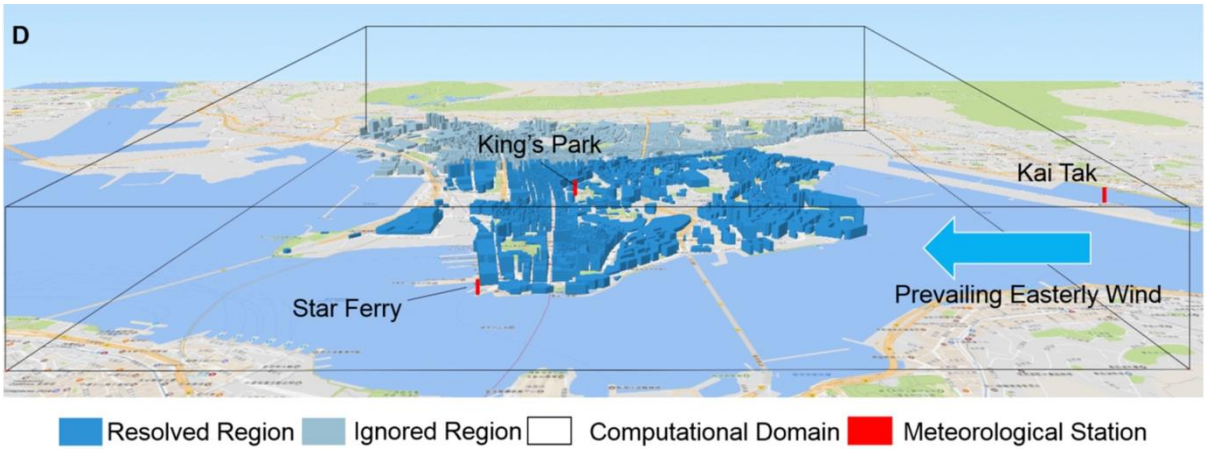

Fig. 2.4 CFD simulations conducted by Peng et al. [76], with all the buildings in the computational domain explicitly modelled.

Analytical modelling is a straightforward and computationally efficient approach, as it can provide explicit mathematical expressions for urban wind profiles without relying on numerical simulations [77–79]. For example, Ikegaya [79] applied the momentum integral method to

derive explicit formulas for wind profiles within the UBL for a cubical building array. Similarly, this analytical model was also applied by Yang et al. [78] to establish explicit wind profile expressions for four different building arrays characterized by varying heights and arrangements. Although these studies demonstrate the effectiveness of analytical modelling approach, they are primarily focused on generic urban layouts, such as building arrays with simple configurations. Therefore, it is essential to develop the analytical modelling approaches that can efficiently improve the performance of WRF for predicting urban wind profiles in real urban layouts.

2.4. Research gaps

Through this literature review, several key research gaps have been identified in the accurate estimation of pedestrian-level wind environments in real urban layouts. Therefore, CFD simulations were employed in this study. A key factor influencing the accuracy of CFD simulations is the choice of turbulence model, as different turbulence models have varying impacts on the accuracy of predicted wind patterns. Previous research has compared the performance of different turbulence models in generic urban layouts with simplified building configurations. However, these configurations fail to reflect the geometric complexity of real cities. In real urban environments, uneven building arrangements can significantly alter wind flow patterns. Therefore, further investigation is needed to assess the applicability of different turbulence models for simulating airflow in real urban layouts.

Apart from the turbulence modelling approach, the setting of inflow wind profiles is also crucial in CFD simulations for outdoor wind distributions. Previous studies have used semi-empirical methods such as log-law or power-law profiles to define inflow boundary conditions. These idealized profiles were oversimplified, as they neglected temporal and spatial variability in real urban environments. To address this, mesoscale models such as the Weather Research and Forecasting (WRF) model have been employed to provide more realistic inflow boundary conditions. However, due to simplified land cover parameterization, WRF tends to overestimate near-ground wind speeds in built-up areas, limiting its direct applicability for

urban-scale CFD. Therefore, it is crucial to develop advanced approaches that can efficiently improve the accuracy of WRF-calculated inflow profiles in dense urban settings.

Finally, to evaluate the performance of the proposed multiscale modelling approach for urban wind simulations, experimental data were needed. Although numerous wind tunnel studies have been conducted to validate CFD models for outdoor wind environments, these experiments are based on scaled-down physical models. Such models may suffer from incompatible similarity requirements. To overcome these limitations, field measurements in real urban environments are essential for evaluating the performance of multiscale modeling approaches and ensuring their applicability to real-world wind simulations. These gaps form the core motivation of this thesis, which aimed to develop and validate a multiscale modelling approach that combined mesoscale and microscale methods for accurately estimating pedestrian-level wind distributions in real urban environments.

2.5. Tasks in this thesis

Based on the review conducted in this chapter, this study proposes the following tasks to propose multiscale modelling approaches for estimating wind distributions at pedestrian level in real urban environments:

(1) Evaluate different categories of turbulence models for calculating airflow and air pollutant dispersion in street canyons with generic and real urban layouts.

(2) Propose a combined WRF and CFD method for calculating urban wind distributions.

(3) Develop an analytical method to predict urban wind profile in built-up areas using a combined method of WRF and a porosity model.

(4) Application of the proposed multiscale modelling approach for calculating pedestrian-level wind distributions in real urban environments, with field measurements as the benchmark.

CHAPTER 3. Evaluate different categories of turbulence models for calculating airflow and air pollutant dispersion in street canyons with generic and real urban layouts

To calculate pedestrian-level wind distributions in real urban environments using the multiscale modelling approach, it is crucial to investigate the applicability of various turbulence models used in CFD for outdoor wind simulations. Therefore, this chapter assessed SRANS/URANS with the RNG $k-\varepsilon$ model and SST $k-\omega$ model, along with the LES approach, for calculating airflow in both generic and real urban street canyons. Additionally, to evaluate the accuracy of turbulence structures predicted by the selected models, the calculated pollutant concentration was assessed, as pollutant dispersion is directly influenced by the flow patterns in urban environments [44]. In this chapter, two urban layouts were selected for analysis, including a building array and a real urban layout. For each urban layout, wind tunnel experiments with measured data on wind speed and pollutant concentration were chosen as the benchmark. To further demonstrate the differences between URANS and LES, instantaneous concentration fields were also analyzed. Finally, this chapter assessed the performance and applicability of selected turbulence modelling approaches in generic and real urban layouts.

3.1. Methodology

This study aimed to evaluate the performance of different CFD turbulence models in predicting airflow and pollutant dispersion in generic and real urban layouts. For the RANS scheme, according to the literature review above, the RNG $k-\varepsilon$ model and SST $k-\omega$ model are the most promising RANS approach for calculating airflows and pollutant dispersion in street canyons [45,48]. Additionally, the SST $k-\omega$ model has been specifically noted for its ability to reproduce large-scale fluctuations in URANS simulations [13,49]. LES was also chosen as it can capture small-scale fluctuations and provide more accurate results compared to RANS. Thus, SRANS/URANS with the $k-\varepsilon$ model and SST $k-\omega$ model, along with LES, were selected to be evaluated in this study. This section details the numerical approaches for the turbulence models used in the study.

3.1.1. RNG $k-\varepsilon$ model

For the governing equations of SRANS approach, the following continuity and momentum conservation equations were solved for an incompressible Newtonian fluid:

$$\frac{\partial \overline{u_i}}{\partial x_i} = 0 \tag{3.1}$$

$$\overline{u_j}\frac{\partial \overline{u_i}}{\partial x_j} = -\frac{1}{\rho}\frac{\partial \bar{p}}{\partial x_i} + \upsilon\frac{\partial^2 \overline{u_i}}{\partial x_j^2} - \overline{u_j'\frac{\partial u_i'}{\partial x_j}} \tag{3.2}$$

where $\mathrm{i,j} = 1, 2 \text{ and } 3$; x_i and x_j are spatial coordinates; $\overline{u_i}$ and u_i' are the mean and fluctuating velocity of the i^{th} component $(\mathrm{m/s})$; $\bar{p}$ is the mean pressure (Pa); ρ is the density (kg/m^3); and υ is the viscosity $(\mathrm{N \cdot s}/m^2)$.

For URANS, the continuity equation is consistent with that in SRANS (see Eq. (3.1)), while an additional time derivative is introduced into the momentum equation. The momentum equation for URANS is expressed by Eq. (3.3).

$$\frac{\partial \overline{u_i}}{\partial t} + \overline{u_j}\frac{\partial \overline{u_i}}{\partial x_j} = -\frac{1}{\rho}\frac{\partial \bar{p}}{\partial x_i} + \upsilon\frac{\partial^2 \overline{u_i}}{\partial x_j^2} - \overline{u_j'\frac{\partial u_i'}{\partial x_j}} \tag{3.3}$$

where t is time (s). Note that although URANS approach solves for transient simulations, it still performs ensemble averaging [49].

The RNG $\mathrm{k}-\varepsilon$ turbulence model is a two-equation model, solving two partial differential transport equations for turbulence kinetic energy (k) and dissipation rate (ε) to obtain the turbulent viscosity. The equations can be written as [80]:

$$\frac{\partial k}{\partial t} + \overline{u_j}\frac{\partial k}{\partial x_j} = \frac{1}{\rho}\frac{\partial}{\partial x_j}\left[\frac{\upsilon_t}{\sigma_k}\frac{\partial k}{\partial x_j}\right] + P_k - \varepsilon \tag{3.4}$$

$$\frac{\partial \varepsilon}{\partial t} + \overline{u_j}\frac{\partial \varepsilon}{\partial x_j} = \frac{1}{\rho}\frac{\partial}{\partial x_j}\left[\frac{\upsilon_t}{\sigma_\varepsilon}\frac{\partial \varepsilon}{\partial x_j}\right] + \frac{\varepsilon}{k}(C_{\varepsilon 1}P_k - C_{\varepsilon 2}\varepsilon) \tag{3.5}$$

where υ_t is the turbulent kinematic viscosity ($\mathrm{N}\cdot\mathrm{s}/m^2$), and P_k is the production term of k ($\mathrm{N}/s\cdot m^2$). The values of the model constants were $C_{\varepsilon 1}=1.42, C_{\varepsilon 2}=1.68, \sigma_k=1, \sigma_\varepsilon=0.719$, and $C_\mu=0.085$ [80].

3.1.2. SST $k-\omega$ model

The governing equations for the SST $\mathrm{k}-\omega$ turbulence model were the same as for the RNG $\mathrm{k}-\varepsilon$ model (see Eqs. (3.1) to (3.3)). Turbulent viscosity is obtained by means of the following two partial differential transport equations for turbulence kinetic energy (k) and dissipation rate (ω) [81]:

$$\frac{\partial k}{\partial t}+\overline{u_j}\frac{\partial k}{\partial x_j}=\frac{1}{\rho}\frac{\partial}{\partial x_j}\left[(\upsilon+\frac{\upsilon_t}{\sigma_k})\frac{\partial k}{\partial x_j}\right]+P_k-\beta^*\omega k \tag{3.6}$$

$$\frac{\partial \omega}{\partial t}+\overline{u_j}\frac{\partial \omega}{\partial x_j}=\frac{1}{\rho}\frac{\partial}{\partial x_j}\left[(\upsilon+\frac{\upsilon_t}{\sigma_\omega})\frac{\partial \omega}{\partial x_j}\right]+\frac{\gamma}{\upsilon_t}G-\beta\omega^2+2(1-F_1)\frac{\sigma_{\omega 2}}{\omega}\frac{\partial k}{\partial x_j}\frac{\partial \omega}{\partial x_j} \tag{3.7}$$

where σ_k, σ_ω, β and γ are model constants determined by functions F_1 and F_2 , and further details of the model can be found in Refs. [81], [82].

3.1.3. Large-Eddy Simulation (LES)

For the LES approach, the large-scale eddies are resolved directly by Navier-Stokes equations, and the small-scale eddies are modelled by a subgrid-scale (SGS) model. The Smagorinsky model has been proved to accurately calculate flow fields around buildings as the SGS model [38,74,83]. Hence, the Smagorinsky model was employed as the SGS model in this study. The continuity equation for LES is the same as Eq. (3.1), and the momentum equations are shown below:

$$\frac{\partial \overline{u_\iota}}{\partial t}+\overline{u_j}\frac{\partial \overline{u_\iota}}{\partial x_j}=-\frac{1}{\rho}\frac{\partial \bar{p}}{\partial x_i}+\upsilon\frac{\partial^2 \overline{u_\iota}}{\partial x_j^2}-\frac{\partial \tau_{ij}^s}{\partial x_j} \tag{3.8}$$

where τ_{ij}^{s} is the sub-grid stress (N/m^2), and the equations can be written as [84]:

$$\tau_{ij}^{s} = \upsilon_t \left(\frac{\partial \overline{u_i}}{\partial x_j} + \frac{\partial \overline{u_j}}{\partial x_i} \right) + \frac{1}{3} \rho \tau_{kk}^{s} \delta_{ij} \tag{3.9}$$

The turbulence viscosity is modelled by [84]:

$$\upsilon_t = \left(C_s \Delta_{sgs} \right)^2 |\bar{S}| \tag{3.10}$$

$$\Delta_{sgs} = (\Delta x \Delta y \Delta z)^{1/3} \tag{3.11}$$

$$\overline{S} = \frac{1}{2} \left(\frac{\partial u_i}{\partial x_j} + \frac{\partial u_j}{\partial x_i} \right) \tag{3.12}$$

where υ_t is the turbulent kinematic viscosity ($\mathrm{N} \cdot \mathrm{s}/m^2$); $\overline{S}$ is the large-scale strain rate; Δ_{sgs} is the grid size that defines the sub-grid length scale; and $\Delta x, \Delta y, \Delta z$ are the discrete lengths in the x, y, and z directions, respectively.

3.1.4. Dispersion modelling

The Eulerian approach was employed to calculate pollutant dispersion in this study. The concentration of a tracer gas was considered as a passive scalar, and the advection-diffusion equation was adopted to simulate the mass diffusion [85]:

$$\frac{\partial C}{\partial t} + \nabla (C \boldsymbol{u}) = \nabla \cdot [(D_c + \upsilon_t / Sc_t) \nabla C] + S_c \tag{3.13}$$

where C is the pollutant concentration; u is the velocity vector (m/s); D_c is the molecular diffusion coefficient (m^2/s); and Sc_t is the turbulent Schmidt number, which was set to 0.7 in this study [46,48,86]. For SRANS, once the flow field reached a steady state and converged, the scalar transport equation was activated. For URANS and LES, the scalar equation was computed synergistically with Eqs. (3.1) and (3.3) / (3.8) at each time step. The method of obtaining time-averaged solutions for transient models is presented in Section 3.1.5.

3.1.5. Solver settings

This investigation was implemented in OpenFOAM 2.3.0 with an open-source CFD code, RapidCFD [87], on an NVIDIA GeForce RTX 3090Ti GPU. The second-order scheme was applied for discretizing pressure, and the second-order upwind scheme was employed for all the other variables [88]. The PISO algorithm was used for pressure-velocity coupling [89]. The scalable wall function aims to address the limitations of standard wall function when dealing with fine grid resolutions near walls. It adjusts the wall shear stress calculation when the mesh is close to the wall, ensuring accuracy in simulations [90,91]. As the y+ value was around 4, the scalable wall function was used. For transient simulations (URANS and LES), the time integration scheme was set as the implicit second-order upwind Euler scheme [90]. To make the transient simulations stable and robust, Courant–Friedrichs–Lewy (CFL) numbers should be carefully defined [43,45,51,92,93]. In explicit time integration schemes, the solution at the next time step is calculated directly from known variables at the current time step. These methods are computationally efficient per time step but require small time steps to maintain stability. Thus, the CFL number should be kept below 1. In contrast, implicit time integration schemes are unconditionally stable by solving a system of equations that involves both the current and future states of the system. Therefore, implicit schemes are robust and allow for a higher CFL number [94,95]. In our study, we employed the implicit time integration scheme, allowing us to use a CFL number slightly larger than 1. This approach was chosen to improve computational efficiency while ensuring the stability and accuracy of the simulation.

To obtain time-averaged results calculated by transient models, the sampling time scale $10t^*$ was used, where t^* is the time required for the airflow to pass through the domain once. Note that the LES simulations were initialized by the results of the steady-state RNG $k-\varepsilon$ model, and the first $10t^*$ was taken as a spin-up period to eliminate dependence on the initial state. The performance of this approach in calculating the dispersion of pollutants in the outdoor environment has been demonstrated in previous literature [12,43]. The solutions were considered to be converged when the scaled residuals reached a minimum value. For the generic urban layout, the minimum values were 10^{-6} for concentration and 10^{-5} for continuity, momentum and turbulence. For the real urban layout, the minimum values were 10^{-4} for continuity, momentum and concentration, and 10^{-5} for turbulence.

3.2. Case setup

To evaluate the performance and applicability of selected turbulence modelling approaches in different urban street canyons, airflows and pollutant dispersion in a generic urban layout and a real urban layout was calculated for further analysis. The generic urban layout was a 9×9 building array, and the real urban layout was a 1/600 scale model of the TPU campus. Wind tunnel experiments were available for both cases with measured wind speed and pollutant concentration distribution. This section presents the wind tunnel test and simulation setup of each case.

3.2.1. Generic urban layout

The wind tunnel experiment for the building array was conducted in an atmospheric boundary layer (ABL) wind tunnel with a cross section of $1\ \text{m} \times 1.2\ \text{m}$ (height × width) [27]. Measured data from the street canyon in a 9×9 building array were used. The selected building array consisted of buildings with dimensions of $0.06\ \text{m} \times 0.06\ \text{m} \times 0.06\ \text{m}$ (See Fig. 3.1). Ethylene (C_2H_4) was used as a tracer gas, with a release concentration of 1×10^6 ppm and a flow rate of $3.6 \times 10^{-6}\ \text{m}^3/\text{s}$ [96]. To capture detailed airflow and pollutant dispersion patterns in the street canyons, measurement points were located on both the horizontal and vertical planes, as shown in Fig. 3.1(c). Note that the green sampling points in Fig. 3.1(c) each had 5 vertical sampling locations, at heights of 0.004 m, 0.01 m, 0.03 m, 0.05 m, and 0.07 m, respectively (see Fig. 3.1(d)). The pink sampling points included three vertical sampling positions, at heights of 0.004 m, 0.01 m, and 0.03 m, shown in Fig. 3.1(e). Detailed information about the wind tunnel experiments can be found in the literature [27]. A Split-Film Probe (SFP) was used to measure the three components of wind speed (streamwise, lateral, and vertical directions), and a fast response flame ionization detector (FID) was used to measure the concentration of the tracer gas. The sampling frequency for both instruments was 1000 Hz, and data were averaged over a 60-second period to obtain the mean wind velocity and time-averaged concentration.

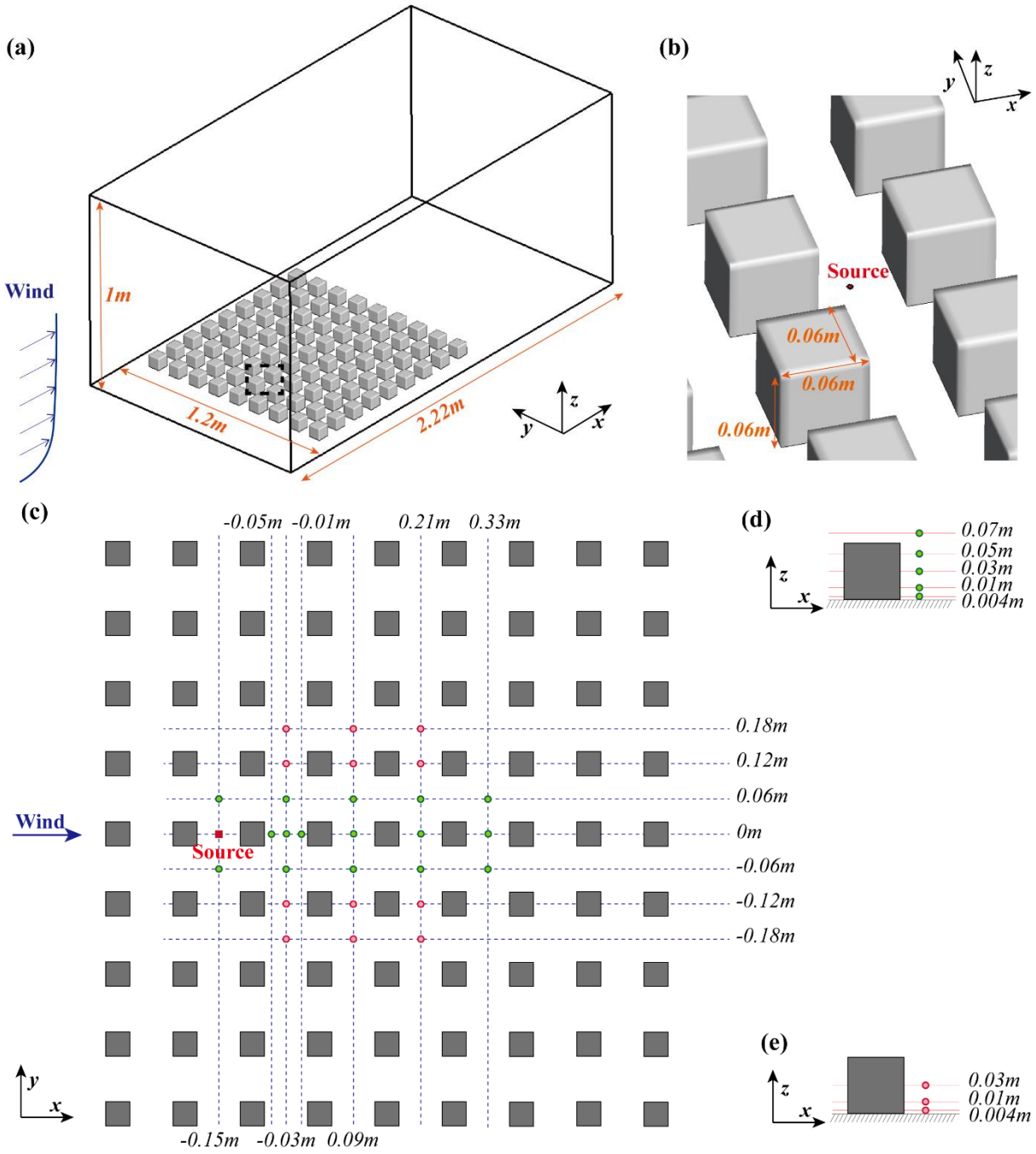

Fig. 3.1 (a) Computational domain of the 9×9 building array, (b) detailed configuration of source and building, (c) measurement points in the building array, (d) vertical locations of green points and (e) pink points (redrawn from Ref. [96]).

For the computational domain of the generic urban layout, the spanwise and vertical sizes were set to be the same as the actual dimensions of the wind tunnel [96]. For the streamwise distance, according to the COST 732 [97] and AIJ guidelines [59], the upstream distance was 0.3 m ($5H_A$, where H_A is the buildings' height), and the downstream length was 0.9 m ($15H_A$). Thus, the computational domain for building arrays was set as 2.22 m (length) × 1.2 m (width) ×

1 m (height), as shown in Fig. 3.1(a). The size of the emission source was approximated in our simulations as a circle with a radius of 2 mm. The time step for unsteady simulations was set as 0.001 s, and the resulting CFL number was around 0.7. Hexahedral cells with a size of 0.00375 m were used near the buildings, and the grid size gradually increased with a stretching ratio of 1.08 in all directions. The maximum grid size was 0.03 m, and the total grid number was 2.46 million, as shown in Fig. 3.2. Although the LES simulations showed a difference between the fine mesh and base mesh, implementing a very fine mesh for the building array could require a very large computing capacity. Therefore, the mesh design for SRANS, URANS and LES was the same. A grid-independence test can be found in Fig. S.1 and Fig. S.2 in the Supplementary Material.

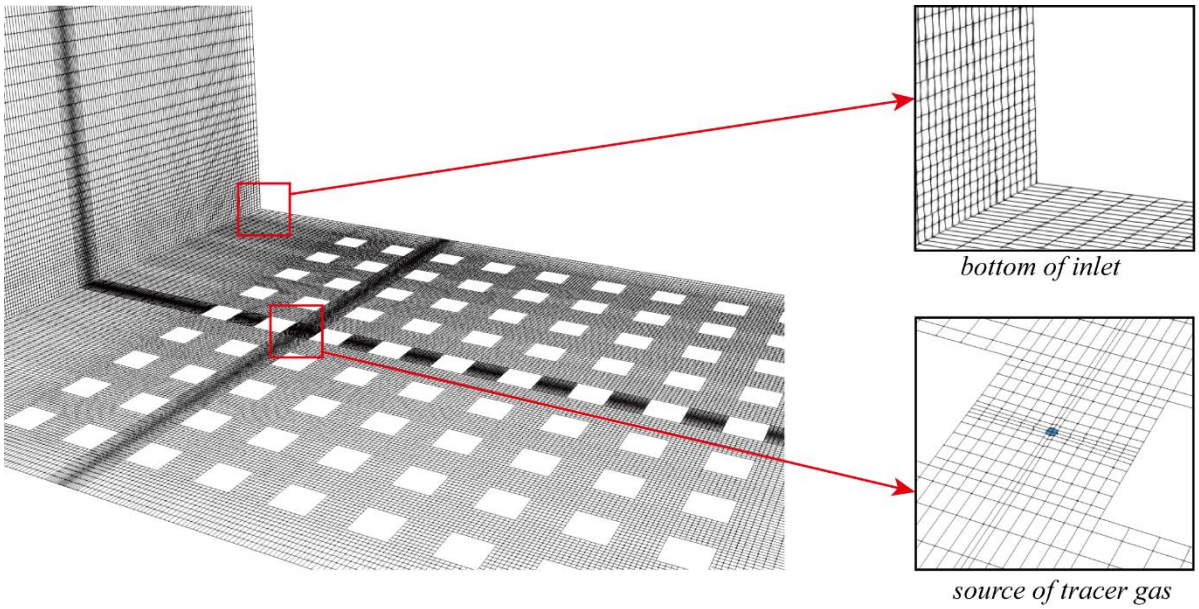

Fig. 3.2 Grid distribution for the generic urban layout case.

The bottom and lateral boundaries of the computational domain and the building surfaces were all set as no-slip walls to replicate the wind tunnel test section. The top surface was set as symmetry [45,49,86]. At the outlet, a zero-gradient condition was prescribed. The emission source was defined as the velocity inlet. In the wind tunnel experiment, the tracer gas was released from a source with a radius of 2 millimeters with the gas flow rate (3.6×10^{-6} m^3/s). Therefore, the tracer gas was set to be released at a velocity of $0.287\ m/s$ in the simulation set up. The velocity inlet boundary conditions can be found in the following subsections.

3.2.1.1. RNG $k-\varepsilon$ model

The inlet boundary conditions of velocity and turbulence kinetic energy (TKE) were obtained by linear interpolation of the experimental data [96]. The turbulence dissipation rate ε was estimated by Eq. (3.14) [98]:

$$\varepsilon(z) = \frac{u^{*3}}{\kappa(z + z_0)} \tag{3.14}$$

where the friction velocity $u^* = 0.465$ m/s, and the roughness length $z_0 = 0.001\ m$ (obtained from logarithmic-law curve fitting of the mean velocity profile in wind tunnel experiments [12]). The von Karman constant κ was set as 0.41 [12,16,46].

3.2.1.2. SST $k-\omega$ model

For the inlet boundary conditions of the SST k − ω model, the turbulence dissipation rate was calculated by Eq. (3.15) [99]. The velocity and TKE at the inlet boundary were kept consistent with those of the RNG $k-\varepsilon$ model, as described in Section 3.2.1.1.

$$\omega(z) = \frac{\varepsilon(z)}{C_\mu k(z)} \tag{3.15}$$

where the $\varepsilon(z)$ was obtained by Eq. (3.15), and C_μ was 0.085 [80].

3.2.1.3. LES

For LES simulation, in addition to the measured mean velocity, a fluctuation scale was used to introduce perturbations at the inflow boundary [100,101]. Based on the root mean square values of measured velocity in three directions [96], the fluctuation scales in the x, y, z directions were set to 0.6, 0.6, and 0.4, respectively.

3.2.2. Real urban layout

An experiment representing a real urban layout was also conducted in the ABL wind tunnel described in Section 3.2.1. A scaled model of the TPU campus was used for the airflows and pollutant dispersion measurements, as shown in Fig. 3.3(a). The terrain and buildings within a 300-meter radius of the TPU campus center (labelled as the origin point in Fig. 3.3(b)) were explicitly built in the scaled model to accurately capture the wind and pollutant concentration distributions in the target area. Ethylene (C_2H_4) at a concentration of 100% was used as the tracer gas, and was released at 0.088 m/s through an outlet with a radius of 3 mm. To capture the pollutant dispersion pattern at pedestrian level within the campus, the measurement points were set at a height of 5 mm from the ground in the scaled model, corresponding to 3 m at full scale. The top view of the measurement points is shown in Fig. 3.3(b). Detailed information about the wind tunnel experiments can be found in the literature [27]. The wind speed was measured using the SFP, while concentration was measured using a High-Speed Total Hydrocarbon Analyzer (HTHC). The sampling frequency was 1000 Hz, with data averaged over 180 seconds to obtain the mean wind velocity and over 240 seconds to obtain the time-averaged concentration.

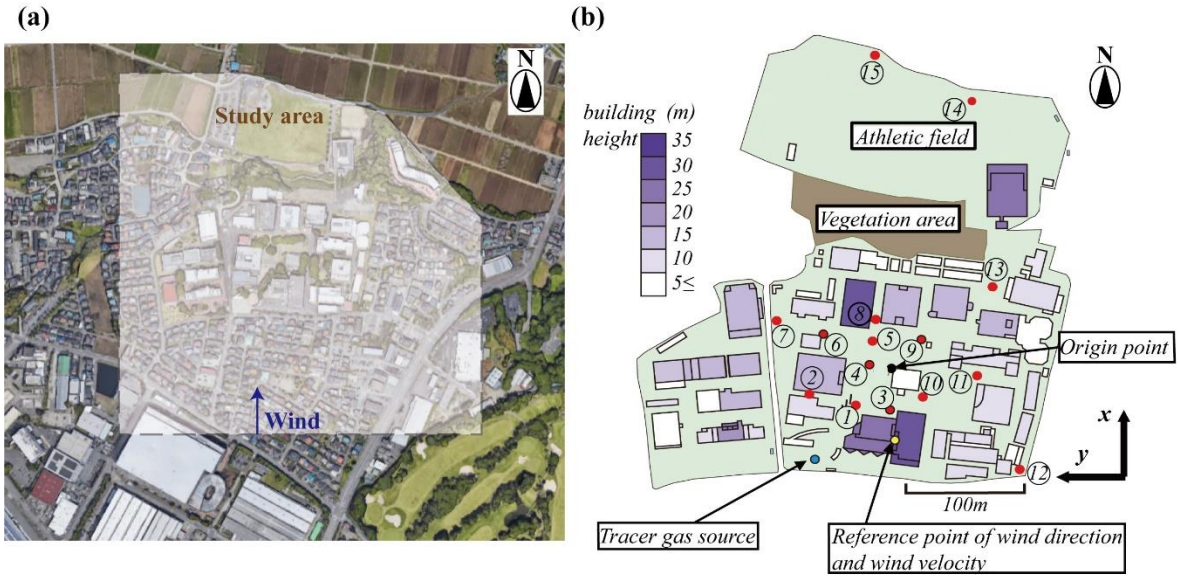

Fig. 3.3 (a) Satellite map of the study area, and (b) measurement locations for the wind tunnel test in the real urban layout case redrawn from [10].

For the real urban layout, the domain size was determined according to the spanwise dimension of the wind tunnel and guidelines [59,97]: the upstream and downstream distances were $5H_B$ and $15H_B$, respectively, and the vertical length was $5H_B$. Here, H_B, representing the rooftop height of the tallest building, was 0.068 m. Therefore, the domain size for the real urban layout was set as 1.8 m (length) × 1.2 m (wide) × 0.34 m (height), as shown in Fig. 3.4(a). Note that the terrain had a height difference of about 30 m at full scale, and a buffer area with an inclination angle of 10° was established upwind of the model (see Fig. 3.4(a)) [27]. The time step for unsteady simulations was set as 0.01 s, and the resulting CFL number was 1.8. Tetrahedral cells were constructed with the minimum size of 0.0016 m near buildings and terrain and then increasing to 0.03 m with the stretching ratio of 1.2. The total grid number was 3.94 million, as shown in Fig. 3.4(c). Grid-independence tests are detailed in the Supplementary Material.

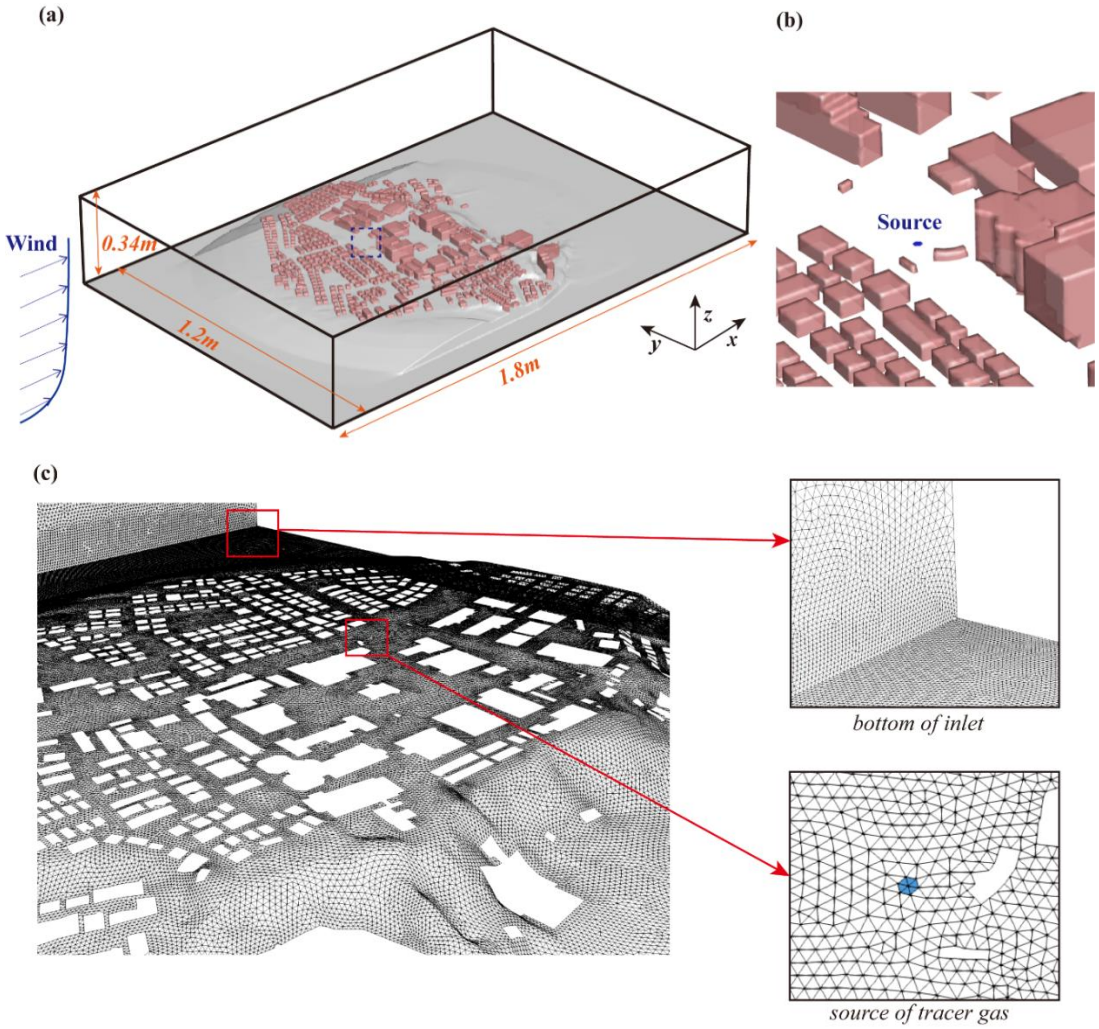

Fig. 3.4 (a) Computational domain of the real urban layout, (b) detailed configuration of source, and (c) grid distribution for the real urban layout case.

The bottom, lateral and boundaries of the computational domain and the building surfaces were set as no-slip walls. The top surface was set as symmetry [45,49,86], and the outlet was set as a zero-gradient condition. The inflow boundary conditions for the chosen turbulence models were set according to the experimental data [27] by means of the method detailed in Subsections 3.1.1, 3.1.2, and 3.1.3. For example, the fluctuation scales for LES in the x, y, z directions were set to 1.0, 0.8, and 0.6, respectively. The pollutant source was defined as the velocity inlet, and the speed was set as 0.088 m/s.

3.3. Results

To assess the performance of different turbulence models, this section compares the calculated time-averaged wind speed and tracer gas concentration fields for both the generic urban layout and the real urban layout with the wind tunnel data as a benchmark. NMSE and FAC2 were used as the metrics for quantitative analysis. To analyze the impact of the unsteadiness of the flow fields in the street canyons on the pollutant dispersion, we also compared the instantaneous pollutant dispersion patterns calculated by the transient models of URANS and LES. To satisfy the similarity law, as recommended by Meroney [102], the inflow wind speed should be sufficient to exceed a critical Reynolds number of 1.1×10^4. In this study, based on the wind tunnel experiment of the generic urban layout [96], the reference height of the inlet wind profile was 0.2 m, with a reference wind speed of 4.9 m/s. The resulting Reynolds number was 5.4×10^4, which satisfies the similarity law. For the real urban layout case [27], the reference height was 0.068 m, with a reference speed of 4.08 m/s, resulting in a Reynolds number of 1.5×10^4, also satisfying the similarity law.

3.3.1. Generic urban layout

3.3.1.1. Mean wind velocity and time-averaged concentration field

The calculated mean velocity magnitudes with different turbulence modelling approaches were compared with the measured data. The planes $y = 0.06$ m and $y = 0$ m were selected as

representative from all sampling locations, as this case is a generic street canyon. Fig. 3.5 shows the results in the plane y = 0.06 m, which represents a street canyon orientation that is parallel to the approaching wind. Error bars represent the standard deviation of the measured velocity. As in Fig. 3.5(a), at the height of 0.05 m, the wind speed obtained by LES was 2.40 m/s, comparable with the measured data (2.70 m/s). In contrast, the results from URANS and SRANS with the SST k-ω model were 3.03 m/s, overestimating the wind speed by 12.2% compared to the measured data. Similarly, the result from URANS and SRANS with the RNG k-ε model was both 3.72 m/s, resulting in an overestimation of 37.8%. Therefore, the LES approach exhibited the best agreement with the experimental data. For both the SST k-ω model and RNG k-ε model, the results obtained by SRANS and URANS approach were very similar, and they underestimated the wind speed near the ground. The conclusions obtained at other measurement points were similar, and the results from the other subplots in Fig. 3.5 showed the same pattern. Therefore, the 0.05m height in Fig. 3.5(a) was selected as a representative for detailed analysis.

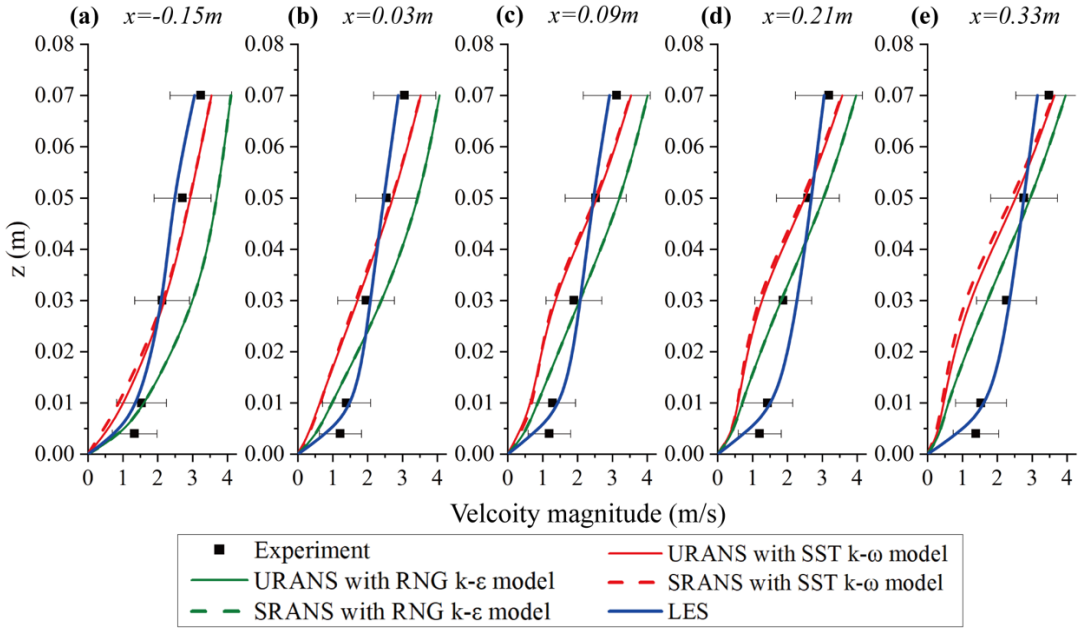

Fig. 3.5 Comparisons between simulated velocity magnitude and measured data on the plane y = 0.06 m along the plotting lines: (a) x = -0.15 m, (b) x = 0.03 m, (c) x = 0.09 m, (d) x = 0.21 m, and (e) x = 0.33m.

The results in the plane y = 0 m are shown in Fig. 3.6, representing a case in which the street canyon is located behind the buildings. As can be seen in Fig. 3.6(a), at the height of 0.03 m, the results of URANS and SRANS with the RNG k − ε model were 1.04 m/s and 1.09 m/s,

respectively, and the results from URANS and SRANS with the SST k − ω model were both 0.83 m/s. The LES result was 0.72 m/s. All these calculated results were similar to the measured value, which was 0.84 m/s. Therefore, in the street canyon located behind the buildings, the wind speeds obtained by all turbulence models were comparable to the measured data. The conclusions obtained in each subplot of Fig. 3.6 were similar. Therefore, we selected Fig. 3.6(a) as a representative case for detailed analysis.

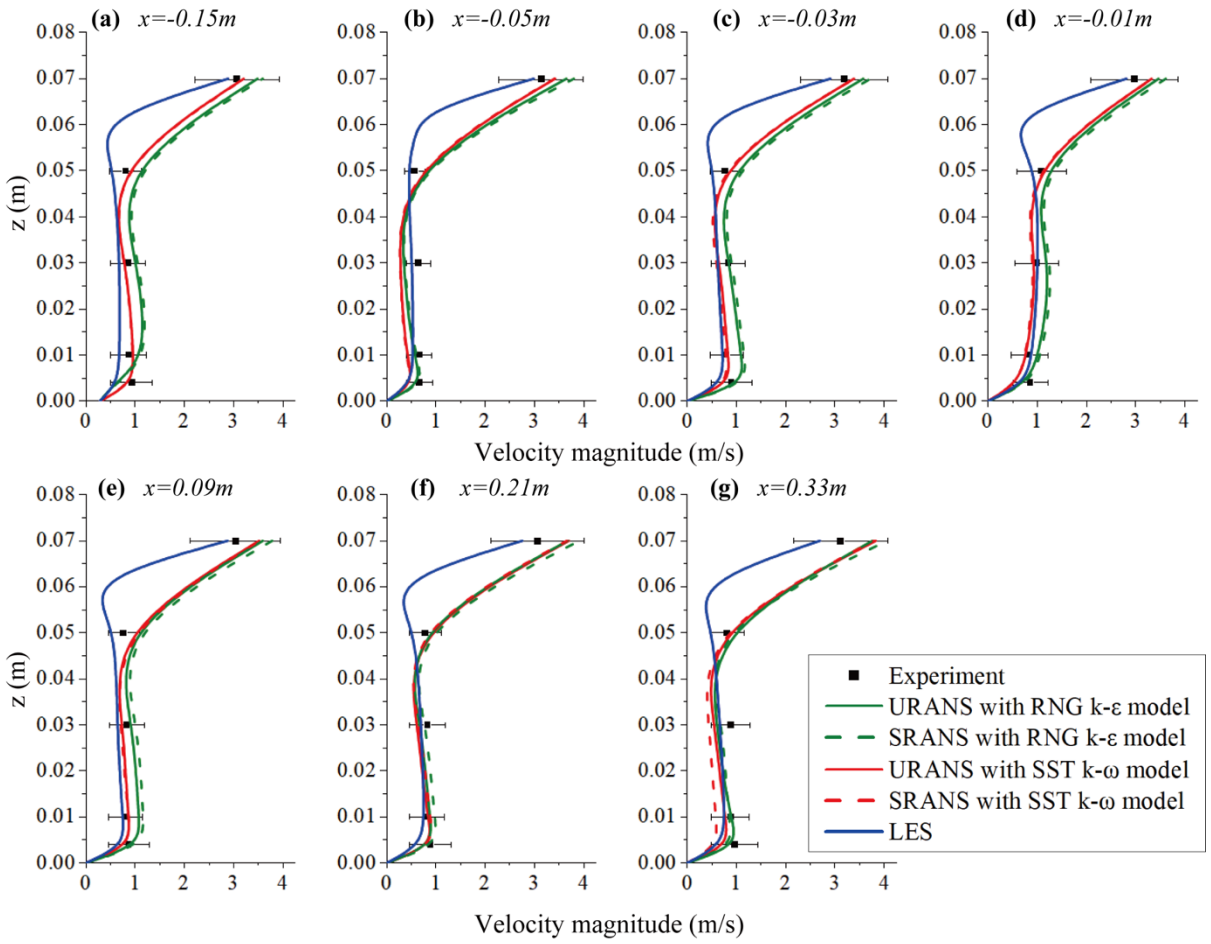

Fig. 3.6 Comparisons between simulated velocity magnitude and measured data on the plane y = 0 m along the plotting lines: (a) x = -0.15 m, (b) x = -0.05 m, (c) x = -0.03 m, (d) x = -0.01 m, (e) x = 0.09, (f) x = 0.21 m, and (g) x = 0.33 m.

In this study, the non-dimensional concentration was used to analyze the pollutant concentration distributions, and it was obtained by the following equation [44,45]:

$$c^* = \frac{c}{c_0} = \frac{c \cdot H_{ref}^2 \cdot u_{ref}}{Q_{gas}} \tag{3.16}$$

where c^* is the normalized concentration; c is the simulated gas concentration (ppm); c_0 is the reference concentration of tracer gas (ppm); Q_{gas} is the emission rate of tracer gas (m^3/s). Meanwhile, H_{ref} is the reference height of each case (m). Specifically, H_{ref} is the buildings' height (0.06 m) for the generic urban layout, and the height of the tallest building (0.068 m) for the real urban layout. In addition, u_{ref} is the velocity at the reference height (m/s). All the reference values can be found in the original studies [27,96].

To evaluate the pollutant dispersion within the street canyons, this study selected plotting lines with the highest density of measurement points ($x = -0.03$ m, $x = 0.09$ m, and $x = 0.21$ m, as shown in Fig. 3.1(c)) for comparison of the simulated time-averaged non-dimensional concentration with measured results. As the dispersion patterns observed at heights $z = 0.004$ m, $z = 0.01$ m, and $z = 0.03$ m were similar, only the results from $z = 0.03$ m were used for the following analysis, as shown in Fig. 3.7. Compared with LES and SRANS/URANS with the SST $k-\omega$ model, SRANS/URANS with the RNG $k-\varepsilon$ model significantly overestimated the pollutant concentration near the central plane $y = 0$ m. For example, in Fig. 3.7(a), at position $y = -0.06$ m, the c^* values obtained from SRANS/URANS with the SST $k-\omega$ model were 16.24 and 15.14, respectively, and the LES result was 10.77; these values were all comparable with the measured data (13.90). In contrast, the results of SRANS/URANS with the RNG $k-\varepsilon$ model were 62.83 and 59.25, respectively, approximately four times higher than the measured data. Additionally, based on the analysis above, we found that the results obtained from URANS and SRANS simulations using the same turbulence models were very similar. To sum up, SRANS/URANS with the SST $k-\omega$ model provided acceptable results that were comparable with LES and the measured data in calculating time-averaged concentration fields, demonstrating the promising accuracy of this approach. In contrast, SRANS/URANS with the RNG $k-\varepsilon$ model exhibited the worst performance in calculating pollutant dispersion in a generic urban layout.

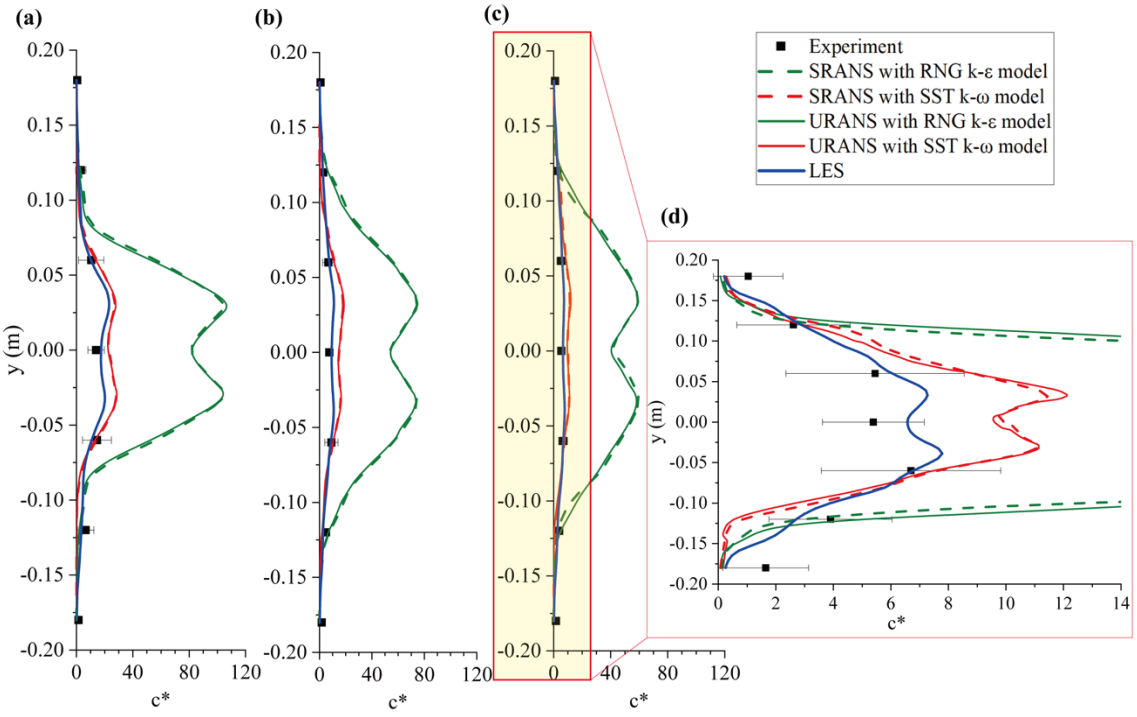

Fig. 3.7 Comparisons between the simulated normalized concentration and experimental data along the horizontal lines at the height of 0.03 m (HA/2): (a) x = -0.03 m, (b) x = 0.09 m, (c) x = 0.21 m, and (d) detailed view of marked area.

For quantitative assessments of turbulence models, three validation metrics have been prevalent: the friction of the prediction within a factor of 2 of the observations (FAC2), fractional bias (FB) and the normalized mean square error (NMSE) [13,48,49,103]. Therefore, these three parameters were calculated to evaluate the performance of the selected turbulence models in the present study. In regard to the first metric, if the ratio of the simulated result to the measured data falls between 0.5 and 2, the simulated result is considered acceptable, and FAC2 calculates the proportion of simulated results within this acceptable range. The ideal value is 1 (see Eq. (3.16)). FB is used to assess the bias between predicted and observed values, and the ideal value is 0 (see Eq. (3.17)). NMSE is widely used to indicate the deviation of the simulated results, and the ideal value is 0 (see Eq. (3.18)).

$$\mathrm{FAC2} = \frac{1}{N}\sum_{i=1}^{N} n_i \ \ with\ n_i = \begin{cases} 1, for\ 0.5 < \dfrac{P_i}{M_i} < 2, \\ 0, otherwise. \end{cases} \tag{3.17}$$

$$\mathrm{FB} = \frac{2 \times ([\mathrm{P}] - [\mathrm{M}])}{[\mathrm{P}] + [\mathrm{M}]} \tag{3.18}$$

$$\mathrm{NMSE} = \frac{[(M_i - P_i)^2]}{[M][P]} \tag{3.19}$$

Here, M_i and P_i are the measured and predicted results, respectively. The square brackets denote the average value of the dataset. N is the number of sampling points, and detailed values can be found in the original studies [27,96].

The metrics of simulated velocity magnitude and normalized concentration for each turbulence model are summarized in Table 3.1. LES accurately reproduced the velocity magnitude and concentration dispersion, with FAC2 of 0.99 for velocity and 0.84 for normalized concentration, FB values of 0.09 for velocity and -0.19 for normalized concentration, and NMSE values of 0.03 for velocity and 0.32 for normalized concentration. Furthermore, the discrepancies in velocity were found to be smaller than the discrepancies in concentration. For example, in terms of URANS/SRANS with the RNG $\mathrm{k} - \varepsilon$ model, although the velocity was accurately calculated, with FAC2 of 0.85, FB of -0.1, and NMSE around 0.1, the reproduction of the concentration field was the worst, with a FAC2 of only 0.17, FB around -1.4, and NMSE values around 13. Thus, the choice of turbulence modelling approach had a greater impact on the calculation of pollutant dispersion than on the calculation of wind speed.

To comprehensively investigate the computational costs of each selected turbulence modelling approach, the required time per iteration was compared. LES required about 3.5 times longer per iteration than URANS and 5.5 times longer than SRANS. For example, in the generic urban layout, LES took 2.50 seconds per iteration, while URANS took approximately 0.70 seconds, and SRANS approximately 0.45 seconds per iteration. Overall, LES had the highest computational cost, followed by URANS, with SRANS having the lowest cost.

Table 3.1 Validation metrics for different turbulence modelling approaches in the generic urban layout case.

Turbulence model	Velocity magnitude (m/s)			Normalized concentration			Required time per iteration (s)
	FAC2	FB	NMSE	FAC2	FB	NMSE	
SRANS with RNG $k-\varepsilon$	0.85	-0.10	0.12	0.17	-1.45	13.23	0.45
URANS with RNG $k-\varepsilon$	0.85	-0.10	0.10	0.17	-1.42	13.13	0.47
SRANS with SST $k-\omega$	0.64	0.28	0.20	0.57	-0.39	2.03	0.61
URANS with SST $k-\omega$	0.67	0.26	0.18	0.58	-0.36	1.89	0.78
LES	0.99	0.09	0.03	0.84	-0.19	0.32	2.50

3.3.1.2. Instantaneous concentration field

To assess the instantaneous solutions obtained from the transient models, URANS with the RNG $k-\varepsilon$ model, URANS with the SST $k-\omega$ model, and LES, the calculated non-dimensional concentration patterns are shown in Fig. 3.8. Significant differences can be seen in the results of URANS and LES. The LES provided more diffusive dispersion patterns than URANS, especially in the lateral direction. Specifically, Fig. 3.8(e) and (f) show that small-scale turbulence motions were resolved by the LES approach, and the pollutant was carried by these small-scale fluctuations over a greater spanwise distance compared to the four URANS results. As displayed in Fig. 3.7(d), the concentrations calculated by SRANS/URANS with the SST $k-\omega$ model and with the RNG $k-\varepsilon$ model approached 0 faster than the concentrations calculated by LES. For comparisons of the selected RANS approach, the dispersion patterns calculated by URANS with the RNG $k-\varepsilon$ model did not change over time, while the URANS with the SST $k-\omega$ model successfully calculated large-scale fluctuations (see Fig. 3.8(a) to (d)). This phenomenon was also reported by Tominaga [49]. He found that the RNG $k-\varepsilon$ model overpredicted the turbulence kinetic energy near the building corners, and this overestimation suppressed the calculation of periodic motions. Moreover, the concentration along the downstream direction obtained by URANS with the RNG $k-\varepsilon$ model was much higher than that obtained by the other models. For example, at the location $x = 0.21$ m, $y = 0$ m, $z = 0.03$ (referred to Fig. 3.1), the c^* calculated by URANS with the SST $k-\omega$ model and LES were 9.63 and 6.58, respectively. In contrast, the c^* calculated by URANS with the RNG $k-\varepsilon$ model was 40.51, significantly higher than the results from the other two

approaches. Thus, pollutants calculated by the RNG k − ε model tended to be directly blown away by the airflows. To sum up, in the building arrays, the turbulence motions calculated by different turbulence models played an important role in the dispersion patterns of air pollutant.

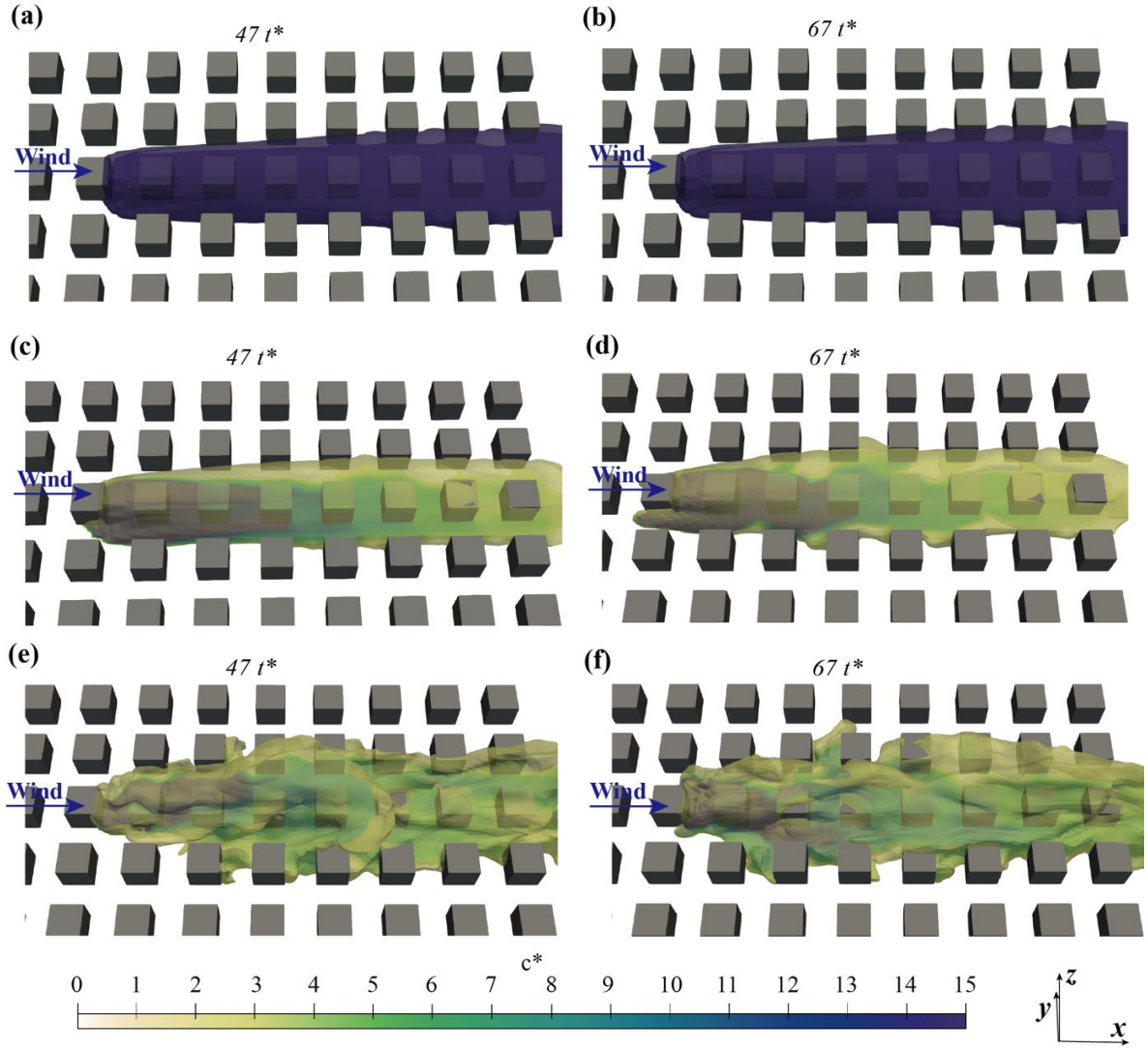

Fig. 3.8 Instantaneous concentration dispersion patterns calculated by: (a) URANS with the RNG k-ε model at 47t* and (b) 67t*; (c) URANS with the SST k-ω model at 47t* and (d) 67t*; (e) LES model at 47t* and (f) 67t*.

3.3.2. Real urban layout

3.3.2.1. Mean wind velocity and time-averaged concentration field

To evaluate the performance of URANS, SRANS and LES in the real urban layout, Fig. 3.9 compares wind speed calculated by selected turbulence models with measured data at 15 sampling points. The results of LES were mostly comparable with the experimental data, while those of the selected RANS approaches significantly deviated from the measured data at some points. For example, for SRANS/URANS with the RNG $k-\varepsilon$ model, the greatest discrepancy was observed at point 1. The measured wind speed was 1.30 m/s at this point, and the value calculated by LES was 1.41 m/s, which was comparable with the measured data. In contrast, for both URANS and SRANS with the RNG $k-\varepsilon$ simulations, the result was 0.33 m/s, and it was 74.6% lower than the benchmark. Additionally, for SRANS/URANS with the SST $k-\omega$ model, the greatest discrepancy occurred at point 9, where the wind speed was measured at 0.53 m/s. At this point, the LES value was 0.71 m/s, closely matching the experimental data. However, the values from URANS and SRANS with the SST $k-\omega$ model were 1.84 m/s and 1.74 m/s, respectively, nearly triple the measured data. Thus, LES performed best in calculating wind speed in the real urban layout.

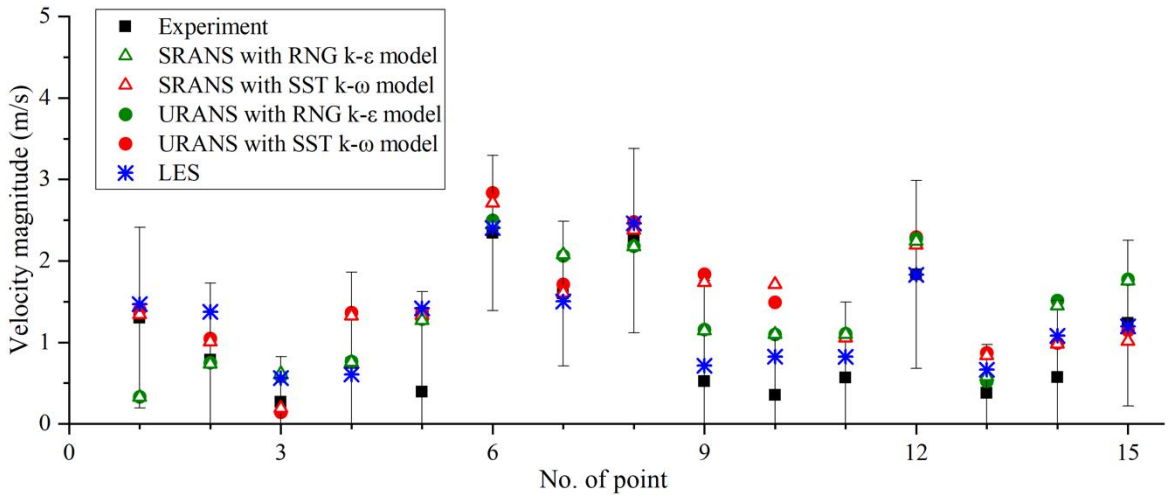

Fig. 3.9 Comparisons of simulated velocity magnitude and measured data at sampling points.

To evaluate the performance of different models in calculating mean concentration distributions in the real urban layout, we compared the non-dimensional concentration c^* obtained by the selected turbulence modelling approaches with the experimental data, and the

results are shown in Fig. 3.10. As in the generic urban layout, steady-state and unsteady-state simulations using the same RANS scheme (either the RNG k − ε model or SST k − ω model) provided very similar pollutant concentrations. Additionally, SRANS/URANS with the RNG k − ε model significantly overpredicted the streamwise concentration (at point 2, point 7 and point 8). For instance, at point 7, the measured c^* was 1.57. However, the c^* values calculated by SRANS/URANS with the RNG k − ε model were 11.14 and 11.24, respectively, approximately 7.1 times higher than the experimental data. However, in contrast with the building-array scenario, the results of LES approach and SRANS/URANS with the SST k − ω model differed significantly from one other in the real urban layout. For example, at point 1, the measured c^* was 3.04. The calculated values from SRANS/URANS with the SST k − ω model were both 0.001, which was significantly lower than the measured value, whereas the LES approach provided a result of 1.67. Although the LES result was still lower than the measured value, it performed better than all the selected RANS models. Thus, the LES approach performed the best, while the prediction capability of SRANS/URANS with the RNG k − ε model and SST k − ω model was limited in calculating pollutant dispersion in real urban layouts.

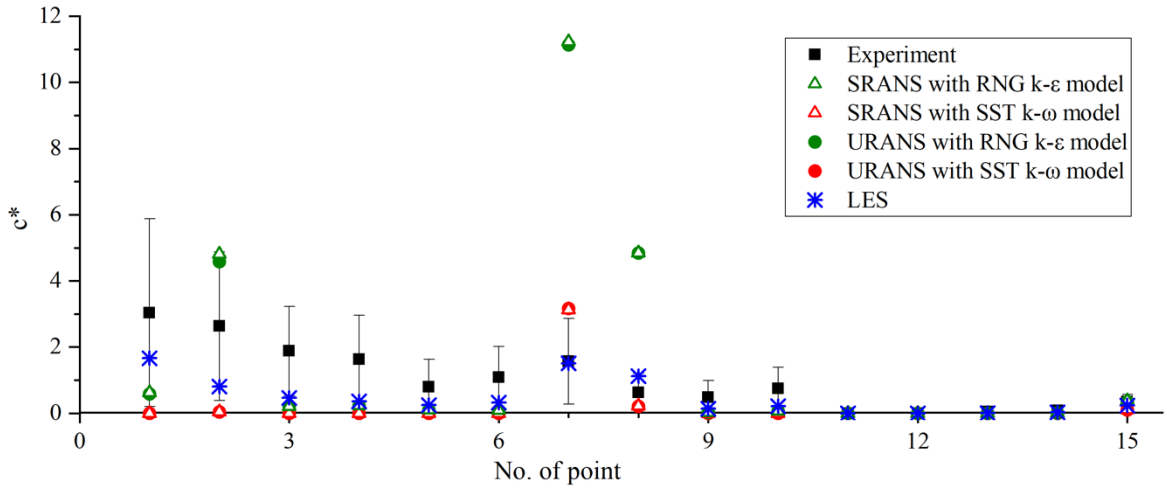

Fig. 3.10 Comparisons between the simulated normalized concentration and experimental data at sampling points.

For quantitative analyses, the validation metrics of calculated wind speed and normalized concentrations are shown in Table 3.2. An inconsistency was observed between the FB values and the FAC2 and NMSE values for normalized concentration. Specifically, for SRANS/URANS with RNG k − ε model, the NMSE value was 5.69, much higher than the

LES value of 1.17. However, the FB value was around 0.4, closer to zero compared to LES, which had an FB of -0.65. Referred to Fig. 3.10, this discrepancy arose because SRANS/URANS with the RNG $k-\varepsilon$ model significantly overestimated pollutant concentrations at points 2, 7, and 8, while underestimating concentrations at other points. This resulted in the FB value appeared close to zero, making the FB metric not representative in this case. Therefore, we used NMSE and FAC2 values for further analysis.

The selection of turbulence models had a more significant influence on the calculation of pollutant dispersion than on the calculation of wind speed. For example, the FAC2 of SRANS/URANS with the RNG $k-\varepsilon$ model, SRANS/URANS with the SST $k-\omega$ model, and LES were 0.6, 0.73 and 0.8, respectively; these values were comparable with each other. However, the selected models performed differently in the calculation of concentration. LES had the highest FAC2 (0.4) and the lowest NMSE (1.17). In contrast, the NMSE of all four RANS models was significantly higher than that of LES, at approximately 7.8 for SRANS/URANS with the RNG $k-\varepsilon$ model and 5.69 for SRANS/URANS with the SST $k-\omega$ model. i.e., about 6.7 times and 4.9 times that of the LES approach, respectively. Thus, even though the selected modelling approaches provided similar results for wind speed in the real urban layout, LES performed the best in pollutant dispersion simulations.

Table 3.2 Validation metrics for different turbulence modelling approaches in real urban layout case.

Turbulence model	Velocity magnitude (m/s)			Normalized concentration			Required time per iteration (s)
	FAC2	FB	NMSE	FAC2	FB	NMSE	
SRANS with RNG $k-\varepsilon$	0.60	0.27	0.23	0.33	0.41	5.69	2.80
URANS with RNG $k-\varepsilon$	0.60	0.27	0.23	0.33	0.39	5.69	3.24
SRANS with SST $k-\omega$	0.73	0.35	0.26	0.20	-1.23	7.81	3.95
URANS with SST $k-\omega$	0.73	0.37	0.26	0.20	-1.23	7.79	4.16
LES	0.80	-0.22	0.12	0.40	-0.65	1.17	14.35

3.3.2.2. Instantaneous concentration field

To evaluate the unsteadiness of pollutant concentration distributions provided by transient models in the real urban layout, the instantaneous normalized concentration c^* obtained by URANS with the RNG k − ε model, URANS with the SST k − ω model, and LES are shown in Fig. 3.11. Similar to the results in the generic urban layout, URANS with the RNG k − ε model provided the highest concentrations in the downstream area. For example, at point 2 (referred to Fig. 3.3), the c^* calculated by URANS with the SST k − ω model and LES were 0.04 and 0.81, respectively. In contrast, URANS with the RNG k − ε model provided a much higher c^* value of 4.82, significantly higher than the results from the other two approaches. Moreover, the results of URANS with the RNG k − ε model remained unchanged over time. The LES approach provided the most diffused dispersion patterns in the lateral direction. Specifically, only the LES approach predicted the right-side dispersion from the source. In contrast, the other models predicted that the pollutant would be directly blown away by airflows. However, unlike in building arrays, the dispersion patterns calculated by URANS with the SST k − ω model did not change over time in the real urban layout, as shown in Fig. 3.11(c) and (d). The reason may have been that in real urban layouts, large-scale fluctuations are disturbed by the complex arrangement of buildings. Further discussion can be found in Section 3.4. To sum up, turbulence models should be carefully chosen when calculating pollutant dispersion patterns in real urban layouts.

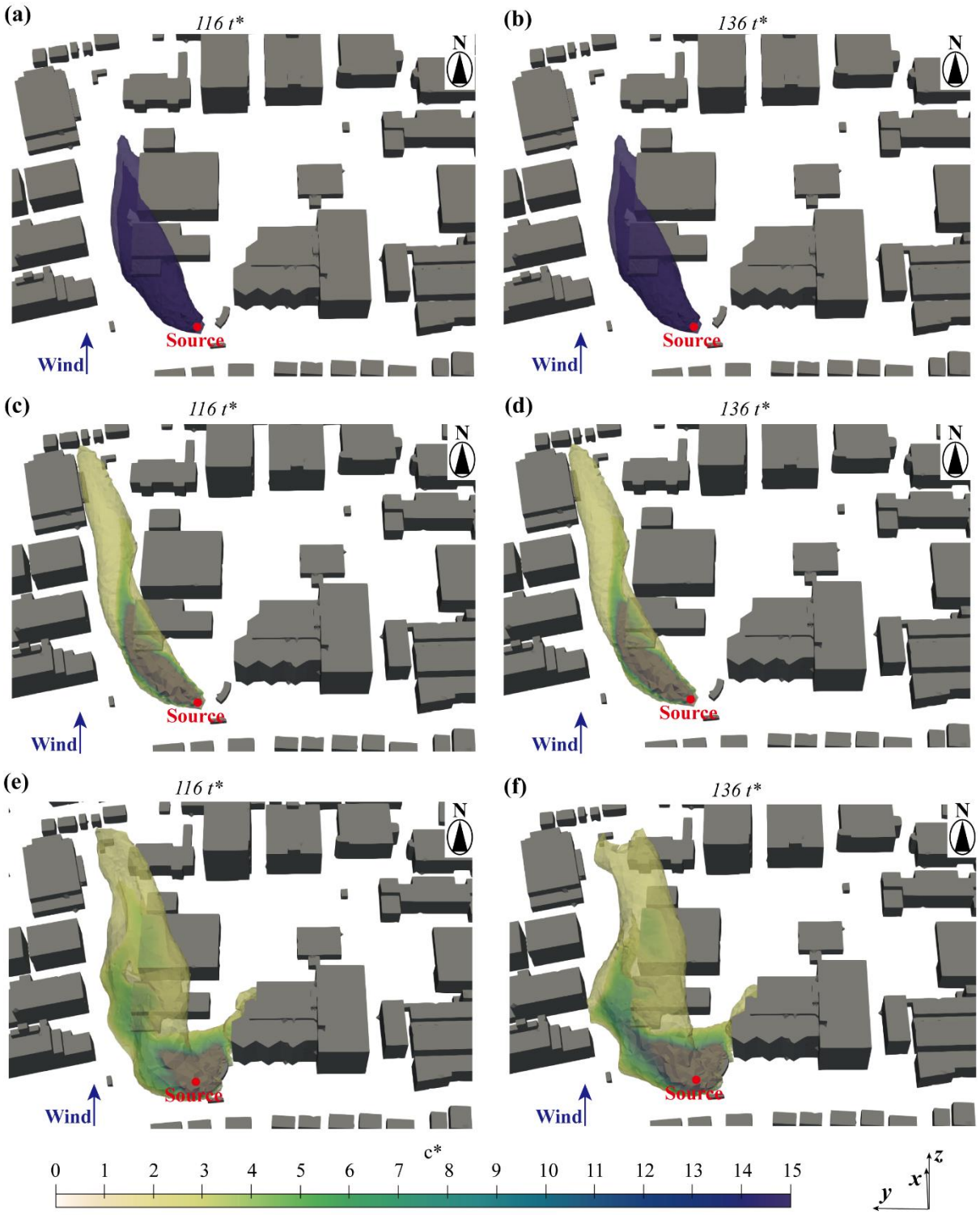

Fig. 3.11 Instantaneous concentration dispersion patterns calculated by: (a) URANS with the RNG k-ε model at 116t* and (b) 136t*; (c) URANS with the SST k-ω model at 116t* and (d) 136t*; (e) LES model at 116t* and (f) 136t*.

3.4. Discussion and limitations

This study obtained instantaneous concentration fields from URANS and LES in a generic urban layout and a real urban layout. Note that URANS with the SST $k-\omega$ model performed differently in the two chosen urban layouts. In the building arrays, it captured large-scale fluctuations in the concentration fields over time, whereas in the real urban layouts, the concentration field remained unchanged over time. To address the reasons for this phenomenon, Fig. 3.12 compares the instantaneous velocity fields and streamlines calculated by URANS with the SST $k-\omega$ model and LES in the considered urban layouts. For the building array, the region from $x = -0.15$ m to $x = 0.33$ m and from $y = 0$ m to $y = 0.12$ m, at $z = 0.004$ m, was selected as representative due to the repeatability of airflows in the generic urban layout. For the real urban layout, the plane at a height of 2 m at full scale was chosen, as it corresponds to a pedestrian-level height. As shown in Fig. 3.12(b) and (d), small-scale velocity fluctuations calculated by LES were observed in both the generic urban layout case and the real urban layout case. As analyzed in Sections 3.3.1.2 and 3.3.2.2, capturing small-scale velocity fluctuations is crucial for accurately simulating pollutant dispersion, as these fluctuations enhance the ability to predict lateral pollutant dispersion. However, for the results of URANS with the SST $k-\omega$ model, large-scale velocity fluctuations were only observed in the generic urban layout, whereas these fluctuations were absent in the real urban layout. This was because URANS with the SST $k-\omega$ model can only capture large-scale and periodic velocity fluctuations [13,50]. However, in the real urban layout, the large-scale velocity fluctuations were disturbed by the complex presence of buildings. Therefore, the influence of large-scale unsteady flows on pollutant dispersion was small, and changes in the URANS results were negligible in the calculation of pollutant dispersion in the real urban layout.

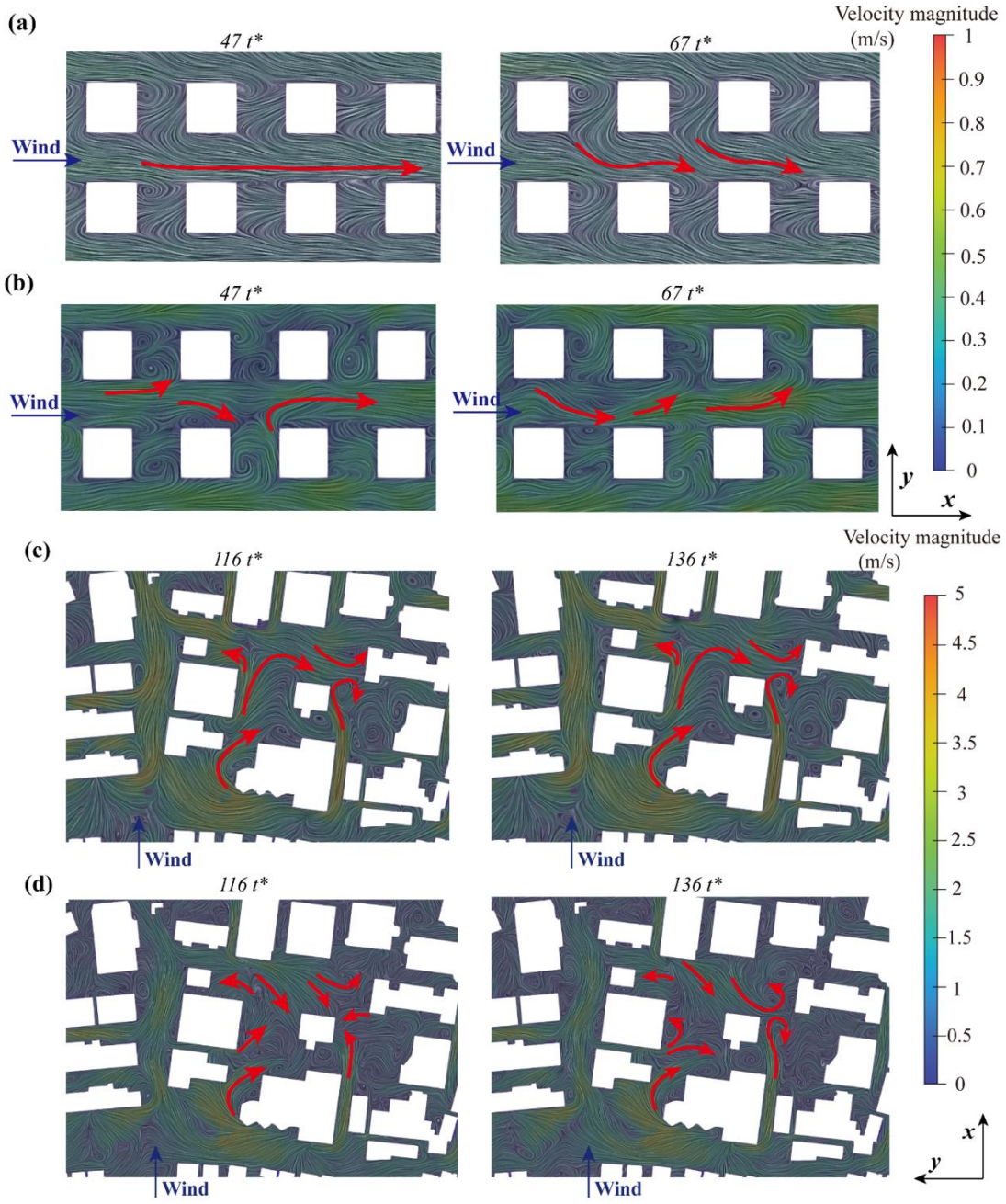

Fig. 3.12 Instantaneous velocity fields for the generic urban layout calculated by (a) URANS with the SST k−ω model and (b) LES, and for the real urban layout calculated by (c) URANS with the SST k−ω model and (d) LES.

To compromise computational efficiency and simulation accuracy, the perturbations at the inflow boundary were introduced using a fluctuation scale for LES approach. However, previous studies have showed that inflow turbulence generation techniques (ITGTs) significantly impact the accuracy of LES results. For example, Bazdidi-Tehrani et al. [104] investigated four ITGTs for calculating flow fields and pollutant dispersion in a street canyon. Their findings showed that the Vortex Method was the most accurate ITGT but also the most

computationally expensive among all the selected ITGTs. In contrast, other ITGTs were less effective in capturing the canyon vortex compared to Vortex Method, leading to an underestimation of pollutant dispersion. The general underestimation of pollutant concentration in the real urban layout by LES can be attributed to the chosen of ITGT. Moreover, this study only considered a single case in a real urban layout with a fixed inflow wind direction, due to limited wind tunnel experimental data. However, urban flow patterns can vary significantly with changing meteorological conditions and different building configurations. Therefore, it is necessary to conduct extensive wind tunnel experiments with different inflow wind conditions and varying urban layouts, in order to better assess the performance of these turbulence modelling approaches in pollutant dispersion simulations.

In this study, we conducted a detailed comparison between URANS and SRANS with selected RANS schemes. We found that although URANS with the SST $k-\omega$ model calculated large-scale fluctuations over time in a generic urban layout, the time-averaged results from URANS and SRANS showed no significant differences. This indicates that although these fluctuations impact the instantaneous pollutant concentration in a building array, they make a minimal contribution to the time-averaged pollutant dispersion. At this stage, URANS can serve as a justifiable alternative to LES for calculating time-averaged fields in the generic urban layout with simple building configurations. For the real urban layout where building arrangements are complex, URANS cannot be considered a reliable alternative to LES. This can be caused by insufficient ability of URANS to capture small-scale fluctuations and turbulence structures. Improving URANS's ability to handle small-scale fluctuations and turbulence viscosity could enhance its performance in complex scenarios. Due to the lack of experimental data on instantaneous pollutant concentration, the accuracy of the fluctuations and instantaneous pollutant dispersion provided by URANS with the SST $k-\omega$ model remains unclear. Therefore, collecting instantaneous concentration data and further investigating URANS approach is essential.

Furthermore, turbulence motions provided by different turbulence modelling approaches play an importance role in pollutant dispersion in the lateral direction. In practice, pedestrian locations often align with the lateral direction of vehicle traffic. The specific impact of calculated lateral dispersion on pollutant exposure for pedestrians remains unclear. Therefore,

future studies should explore the applicability of various turbulence modelling approaches in order to elucidate their implications for pollutant exposure at pedestrian level.

3.5. Summary

This investigation aimed to evaluate the performance of SRANS/URANS with the RNG $k-\varepsilon$ model, SRANS/URANS with the SST $k-\omega$ model, and LES in calculating pollutant dispersion in street canyons with generic and real urban layouts. For each layout, wind tunnel data on airflows and pollutant concentrations served as the benchmarks. We also compared the instantaneous concentration fields obtained from URANS and LES approaches. Within the scope of this chapter, the following conclusions can be drawn.

- In both generic and real urban layouts, the RNG $k-\varepsilon$ model and SST $k-\omega$ model provided similar results for time-averaged wind speed and concentration distributions in SRANS and URANS approaches.
- In both generic and real urban layouts, among all the selected RANS models, SRANS/URANS with the SST $k-\omega$ model showed best agreement with measured data in calculating wind speed. LES performed best in calculating wind speed and pollutant dispersion, but it was the most time-consuming model.
- In the generic urban layout, URANS with the SST $k-\omega$ model captured the large-scale fluctuations, while instantaneous results from URANS with the SST model did not change over time in the real urban layout.

CHAPTER 4. Propose a combined WRF and CFD method for calculating urban wind distributions

To calculate the wind distributions in real urban environments, it is essential to provide the realistic inflow boundary conditions for CFD simulations. In this chapter, the potential of a combined WRF and CityFFD method (WRF-CityFFD) was evaluated. The WRF and CityFFD models were first validated by two sets of experimental data from field measurements and wind tunnel tests. The validated models were then employed in the WRF-CityFFD method to calculate the wind distribution in the Kowloon district of Hong Kong within an area of 3.5 km × 2.4 km. The wind speed data at two weather stations in the calculation domain was used as a benchmark to evaluate the combined method. For comparison, CityFFD with inflow boundary conditions from a semi-empirical method (semi-empirical-CityFFD) was also evaluated. Finally, this chapter discussed the applicability of the combined method.

4.1. Methodology

4.1.1. CityFFD

Fast fluid dynamics (FFD) is a unique algorithm based on CFD, and the semi-Lagrangian approach is used for advection terms in the Navier-Stokes equations [105,106]. Extensive validation efforts have demonstrated the accuracy and computing efficiency of the FFD approach [93,105–109]. Dai et al. [93] evaluated the performance of the traditional CFD and FFD for outdoor airflow and pollutant dispersion using experimental wind tunnel data as the benchmark. They found that the use of FFD with a proper turbulence model can reduce computing time without sacrificing accuracy. Therefore, FFD simulations have been used for urban wind modelling up to the scale of several kilometers. For example, Mortezazadeh et al. [110] developed a simulation tool named City Fast Fluid Dynamics (CityFFD), and they simulated the urban microclimate in a region of 3 km × 3 km.

The CityFFD model solves the following continuity, momentum, and energy equations for incompressible flows [72]:

$$\nabla \cdot \mathbf{V} = 0 \tag{4.1}$$

$$\frac{\partial \mathbf{V}}{\partial t} + (\mathbf{V} \cdot \nabla)\mathbf{V} = -\nabla \mathrm{P} + \left(\frac{1}{Re} + v_t\right)\nabla^2 \mathbf{V} - \frac{Gr}{Re^2} T \tag{4.2}$$

$$\frac{\partial T}{\partial t} + (\mathbf{V} \cdot \nabla)T = \left(\frac{1}{Re \cdot Pr} + \vartheta_t\right)\nabla^2 T \tag{4.3}$$

where $\mathbf{V}$, T, P and t are the velocity, temperature, pressure and time, respectively; Re, Gr and Pr are the dimensionless Reynolds number, Grashof number, and Prandtl number, respectively; and v_t and ϑ_t are turbulence-related parameters, i.e., turbulent viscosity and turbulent thermal diffusivity.

CityFFD adopts the semi-Lagrangian method for the advection term in Eqs. (4.2) and (4.3). Therefore, no iteration is needed to calculate the velocity field, and computing costs are reduced [111]. The split scheme for the semi-Lagrangian method is shown in Eqs. (4.4) and (4.5) [106]:

$$\frac{\partial \emptyset}{\partial t} + (\mathbf{V} \cdot \nabla)\emptyset = \frac{d\emptyset}{dS} \tag{4.4}$$

$$S^n \approx S^{n+1} - \mathbf{V}\Delta \mathrm{t} \tag{4.5}$$

where $\emptyset$ refers to the velocity or temperature in Eqs. (4.2) and (4.3); and S represents the characteristic curve of the fluid particle, based on which S^n and S^{n+1} are the positions of the particle at times n and n+1, respectively. The detailed high-order interpolation scheme can be found in our previous work [105,109,112]. It has been proven that the applied 3rd-order backward and forward sweep interpolation scheme has an accuracy comparable to that of the 4th-order scheme and could significantly reduce the numerical errors and computing time when simulations are conducted with coarse grids and large time steps. A Poisson equation is used for updating pressure domains [109].

Large-eddy simulation (LES) was found to be potentially more accurate than Reynolds-averaged Navier–Stokes models for outdoor simulations [47]. Therefore, LES was adopted as the turbulence model in the present study. As CityFFD uses a high-order interpolation scheme,

the Courant–Friedrichs–Lewy (CFL) number is recommended to be between 1 and 10 [110], and this study used 6.75. The turbulence viscosity is calculated as follows [113]:

$$v_t = (C_s \times l)^2 \left|\overline{S}\right| \tag{4.6}$$

where C_s is the Smagorinsky constant, typically between 0.1 and 0.24 [47], and equal to 0.18 in this study; l is the filter width; and $\overline{S}$ is the large-scale strain rate. For calculating the filter width l and strain rate $\overline{S}$, the following equations are used here [107]:

$$l = (\Delta x \Delta y \Delta z)^{1/3} \tag{4.7}$$

$$\overline{S} = \frac{1}{2}\left(\frac{\partial u_i}{\partial x_j} + \frac{\partial u_j}{\partial x_i}\right) \tag{4.8}$$

where $\Delta x, \Delta y, \Delta z$ are the discrete lengths in the x, y, and z directions, respectively. Meanwhile, the i-index indicates the x, y, and z directions.

4.1.2. Inflow boundary conditions for CityFFD

This section describes two methods applied in this study for generating inflow boundaries for the CFD models, the semi-empirical method (for semi-empirical-CityFFD) and the mesoscale modelling (for WRF-CityFFD). As the tallest building of the target complex urban area in this study was 284 m, both methods approximated the wind profile at the CFD inlet boundary as a power law. The semi-empirical method used the wind speed measured by the windward weather station nearest to the CFD domain and an empirical power-law coefficient. For the combined method of CFD and mesoscale modelling, both the wind speed and the power-law coefficient at the inlet boundary were extracted from WRF simulations in this study.

4.1.2.1. Semi-empirical method

The wind profile was approximated as a power law, as shown in Eq. (4.9) [9].

$$U(z) = U_{ref}\left(\frac{z}{z_{ref}}\right)^{\alpha} \tag{4.9}$$

where $U(z)$ is the wind velocity $(\mathrm{m/s})$ at the height of z, U_{ref} is the velocity $(\mathrm{m/s})$ at a reference height z_{ref} (m), and α is the power-law coefficient. In this method, U_{ref} was determined by the windward weather station closest to the CFD domain, and z_{ref} was the height of the wind-measurement point at the station. Meanwhile, α was selected in accordance with the terrain category and the roughness. According to previous studies, as the land surface changes from smooth (e.g., sea) to rough (e.g., downtown areas), the value of α gradually increases from 0.1 to 0.5 [59].

4.1.2.2. From mesoscale modelling: WRF

In the mesoscale modelling method, the WRF model was used for calculating meteorological conditions, as shown in Fig. 4.1. The WRF model is a powerful mesoscale numerical weather prediction system consisting of advanced physics schemes and multi-physics parameterizations for modelling major atmosphere processes with grid spacing from hundreds of meters to hundreds of kilometers [66,68,114]. For the land surface, planetary boundary layer, atmospheric and surface radiation, microphysics, and cumulus convection, WRF offers various physics options that have been thoroughly proven in previous research [115]. To obtain the wind profile at the inflow boundary, U_{ref}, z_{ref}, and α were all extracted from WRF results. As this work focuses on urban wind fields, the wind profiles in the bottom portion of the ABL, below a height of 350 meters, were utilized to obtain α. η in the flow chart represents the vertical layer used in the WRF model, and it was established according to the pressure gradient [116].

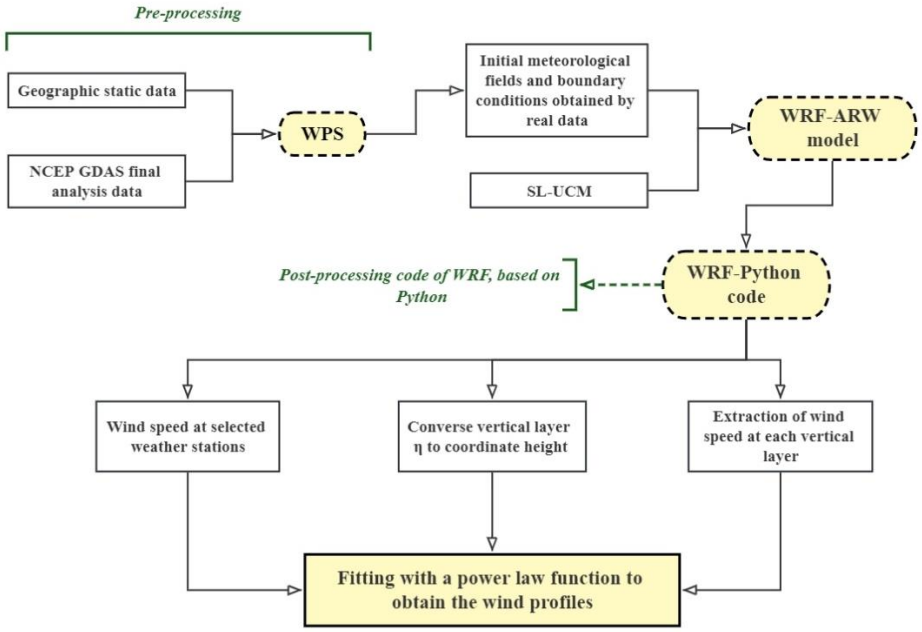

Fig. 4.1 Flowchart to obtain inflow boundary conditions from WRF simulation.

To rationally reproduce the meteorological phenomena, the selected physical parameterization for WRF is summarized in Table 4.1. In this study, the initial and lateral boundary conditions to force the WRF simulation were obtained from the NCEP GDAS final analysis with 0.25-degree horizontal resolution and 6-hour temporal resolution [117]. The Noah land surface model (LSM) provides surface sensible and latent heat flux as well as skin temperature as the lower boundary [118], and the urban canopy model (UCM) provides the urban friction based on the land cover/land use at the sub-grid scale. This study used the integrated model (SL-UCM) to determine the momentum fluxes of the urban canopy [119]. When these basic models are integrated into the WRF, the outputs can be directly adapted to the CityFFD model.

Table 4.1 Physical parameterization of the WRF model.

Category	Description
Planetary boundary layer scheme	Mellor-Yamada-Janjic scheme [120]
Microphysics	Lin scheme [121]
Cumulus parameterisation	Grell-Devenyi ensemble schemes [122]
Shortwave and longwave radiation	RRTM [123]
Land surface model	Noah [117]
Urban canopy model	SL-UCM [119]
Advection scheme	Runge–Kutta 3rd order

4.2. Model validation

4.2.1. Mesoscale modelling: WRF

To validate the mesoscale model, we chose the Kowloon peninsula domain as the WRF study domain, as shown in Fig. 4.2(a). We used WRFv4.0 to calculate the meteorological conditions, and the wind speed measured by the four weather stations in our study area was employed as the benchmark. Star Ferry (SF) and Shell Oil Depot (SOD) were located near the coastal areas, while the Hong Kong Observatory (HKO) and King's Park (KP) were situated in the downtown areas and surrounded by high-rise buildings (see Fig. 4.2(a)). The exact geographical locations of the weather stations are summarized in Table 4.2. As shown in Fig. 4.2(b), three-nested domains were configured for WRF calculation using grid spacings of 1.8 km (113×128 grid points), 0.6 km (127×148 grid points), and 0.2 km (112×112 grid points) for a parent domain (d01) and two nested domains (d02, d03), respectively. A two-way coupling strategy [116] was adopted for the adjacent domains. A total of 34 sigma vertical levels were used for all domains, and 13 of the layers were under 1 km in height. Three typical calm wind days (from 08:00 on 19 October to 14:00 on 22 October 2016) were simulated to represent typical wind conditions in Hong Kong. The mean daily wind speed during selected simulation period was 2.95 m/s, 3.70 m/s and 9.04 m/s, respectively. According to the Hong Kong Observatory, the mean daily wind speed in Hong Kong ranges from 2 m/s to 10 m/s. Therefore the chosen days are typical in Hong Kong. The first 26 hours were taken as the spin-up period. WRF results were recorded every 20 minutes.

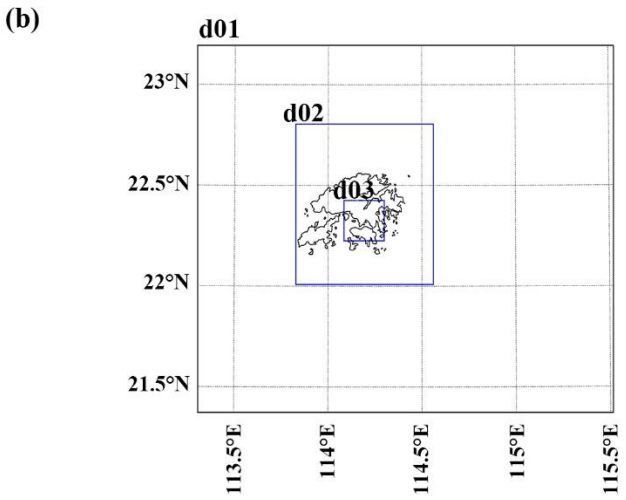

Fig. 4.2 (a) Four weather stations located in the innermost domain and (b) domain setup of the WRF

Wind measurement data with a temporal resolution of one minute was available from local authorities. The most recent 20-minute averaged wind speed was used to represent the wind speed at this time point. For instance, the wind speed at 10:00 was calculated as the average wind speed from 09:40 to 09:59. Fig. 4.3 compares the measured wind speed and the WRF-simulated results over time for the four weather stations. The simulation results at all four stations captured the trend in the wind speed as it gradually increased from 20 October to 21 October and then decreased. The simulated results exhibited the best agreement with the measured data at the SF station. However, WRF significantly overpredicted the wind speed for HKO and KP during the period from 23:20 on 20 October to 00:20 on 22 October. The largest discrepancies were 8.24 m/s and 10.66 m/s for HKO and KP, respectively, occurring at 08:20 and 09:00, respectively, on 21 October. As shown in Fig. 4.3, the measured wind speed in the downtown area (HKO and KP) was relatively stable compared with that in the upstream station (SF). This phenomenon may be attributed to the complexity of the urban layouts, especially associated with the high-rise buildings in Kowloon, and it is consistent with the field test by He et al., [64]. However, in WRF simulations, the urban canopy was parameterized by the drag force with the specific value of building height of 10 m [119]. A high consistency of simulated wind speed can be found at the upstream station (SF) and downtown stations (HKO and KP). Therefore, the discrepancies between measured data and simulated results could be caused by the urban canopy model used in WRF.

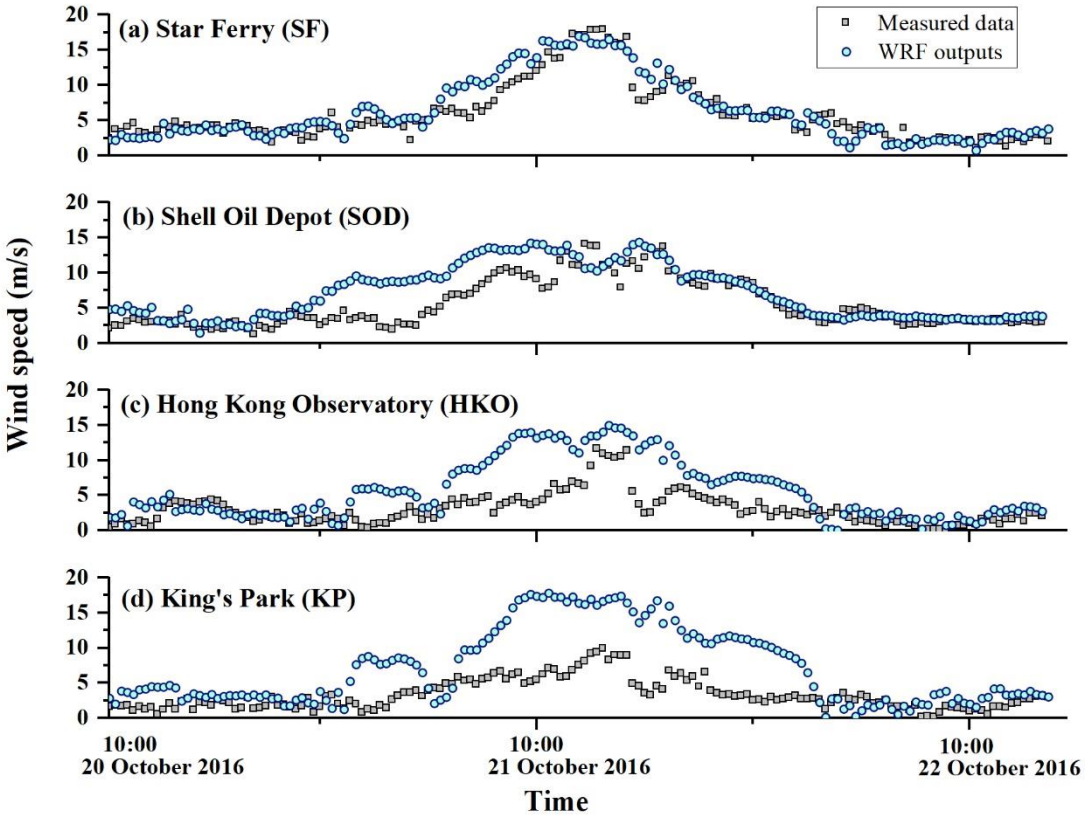

Fig. 4.3 Comparison of measured wind speed and WRF-simulated results over time for the four weather stations: (a) SF, (b) SOD, (c) HKO, and (d) KP.

To quantitatively analyze the performance of the mesoscale model, the mean bias error and the root mean square error were prevalently used [71,124]. Thus, these two parameters were calculated in this work to evaluate the performance of WRF simulations. The mean bias error (MBE) assesses whether the simulated wind velocity is overestimated or underestimated compared to the measured values (see Eq. (4.10)). The root mean square error (RMSE) is widely used to indicate the deviation of the simulated results (see Eq. (4.11)).

$$\mathrm{MBE} = \frac{\sum_{i=1}^{n}\left(U_i^S - U_i^M\right)}{n} \tag{4.10}$$

$$\mathrm{RMSE} = \sqrt{\frac{\sum_{i=1}^{n}\left(U_i^S - U_i^M\right)^2}{n}} \tag{4.11}$$

where U_i^S and U_i^M are the simulated and measured wind velocity, and n is the number of measured data points for one sampling location. In this study, n was 158. As summarized in Table 4.2, WRF exhibited the best performance at SF and the worst at HKO. The MBE and

RMSE for SF were 0.58 m/s and 1.79 m/s, respectively, and those for HKO were 3.89 m/s and 5.49 m/s, respectively. Wong et al. [70] recently compared WRF results with measured data for five locations on a university campus in Singapore. The MBE in their study ranged from 2.58 to 3.90 m/s, and the RMSE from 2.69 to 4.13 m/s. Thus, our WRF results showed similar accuracy to those in the literature for dense urban areas.

Table 4.2 Geographical locations, MBE and RMSE at each weather station.

Station Name	Star Ferry (SF)	Shell Oil Depot (SOD)	Hong Kong Observatory (HKO)	King's Park (KP)
Position	Coastal	Coastal	Downtown	Downtown
Latitude (°N)	22.29	22.34	22.30	22.31
Longitude (°E)	114.17	114.08	114.17	114.17
Elevation (m)	18	43	32	65
MBE (m/s)	0.58	1.67	3.89	2.68
RMSE (m/s)	1.79	2.75	5.49	3.95

4.2.2. CityFFD

A wind tunnel experiment for the Japanese city of Niigata conducted by Tominaga et al. [24] was used for CityFFD validation, as described in this section. The tallest structure was 60 m high in full scale, and the radius of the urban building geometries was 500 m, as shown in Fig. 4.4(a). The experiment measured the time-averaged wind speed at 80 sampling points, as shown in Fig. 4.4(b) [24]. All the sampling points were located at the height of 8 mm above the ground in the downscaled model, which corresponded to 2 m in full scale. Three sets of grid were tested with the total the cell number of 3.9 million, 19.4 million, and 40.4 million, and the grid with 19.4 million cells was sufficient for this case. Structured grids were used in this model, as shown in Fig. 4.4(c), and uniform grids were distributed near the zone in which the buildings were situated, with dimensions of 1 meter horizontally and 0.5 meter vertically. The total grid number was 19.4 million. The ground surface and building walls were set as non-slip conditions with smooth surfaces. Currently, CityFFD does not include wall functions, as our previous validation studies at the urban scale demonstrated acceptable accuracy for the outer layers and regions away from the surface without these functions [107,125]. Additionally,

for large urban scale simulations, the Y+ values are typically high, so a wall function may be beneficial in enhancing accuracy. This is a limitation of the current version of CityFFD, and we intend to implement wall functions to improve the simulation near surfaces. The downstream boundary was set as the pressure outlet, and the top and lateral boundaries were set to be symmetric. The inflow boundary condition was set as the measured results from the original study [24].

Fig. 4.4 (a) Geometrical models of the urban area used for validation, (b) positions of the sampling points in the wind tunnel experiment [24], and (c) mesh design for the simulation.

Fig. 4.5 compares the measured results, the simulated results in this study, and the CFD results reported by Tominaga et al. [24]. The wind speed ratio was defined as the ratio between the wind speed at each measuring location and that at the inflow border at the same height. For CFD simulations , mean relative errors are more widely used to evaluate the simulation performance [7,16,35]. Thus, using this parameter made it easier to compare our simulation performance with previous work. The mean relative error of our calculation was -30.25% for the wind speed ratio, and the mean relative error for the same case in the literature [24] was -29.28%. The relative error of the CityFFD simulation was within acceptable limits based on previous studies on urban wind fields [16]. Therefore, our CityFFD results showed similar accuracy to that in the literature on an urban layout.

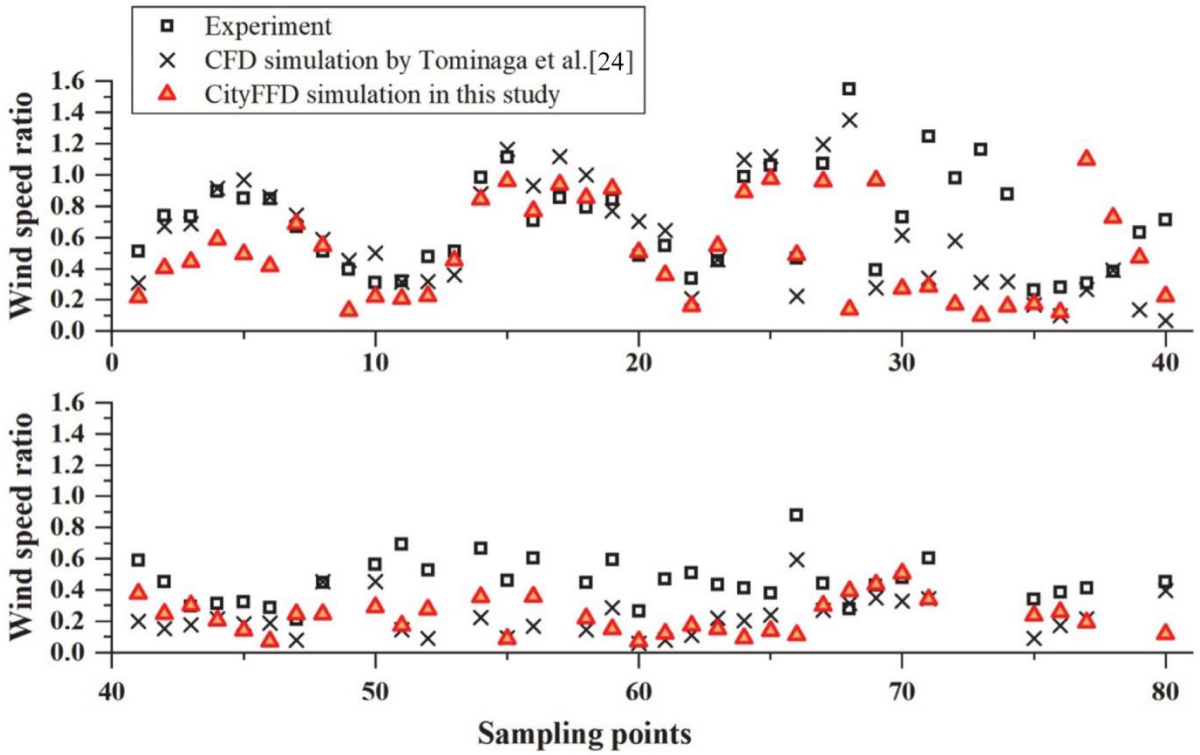

Fig. 4.5 Comparisons of the measured wind speed ratio and calculated results

4.3. Case setup

The Kowloon district in Hong Kong was selected for evaluation of the performance and applicability of the time-varying power-law wind profiles obtained from mesoscale models. Kowloon, one of the first few areas to be developed in Hong Kong, has an extremely complex and dense urban morphology [126]. During the time period between 16:00 and 24:00 on 21 October 2016, the wind direction was stable at the southwest. Therefore, CFD inflow boundary can be set at the same location, and this time period was chosen for the CityFFD simulation.

4.3.1. Computational domain and mesh design

According to the meteorological data, the wind direction for the Kowloon district during the calculation period was southwest (i.e., the wind-from direction was between 180° and 270°). Therefore, a domain of 3.5 km by 2.4 km in the Kowloon Peninsula, as shown in Fig. 4.6(a),

was chosen for this study. The weather station SF was in the windward direction, so the boundary of the study domain was set near SF. Fig. 4.6(b) shows the three-dimensional geometric model of the selected area. Note that all buildings and terrain were explicitly resolved in this model; other obstacles, such as greenery and roads, were neglected. The geometric data was transformed from public sources such as OpenStreetMap, NASA, and USGS [127]. An et al. [128] recommended the inclusion of buffer areas for geometric models with topography. These areas should ideally be sloped at an inclination angle (θ) of less than 30° in order to minimize the impact of an elevated terrain border on the simulation results. Therefore, buffer areas indicated by the dark grey shading in Fig. 4.6(b) and (c) with θ of 20° were included in the geometric model. This is also the reason that SF was set near the geometric boundary rather than at the boundary. Two meteorological stations, KP and HKO, were located in the study area, and their measured data were used as a benchmark.

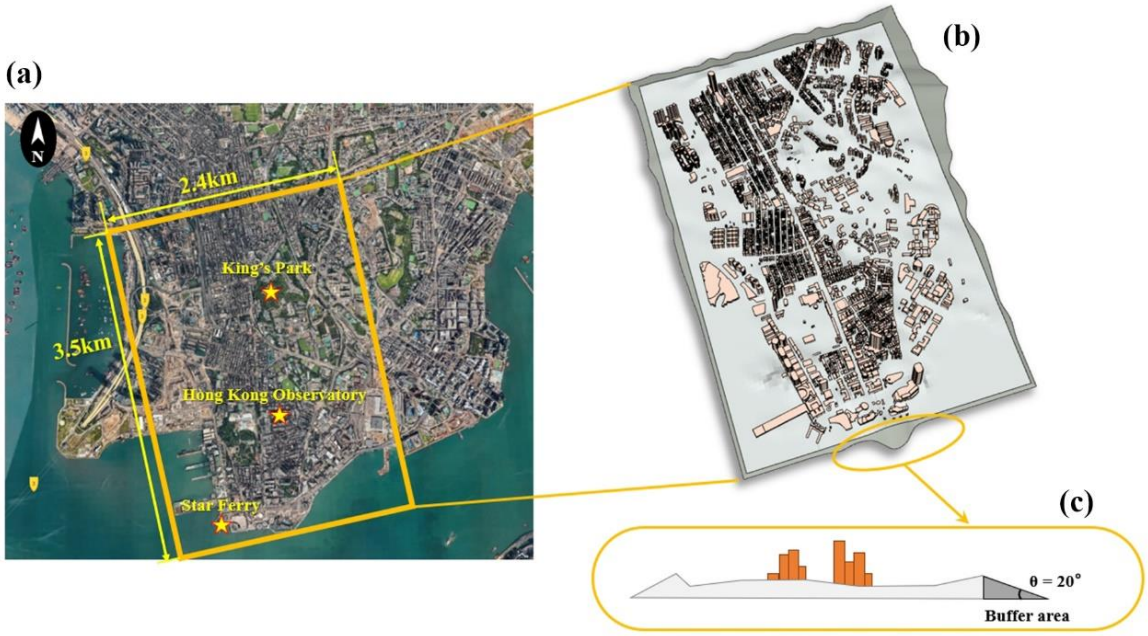

Fig. 4.6 Study area for CityFFD simulation: (a) plane view of the target area (where weather stations are marked with stars), (b) geometries of buildings and terrain, (c) setting of buffer areas.

This study followed the recommendations of AIJ [59], COST guidelines [97], and An et al. [128] to determine the computational domain size for CityFFD simulation. The vertical length of the computational domain should be no less than $5H_{max}$, where H_{max} is the height of the tallest building within the target area. The lateral boundaries of $5H_{max}$ are recommended. Meanwhile, the blockage ratio should be less than 3%, and artificial acceleration should not be observed near the borders. In this case, the tallest structure located in the study area was 284

meters high (H_{max}), so the whole model was 5.30 km long, 5.08 km wide, and 1.45 km high (see Fig. 4.7(a)). Note that the lateral boundaries in the downstream area were $4H_{max}$, due to the limitations of computing capacity. The blockage ratio was 1%, and no artificial acceleration was observed.

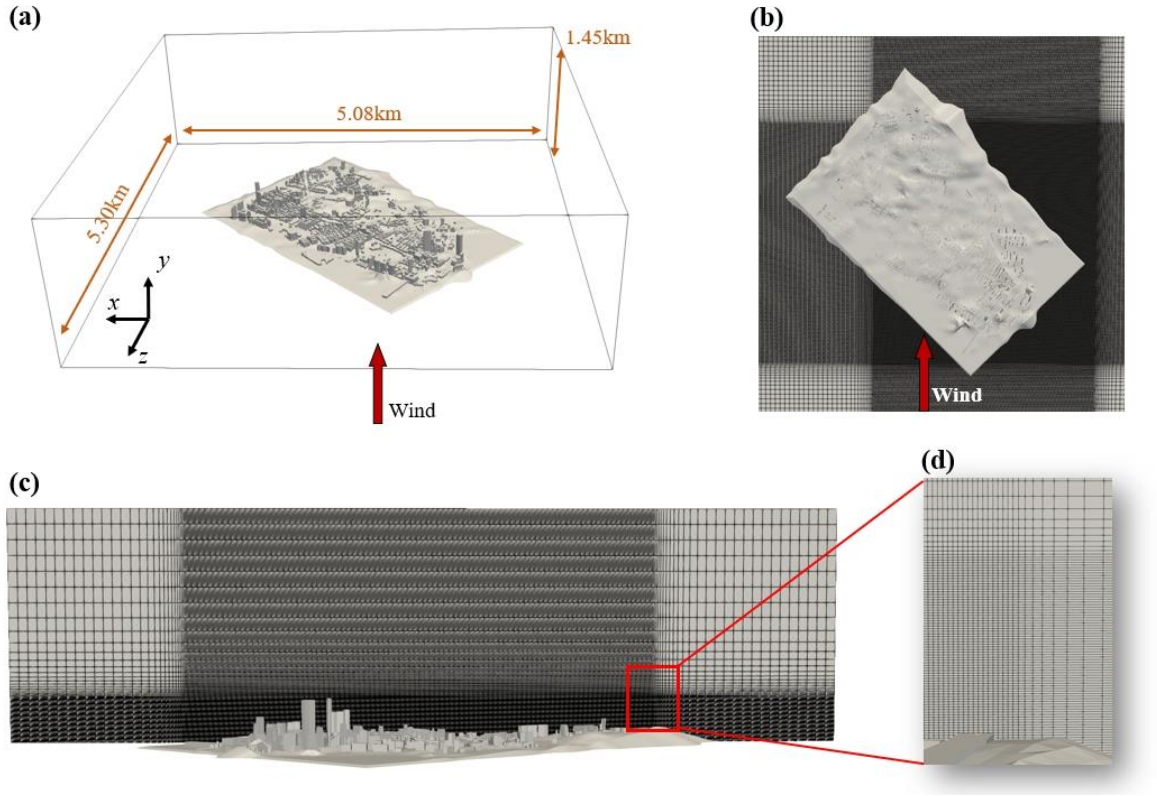

Fig. 4.7 Setup of CityFFD simulations: (a) computational domain, (b) mesh design in the horizontal direction and (c) vertical direction, (d) details of the grid transition section.

The mesh generation techniques of the CityFFD simulation were based on the staggered Cartesian meshes, and more information about this technique can be found in our previous work [110,129]. Three sets of grid were tested with the grid number of 35.3 million, 105.6 million, and 229.4 million, and the 105.6 million grids were chosen after the grid independence test. The details of the mesh design are shown in Fig. 4.7(b-d). The grid size near buildings and terrain was 4 meters horizontally and 2 meters vertically, which satisfied the grid size requirement [110]. The grid size gradually increased to 60 meters in all directions at a stretching ratio of 1.2. The total grid number was 105.6 million. The numerical simulations were conducted by a PC with GPU NVIDIA GeForce RTX 3080, and the computing time for each case was 10 hours.

4.3.2. Inflow boundary conditions

The wind during the simulated duration was sweeping from the southeast across the calm sea surface. Thus, the transition area upstream of the study domain was assumed to have no effect on the approach wind. Based on the assumptions, this study used the wind profile at SF as the inflow boundary condition. The inflow boundary was set as the velocity inlet, and this study approximated the wind profile at the inlet as a power law following Eq. (4.9). The obtained U_{ref}, α, and z_{ref} for the inflow wind profile in the two methods are described below.

4.3.2.1. Semi-empirical method

In the semi-empirical method, the measured wind speed and direction at SF were used for the inflow boundary conditions. The power-law coefficient α in this method was set as 0.18 [128], and z_{ref} for SF was 18 m above sea level. The measured wind speeds at SF (Fig. 4.3(a)) were used as U_{ref}.

4.3.2.2. From mesoscale modelling: WRF

Similarly, the WRF-calculated wind profile at SF was used for the inflow boundary conditions in this method. The WRF case setup was the same as that for the WRF validation case in Section 4.2.1. The innermost domain of WRF contained the built-up areas in Kowloon and covered the CityFFD simulated area. The calculated SF wind profile was obtained from data at the grid point closest to SF. Note that the WRF model has a horizontal grid resolution of 200 m in that region; thus, SF and the windward boundary of the study domain were in the same element. The power-law coefficient α and U_{ref} were obtained for 22.29 °N and 114.17 °E, and z_{ref} for SF was 18 m above sea level. Unsteady simulation was conducted for WRF simulation, and the results were extracted with an interval of 20 minutes. The calculated wind speeds at SF can be found in Fig. 4.3(a).

Fig. 4.8 compares the time-varying power-law coefficient α from WRF simulation and the empirical value within the calculation period. The calculated power-law values of wind profiles from WRF varied between 0.133 and 0.359, and the empirically determined power-law value was within this range. In addition, the calculated power-law value was lower than the empirical value (0.18) in the afternoon (before sunset at 18:00), while it rose over 0.18 in the evening (after sunset). The calculated power-law coefficient then dropped slightly during the night. Thus, the local atmospheric circulation and diurnal variations can lead to changes in the power-law coefficients.

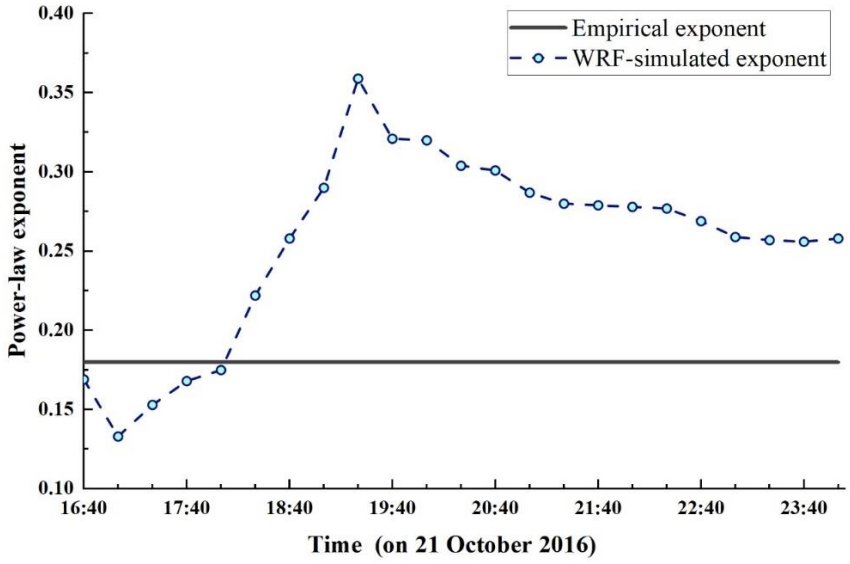

Fig. 4.8 Variation of the extracted power-law coefficient α during the simulation period on 21 October 2016.

4.4. Results

To evaluate the combined method, we compared the simulated wind speeds from WRF-CityFFD and semi-empirical-CityFFD with the measured wind speeds at KP and HKO as the benchmark. We further compared the two methods in calculating flow distributions at the height of the two stations. Finally, we assessed the WRF prediction capacity at different weather stations to explore the applicability of the combined method.

4.4.1. Comparison between WRF-CityFFD and semi-empirical-CityFFD

The comparisons of WRF-CityFFD and semi-empirical-CityFFD with the measured data at KP and HKO are shown in Fig. 4.9(a) and (b), respectively. The results of WRF-CityFFD were mostly comparable with the measured values, while those of the semi-empirical-CityFFD significantly deviated from the measured data at some time points. For example, at 19:40 for KP, the wind speed obtained by WRF-CityFFD was 4.12 m/s, comparable with the monitored data (3.54 m/s). In contrast, the result from semi-empirical-CityFFD was 6.97 m/s, and it was 96.9% higher than the benchmark. For HKO, the measured wind speed at 17:00 was 5.51 m/s. Compared with the measured result, WRF-CityFFD predicted a similar speed of 5.35 m/s, while that from semi-empirical-CityFFD (7.96 m/s) was significantly higher. Therefore, WRF-CityFFD performed better than semi-empirical-CityFFD in calculating wind velocities in urban microclimates. Note that the inflow boundary condition of City-FFD simulations were determined by both α and wind speed at SF station (U_{ref}) as in Eq. (4.9). Therefore, the simulated wind speed variation trend between the two methods was not necessarily the same as that of α in Fig. 4.8.

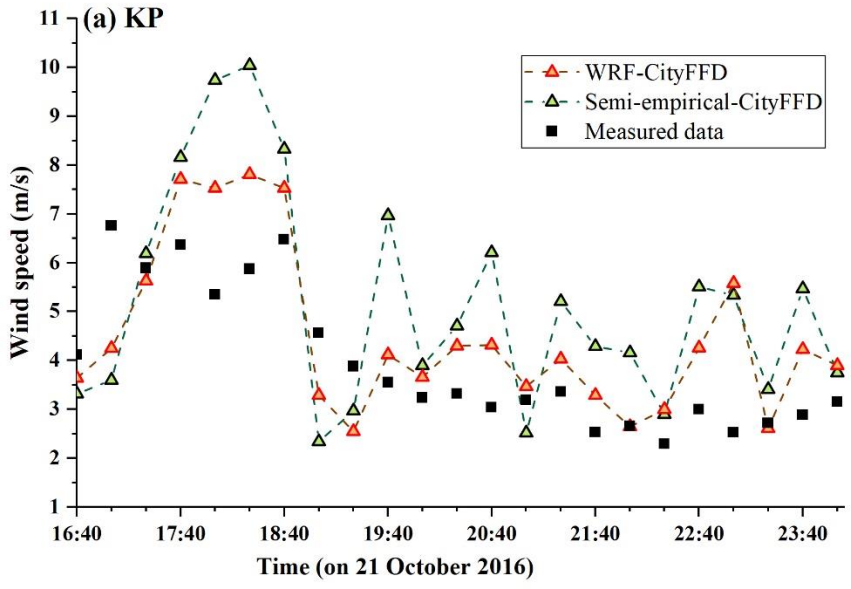

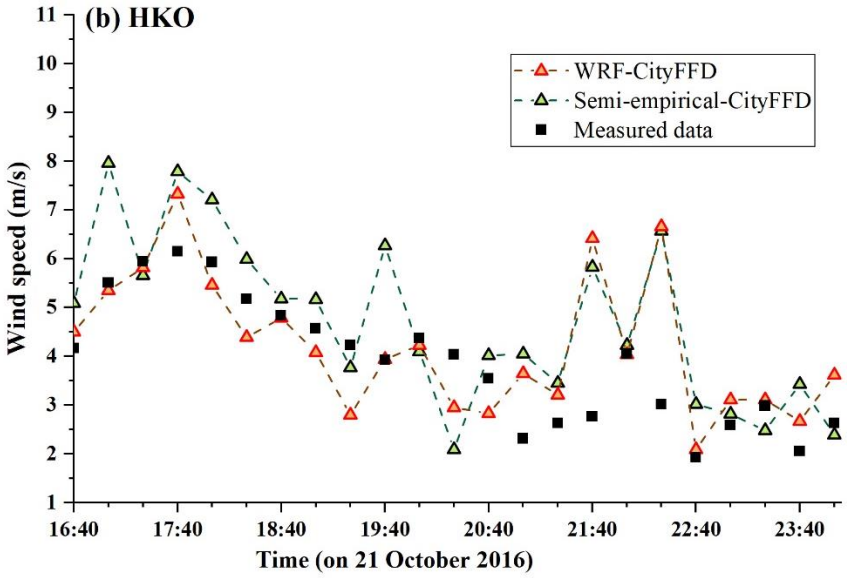

Fig. 4.9 Comparisons of the semi-empirical-CityFFD results and WRF-CityFFD results with the wind speed measured at (a) KP and (b) HKO on 21 October 2016.

For a quantitative assessment of the performance of the two methods, Table 4.3 shows the relative deviation, MBE, and RMSE for the two methods at KP and HKO. The relative deviation of WRF-CityFFD was 18.1% at KP and 14.7% at HKO, and the relative deviations of semi-empirical-CityFFD were 37.2% and 26.1% at KP and HKO, respectively. The MBE and RMSE of the WRF-CityFFD results were also lower than those of the semi-empirical-CityFFD results at both stations. In addition, previous studies have used semi-empirical inflow boundary conditions for CFD modelling to calculate airflows for actual urban layouts. The relative error of their numerical simulations ranged from 20.0% to 40.8% when compared with the measured wind speed in field tests [16,47,61], which was higher than the relative deviation for the combined method in this study. For instance, Liu et al. [16] established a detailed full-scale model from a university campus to its nearest weather station, and their CFD model overestimated the wind velocity by 20%. Therefore, WRF-CityFFD has greater potential than the traditional CFD methods for accurately predicting urban wind distributions.

Table 4.3 MBE and RMSE of wind speed at KP and HKO.

Station name	KP		HKO	
Method	WRF-CityFFD	Semi-empirical-CityFFD	WRF-CityFFD	Semi-empirical-CityFFD
Relative deviation	18.1%	37.2%	14.7%	26.1%
MBE (m/s)	0.55	1.23	0.34	0.84
RMSE (m/s)	1.31	2.24	1.26	1.50

Next, we compared the wind fields calculated by WRF-CityFFD and semi-empirical-CityFFD at the height of the measuring points of HKO and KP. Fig. 4.10(a) and (b) compare the wind speed distribution at HKO calculated by the two methods at 17:00. In general, the obtained wind speed distributions were similar, while significant discrepancy was observed in the marked area. At this time point, the WRF-simulated α (0.133) at SF was lower than the empirical coefficient (0.18); thus, semi-empirical-CityFFD underpredicted the approach wind speed by 0.7 m/s compared with WRF-CityFFD. In contrast, in the marked area in Fig. 4.10(c), semi-empirical-CityFFD underestimated the wind speed by up to 4.6 m/s. Similarly, Fig. 4.10(d-f) shows the results at 19:20, and the WRF-simulated α (0.359) was larger than the empirical coefficient at that time. Compared with WRF-CityFFD, semi-empirical-CityFFD overestimated the approach wind speed by 0.2 m/s and the wind speed in the marked area by up to 4.2 m/s. Note that the average height of the building complex on the left side of the marked area was 50 meters, and that of the building structure on the right side (represented by dashed polygons) was 23 meters. Therefore, the marked area was in the wake region of the taller building complex in this study. The results show that the difference in the inflow boundary was exacerbated in the wake region. A similar phenomenon was observed at the height of KP. Moreover, the selected plane was above the rooftop of the lower construction in the marked area. Previous experimental studies found that ambient wind over rooftop level was correlated with pollutant dispersion within the street canyon [130–133]. Considering that urban areas have large numbers of high-rise buildings, especially in high-density cities, inflow boundary conditions could have a significant impact on the pollutant dispersion in street canyons within the wake regions. Therefore, the power-law exponent for wind profiles should be carefully defined when conducting CFD simulations for complex urban layouts.

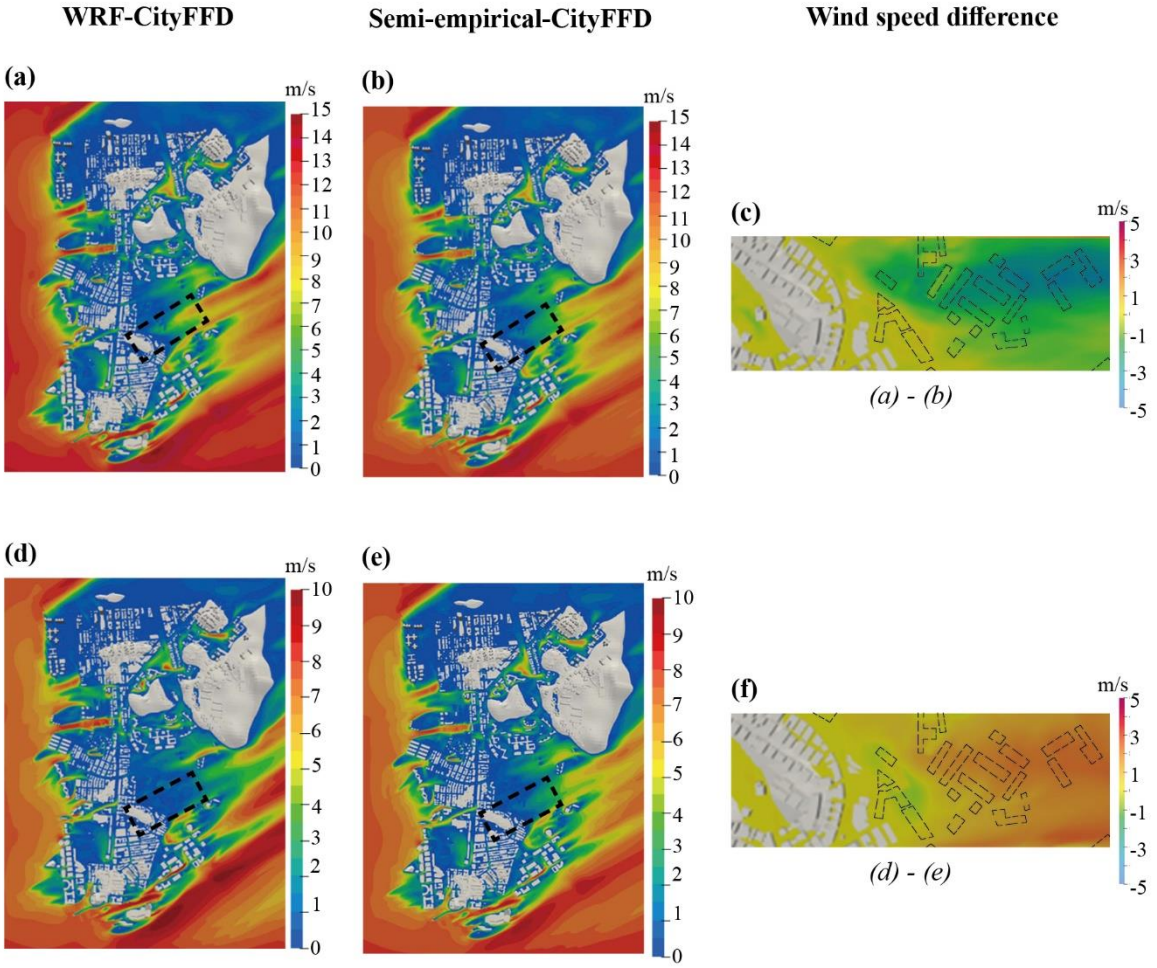

Fig. 4.10 Comparisons of the performance of the two methods at the height of HKO: When WRF-simulated α was lower than 0.18, and wind flow field was calculated by (a) WRF-CityFFD and (b) semi-empirical-CityFFD; and (c) the difference between the two. When WRF-simulated α was larger than 0.18, and wind flow field was calculated by (d) WRF-CityFFD and (e) semi-empirical-CityFFD; and (f) the difference between the two.

4.4.2. Applicability of the combined method

To assess the applicability of the combined method, we evaluated the WRF prediction capacity at different weather stations. Fig. 4.11 compares the WRF-simulated wind speed (horizontal axis) with the measured data (vertical axis) at each weather station. The solid line represents the 1:1 line, while the dashed line is the relative error of ±30%. If a point is above the 1:1 line, the WRF overpredicted the wind speed compared to the measured data, whereas a point below the 1:1 line indicates an underprediction. The results show that at the coastal weather stations (SF and SOD), most of the points were within the range of ±30% relative error. However, at

the downtown weather stations (KP and HKO), wind speeds were overestimated by more than 30% most of the time, especially when the measured wind speed was greater than 2 m/s. Therefore, the WRF performed better in the coastal area than in the downtown area. The specific value of building height in industrial and commercial areas was 10 m in SL-UCM [119] for WRF, while the tallest building of the target complex urban area in this study was 284 m. Thus, the default urban canopy parameterization schemes of SL-UCM could not represent urban morphology for high-density cities. Therefore, coastal areas were more suitable for selection as inflow boundary conditions for WRF-CityFFD. Similarly, for the inland cities, it is recommended that the borders of the built-up areas (for example, sub-urban or open and flat areas) be used as the inflow boundary conditions for WRF-CityFFD.

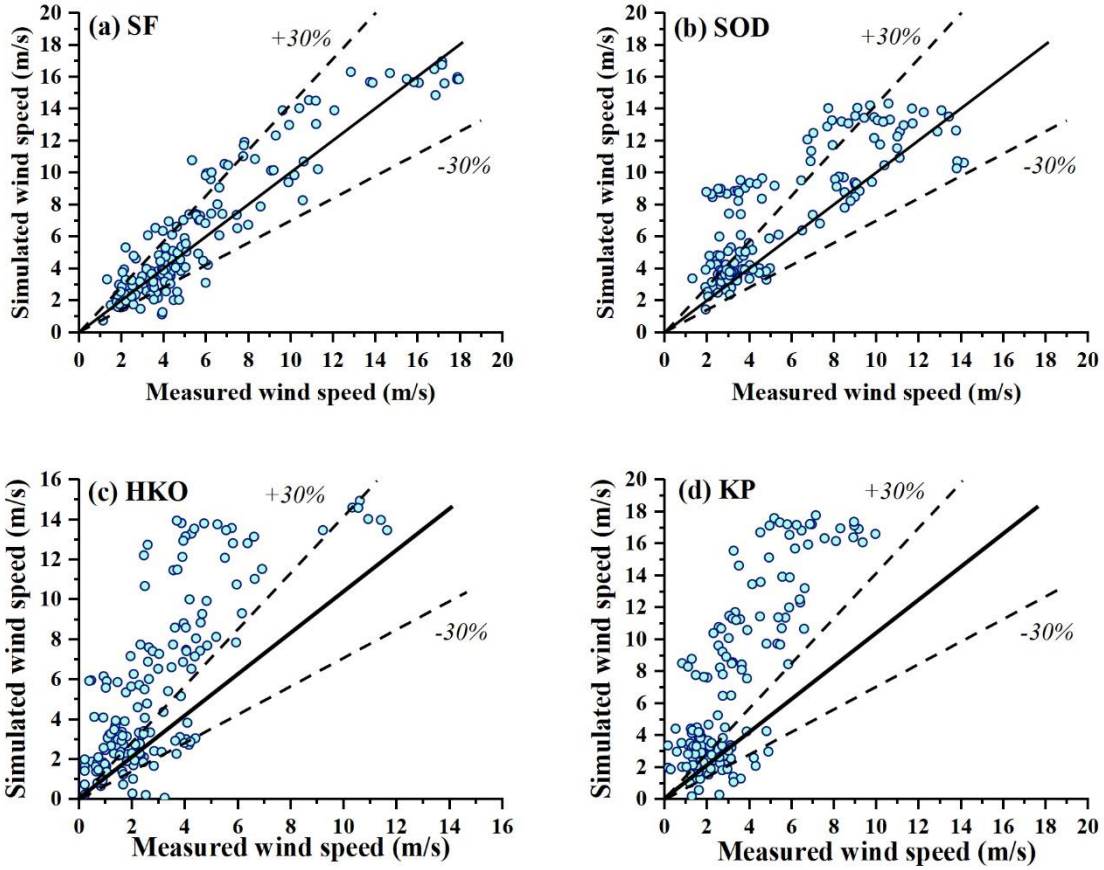

Fig. 4.11 Comparison of the WRF-simulated results and measured results at (a) SF, (b) SOD, (c) HKO and (d) KP.

We then compared the WRF-simulated wind speed under onshore and offshore wind conditions. The wind blew from the urban area to the SOD (offshore wind) during 26% of the simulation time; during the other 74% of the time, the wind swept across the sea (onshore wind). For SF, onshore wind occurred during 95% of the simulation time. Therefore, we only compared the

simulated wind speed and measured wind speed at SOD under onshore and offshore wind conditions. As shown in Fig. 4.12(a), most of the time, WRF overpredicted the wind speed by over 30% under offshore wind conditions. Fig. 4.12(b) shows that WRF provided reasonably accurate predictions under onshore wind conditions for SOD. Thus, for coastal areas, onshore wind conditions are more suitable for use as inflow boundary conditions for WRF-CityFFD. For inland cities, the recommended scenario is an open area with few structures in the upstream direction.

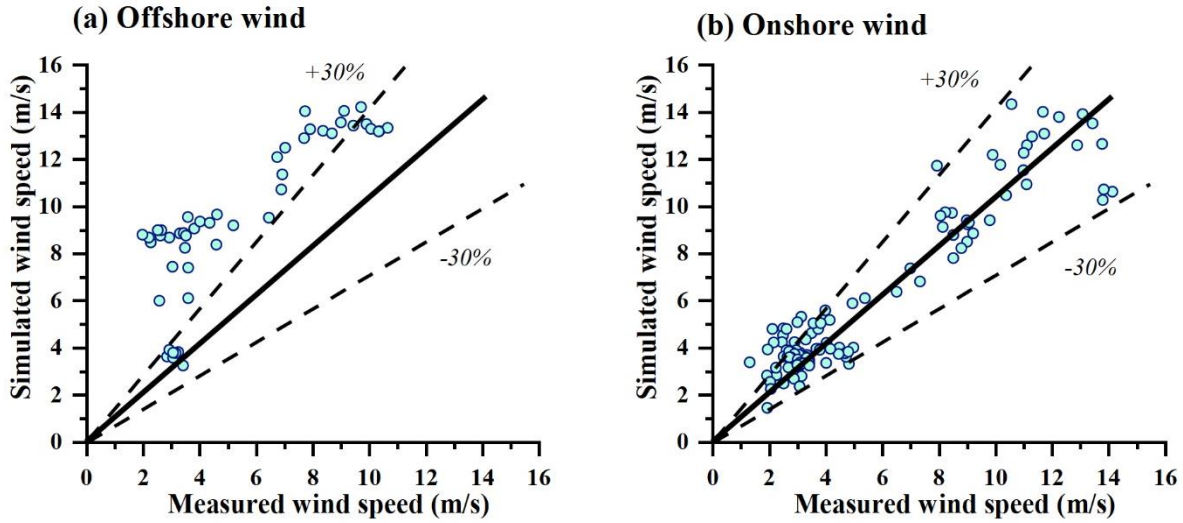

Fig. 4.12 Comparison of the WRF-simulated results and measured results under (a) onshore wind conditions and (b) offshore wind conditions at SOD.

4.5. Discussion

Note that the lateral length of the inflow was 5.08 km, which was larger than the horizontal grid resolution of the WRF (200 meters). Taking 24:00 on 21 October 2016 as an example, the lateral wind speed ranged from 5.76 m/s to 6.98 m/s. However, only the wind conditions at the SF station were used in this study, and the lateral wind speed difference was not considered. The usage of WRF results along horizontal directions needs to be further evaluated for our future work. In this study, roads, and greenery were not taken into account using ground roughness. It was because our previous work has shown that the CityFFD with the setting of non-slip boundary conditions can provide reasonable results in both wind-tunnel validation

cases and full-scale urban simulations [107,110]. However, future studies are needed to consider this aspect.

The combined WRF-CityFFD method can be used to calculate wind profiles flexibly and accurately, especially for cities with only a limited number of meteorological stations. The proposed combined method can help improve the model's ability to reproduce urban wind patterns. Thus, the method can be further used to provide the high-resolution wind microclimate, modelling down to the scale of the pedestrian level. Additionally, urban airflow plays an important role in removing and diluting pollutants. The mass exchange occurred both in the open space (directly blown away) and the layer above the urban canopy (pollutant removal due to turbulent fluctuations) in an urban atmosphere. Thus, accurate calculation of the urban wind distributions will be crucial for studies on the pollutant's transportation in urban areas, including dispersion in far fields and street canyons. Accordingly, the pollutants exposure for urban residents can be further investigated.

4.6. Summary

This investigation aimed to evaluate the potential of a combined WRF and CityFFD method for calculating urban wind distributions. This study used WRF-CityFFD to calculate the wind distribution in the Kowloon district of Hong Kong within an area of 3.5 km × 2.4 km. Semi-empirical-CityFFD was also used for comparison. In addition, the applicability of the combined method was evaluated. Within the scope of this study, the following conclusions can be drawn:

- The WRF-CityFFD performed better than the semi-empirical-CityFFD in calculating wind velocities in urban microclimates.
- The power-law exponent for wind profiles should be carefully defined when conducting CFD simulations for complex urban layouts.
- Coastal areas with onshore wind conditions were recommended for selection as inflow boundary conditions for WRF-CityFFD.

CHAPTER 5. Develop an analytical method to predict urban wind profile in built-up areas using a combined method of WRF and a porosity model

As described in Chapter 4, mesoscale models such as Weather Research and Forecasting (WRF) simulations are not sufficiently precise to predict wind profiles in built-up areas, and existing improvement methods remain computationally expensive and time-consuming. To efficiently and accurately estimate wind profiles in built-up areas, this study proposed a method that combines WRF with a porosity model. WRF provides the wind profile at the urban edge, and the porosity model calculates the airflow pressure drop across the selected urban area using a parametrized urban layout. The urban wind profile is then analytically determined with the momentum integral method. The performance of the proposed method was first evaluated in three generic urban layouts, with validated computational fluid dynamics (CFD) simulations used as benchmarks. The proposed method was then applied in a real urban layout to demonstrate its performance, and the Kowloon district of Hong Kong, with an area of $2{,}350\,m \times 643\,m$, was selected as the target area. The wind profile measured with a radiosonde in the same region was used as a benchmark, and the WRF-calculated wind profile in the built-up area was also evaluated for comparison.

5.1. Proposed method

A method that combines WRF with a porosity model is proposed for efficiently estimating wind profiles in built-up areas. As WRF performs well in predicting wind profiles at the urban edge [19,23], it was used to provide the inflow wind profiles for the proposed method. To estimate wind profiles in built-up areas, the momentum integral method can be employed to derive explicit expressions for urban wind profiles. This method establishes a relationship between the momentum changes of wind profiles before and after passing through urban areas and the pressure drop of airflow. The effectiveness of this analytical modelling approach has been proven in the literature [77–79]. For estimating the pressure drop required by the momentum integral method, the porosity model is widely used, as it considers the effects of

different building arrangements in complex urban areas by adapting the urban morphology parameters [134–136]. Fig. 5.1 displays the flow chart of the proposed method. This section provides detailed explanations of the inflow wind profiles obtained from WRF, as well as the porosity model and momentum integral method used in the proposed method. Additionally, the definitions and settings of the urban morphology parameters are described in this section.

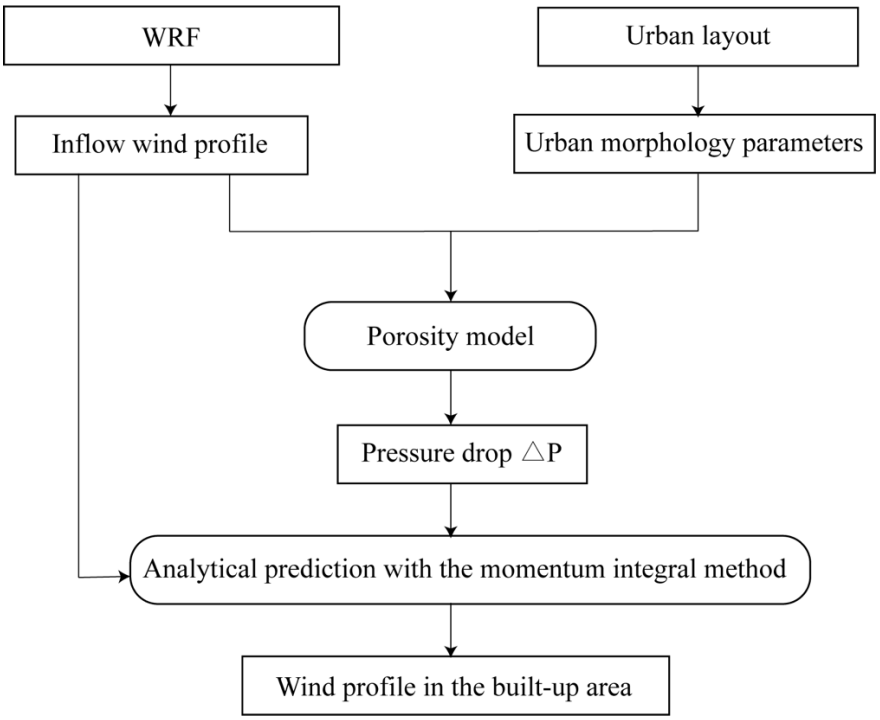

Fig. 5.1 Flow chart of the proposed method.

5.1.1. Analytical prediction of urban wind profiles

Considering only a neutrally stratified ABL, the wind speed are assumed to be accurately approximated with a logarithmic profile, as shown in Eq. (5.1) [137].

$$u(z) = \frac{u^*}{\kappa} \ln\left(\frac{z}{z_0}\right) \tag{5.1}$$

where κ is the von Karman constant (~0.42) [137], u^* is the friction velocity (m/s), and z_0 is the aerodynamic roughness length (m). To obtain the mathematical expression for the

logarithmic wind profile after passing through the selected urban area, the values of u^* and z_0 are required.

For the estimation of the wind profiles in the built-up areas, the momentum integral method was used to establish the relationship between the velocity profile within the UBL and the pressure drop of airflow [138,139]. In this method, airflow through urban areas was described as flow over fully rough surfaces [140], and the urban boundary layer (UBL) was treated as a turbulent boundary layer [140]. Based on these assumptions, the momentum integral method was used to derive mathematical expressions for wind profiles, and the governing equation is given as follows [85]:

$$\frac{d\delta}{dx} = \frac{\tau_w}{\rho u_e^2} \tag{5.2}$$

$$\delta = \int_0^{H_{UBL}} \frac{u(z)}{u_e}\left(1 - \frac{u(z)}{u_e}\right) dz \tag{5.3}$$

where the positive x-direction represents the inflow direction. Here τ_w is the shear stress caused by the roughness elements (N/m^2), ρ is the air density (kg/m^3), $u(z)$ is the wind profile, and δ is the momentum thickness (m), which can be calculated by Eq. (5.3). Note that Eq. (5.3) was derived from the Navier-Stokes equations, and therefore both mass and momentum conservation were satisfied. H_{UBL} is the depth of the UBL ($6H$ in this study). The UBL depth typically ranges from $2H$ to $6H$ [137,141,142], where H is the average building height in the area upwind of the selected built-up region (i.e., the region through which the airflow passes). Given the complexity of real urban layouts, a value of $6H$ was chosen for the UBL depth in this study. Meanwhile, u_e is the free-stream velocity, which can be obtained from the inflow wind profile at the height of H_{UBL} (see Section 5.1.2).

The shear stress (τ_w) represents the drag force exerted by the bottom roughness elements on the airflow. In this study, τ_w is used to quantify the aerodynamic resistance of the urban areas characterized by complex roughness elements. Based on the Monin–Obukhov similarity theory (MOST) [137], atmospheric conditions are assumed to be steady-state and horizontally homogeneous, with a constant turbulent momentum flux ($\overline{u'w'}$) within the urban canopy layer. Under these assumptions, τ_w can be estimated from the pressure drop across the urban canopy, as shown in the following equation [142].

$$\tau_w = -\rho\overline{u'w'} = \frac{-\Delta P \cdot H \cdot \rho}{L} \tag{5.4}$$

The change in momentum thickness ($\Delta\delta$) as wind passes through a selected urban area with a length of L can then be obtained by combining Eqs. (5.2) and (5.4):

$$\Delta\delta = \frac{-\Delta P \cdot H}{u_e^2} \tag{5.5}$$

When Eqs. (5.1), (5.3) and (5.5) are combined, the relationship between the pressure drop of airflow across the selected urban area and the wind profile in the built-up area is obtained:

$$\int_{z_0}^{H_{UBL}} \left(\frac{u^*}{\kappa u_e} ln\frac{z}{z_0}\right)\left(1 - \frac{u^*}{\kappa u_e} ln\frac{z}{z_0}\right) dz = \delta_{inflow} - \frac{\Delta P \cdot H}{u_e^2} \tag{5.6}$$

where δ_{inflow} represents the momentum thickness of the inflow wind profile. To estimate the values of u^* and z_0 for urban wind profiles, Eqs. (5.1) and (5.6) were solved simultaneously. Parameters such as δ_{inflow}, u_e, and its corresponding height were extracted from the inflow wind profile obtained from WRF, and ΔP was calculated using the porosity model. Details of these derivations are provided in Sections 5.1.2 and 5.1.3.

5.1.2. Inflow wind profile from WRF

The WRF model was used to provide accurate and realistic wind profiles at the urban edge as the inflow conditions for the proposed method. The urban edge refers to the transitional zone between the built-up area and its surrounding environment, including rural areas, open fields, and coastal regions [143]. Note that only the wind profile within the depth of the UBL located upwind of the selected built-up area could be used. As described in Section 5.1.1, a value of $6H$ was chosen for the UBL depth in this study.

To obtain the inflow wind profile for the proposed method, the values of u^* and z_0 were derived by fitting the extracted WRF data to the logarithmic wind profile, as shown in Eq. (5.1). The detailed setup of the WRF simulation can be found in Section 5.3.1.

5.1.3. Modelling the urban canopy as a porous medium

To estimate the urban wind profile, the pressure drop of airflow required by the momentum integral method was first determined. In this study, the porosity model was used to calculate the pressure drop as airflow passes through the urban canopy. Generally, the porosity models used in the literature were derived from porous media with pore-throat structures, often represented by packed particles of uniform size [136,144]. For example, Hang and Li [136] used a coefficient (i.e., the Forchheimer coefficient) from the flow equation of a pore-throat structured porous medium to estimate the pressure drop through a building array with uniform height. However, real urban layouts are characterized by complex building arrangements and diverse building shapes. Thus, modelling real urban layouts as pore-throat structured porous media is not sufficiently precise. To address this limitation, the fracture-based porosity model was adopted in this study [145].

Fractures, representing the gaps between buildings, are well-suited to capturing the complexity of real urban layouts. For instance, as illustrated in Fig. 5.2, the selected urban area had a length L and width W. The height of the porous medium H was defined as the height of the urban canopy, which was the average building height within the selected area. As shown in Fig. 5.2, the fractures in the porous medium were randomly distributed. Fig. 5.2(b) provides an example of the determination of the number of fractures (n). According to the definition of fractured porous media [145], only fractures that allow wind to flow through the entire porous medium are explicitly considered (i.e., included in n). If a fracture has multiple branches, only the branch with the lowest tortuosity is considered explicitly. Meanwhile, the branches that are not explicitly considered serve to increase the volume occupied by the solid objects; these branches are implicitly accounted for in the permeability (K) when the pressure gradient is calculated. Based on this, the value of n in Fig. 5.2 is 2, and is represented by the labels 7-4-8-9-10 and 13-11-12-16-18, respectively.

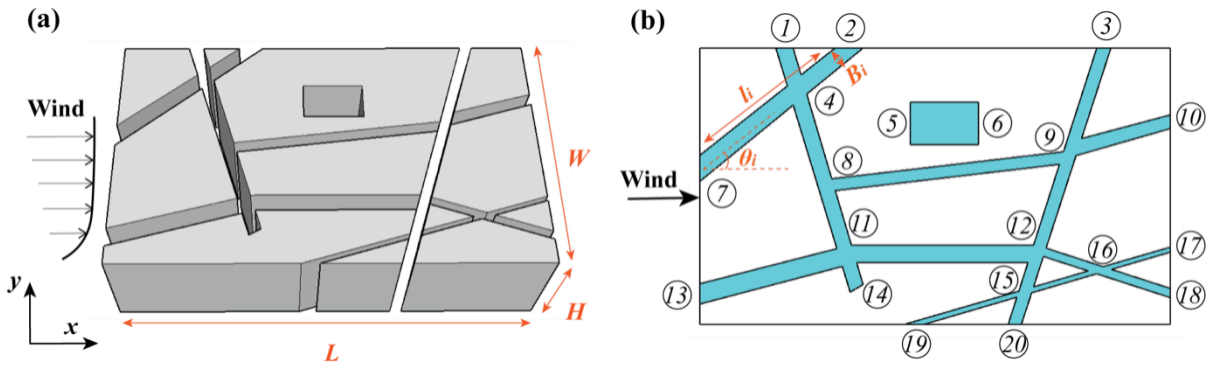

Fig. 5.2 (a) Modelling the urban canopy as a fractured porous medium, and (b) distribution of the fractures.

To calculate the pressure drop within the urban canopy, the Forchheimer equation (see Eq. (5.7)) [134,145] was used to establish the relationship between the pressure gradient and the velocity of the airflow in porous media. In this study, the airflow within the urban canopy was assumed to behave as incompressible turbulent flow passing through a fixed porous medium, following the assumptions made in previous studies [136,144].

$$-\nabla p = au + bu^2 \tag{5.7}$$

$$a = \frac{\mu}{K} \tag{5.8}$$

$$b = \beta \rho A_h^2 \tag{5.9}$$

where ∇p is the pressure gradient (Pa/m), and u is the superficial velocity (m/s), which is the macroscopic velocity of the fluid flowing through the porous medium. The specific calculation of the superficial velocity for the example shown in Fig. 5.2 can be found in Eq. (5.13). Meanwhile, a is the Darcy coefficient, and the linear term is known as the Darcy term, describing the pressure drop caused by the viscous forces [146]; μ is the viscosity of the fluid ($Pa \cdot s$); and K is the permeability of the porous media (m^2). The quadratic term was introduced by Forchheimer to account for the pressure drop caused by turbulence [134]. The β is the Forchheimer coefficient, ρ is the density of fluid (kg/m^3), and A_h is the flow sectional area (m^2). The values of β and K can be determined by Eqs. (5.17) and (5.18), respectively.

To simply Eq. (5.7), we introduce a constant $\gamma = -\frac{a^2}{4b \cdot \nabla p}$, and Eq. (5.7) can be written as:

$$\mathrm{u} = \sqrt{\frac{-\nabla p}{b}} \cdot \left[\sqrt{1+\gamma} - \sqrt{\gamma}\right] \tag{5.10}$$

According to the Taylor series:

$$\sqrt{1+\gamma} = 1 + \frac{1}{2}\gamma + \frac{\frac{1}{2}\left(\frac{1}{2}-1\right)}{2!}\gamma^2 + \cdots \tag{5.11}$$

When the higher-order terms are ignored, the leading-order approximation of Eq. (5.10) is as follows:

$$\mathrm{u} = \sqrt{\frac{-\nabla p}{b}} = \sqrt{\frac{-\nabla p}{\beta \rho A_h^2}} \tag{5.12}$$

The above equation implies that the pressure gradient caused by turbulent flow is independent of the Darcy term in Eq. (5.7). It indicates that viscous forces are neglected in this case. Hang and Li [144] conducted CFD simulations to calculate wind distributions in a building array and found that the Forchheimer term was approximately one hundred times greater than the Darcy term. Thus, the simplification of Eq. (5.7) is reasonable.

Specifically, when the urban canopy is modelled as a fractured porous medium (see the example in Fig. 5.2), the superficial velocity within the porous medium, expressed in Eq. (5.12), can also be represented by Eq. (5.13). Note that the mass exchange at the intersections of fractures [145] and the variation in building shape with height were neglected.

$$\mathrm{u} = \frac{Q}{V} = \frac{\int_0^H u_0(z)dz}{L \cdot W \cdot H} \sum\nolimits_{i=1}^{n} \cos\theta_i \cdot l_i \cdot B_i \cdot H \tag{5.13}$$

where Q is the volumetric flow rate (m^3/s); V is the volume of the porous medium (m^3); $u_0(z)$ is the inflow wind profile; θ_i is the angle between the fracture and the inflow wind direction (°); l_i and B_i are the length and width of each fracture (m), respectively; and n is the number of fractures.

When Eqs. (5.9) and (5.12) are substituted into Eq. (5.13), the following equations are obtained:

$$\frac{\int_0^H u_0(z)dz}{H} \cdot \frac{\varepsilon}{\sum_{i=1}^{n} B_i} = \sqrt{\frac{-\nabla p}{\beta \rho}} \tag{5.14}$$

$$\varepsilon = \frac{V_{flow}}{V} = \frac{\sum_{i=1}^{n} \cos\theta_i \cdot l_i \cdot B_i \cdot H}{L \cdot W \cdot H} \tag{5.15}$$

where $\frac{\int_0^H u_0(z)dz}{H}$ is the average velocity of the inflow wind profile within the urban canopy (m/s), represented hereafter by u_0; $\sum_{i=1}^{n} B_i$ is the total width of the fractures (m); and ε is the porosity, defined as the ratio of the fluid volume (V_{flow}) to the total volume of the porous medium (V).

Finally, the pressure drop across the selected urban layout can be obtained as follows:

$$\Delta P = -\nabla p \cdot L = \frac{\beta \rho L \varepsilon^2}{n^2 \bar{B}^2} \cdot u_0^2 \tag{5.16}$$

where ΔP is the pressure drop across the selected urban layout (Pa); β is the Forchheimer coefficient; and n and $\bar{B}$ are the number and average width of the fractures, respectively.

The Forchheimer coefficient (β) depends on the characteristics of the porous medium (i.e., the layout of the selected built-up area), and it can be calculated by Eq. (5.17) [147]:

$$\beta = \frac{c\tau}{\rho \cdot \varepsilon^c \cdot K^c} \tag{5.17}$$

$$K = \frac{\varepsilon^3 d_p^2}{150(1-\varepsilon^2)} \tag{5.18}$$

$$d_p = 6\frac{V_{buildings}}{S_{buildings}} \tag{5.19}$$

where τ is the average tortuosity of the fractures in the porous medium. Here tortuosity refers to the ratio of the average length of the fractures to the length of the porous medium (L) [148]. Meanwhile, K is the permeability (m^2), which can be estimated by the Ergun equation [149], as shown in Eq. (5.18); d_p is the equivalent spherical diameter of buildings in the porous

medium (m); and $V_{buildings}$ and $S_{buildings}$ are the average volume (m^3) and surface area (m^2) of the buildings in the porous medium, respectively.

In Eq. (5.17), c is an empirical parameter, typically ranging from 0 to 2, and is commonly determined through experiments. The value of c depends on the properties of the solid objects in the porous medium, decreasing as the particle size of the solid objects increases [147]. However, when the urban canopy is modelled as a porous medium, the solid objects, which are buildings, are significantly larger than those in conventional porous media. Therefore, it is challenging to find an appropriate reference for setting the c value. In this study, we assumed c to be 0.11. In the building array cases (see Section 5.2), the resulting Forchheimer coefficient β ranged from 0.5 to 1, which was consistent with the values used in a previous study by Hang and Li [136]. They set β as 0.56 and 1. Thus, our assumed value for c is reasonable. When β is substituted into Eq. (5.16), the pressure drop of airflow can be determined based on the urban morphology parameters of the selected built-up area and the inflow wind profile.

5.2. Validation in generic urban layouts

The performance of the proposed method in predicting pressure drop and wind profiles was first evaluated in generic urban layouts. Three such layouts were chosen to represent building arrays with varying levels of complexity: an aligned building array with uniform height, a staggered building array with uniform height, and a staggered building array with non-uniform height. CFD simulations were chosen as benchmarks, as they are widely recognized for their accuracy and ability to provide detailed flow field data across the entire domain [23,30,61]. This section details the setup of the selected cases and compares the results estimated by the proposed method with those obtained from CFD simulations.

5.2.1. Case 1: Aligned building array with uniform height

5.2.1.1. Case setup

Case 1 was an aligned building array that had previously been studied in a wind tunnel test [96]. Therefore, in this section, the inflow wind profile for the proposed method was based on measurements from that test (see Fig. 5.3(d)). The selected array consisted of 9 × 9 buildings, each having uniform dimensions of 0.06 m × 0.06 m × 0.06 m, as shown in Fig. 5.3(a). The spacing between adjacent buildings was 0.06 m in both the x and y directions. Based on the building configuration, the selected urban canopy was modelled as a porous medium with a canopy length (L) of 1.02 m and height (H) of 0.06 m, as shown in Fig. 5.3(c). Accordingly, the mean wind velocity of the inflow wind profile within the urban canopy was 1.83 m/s.

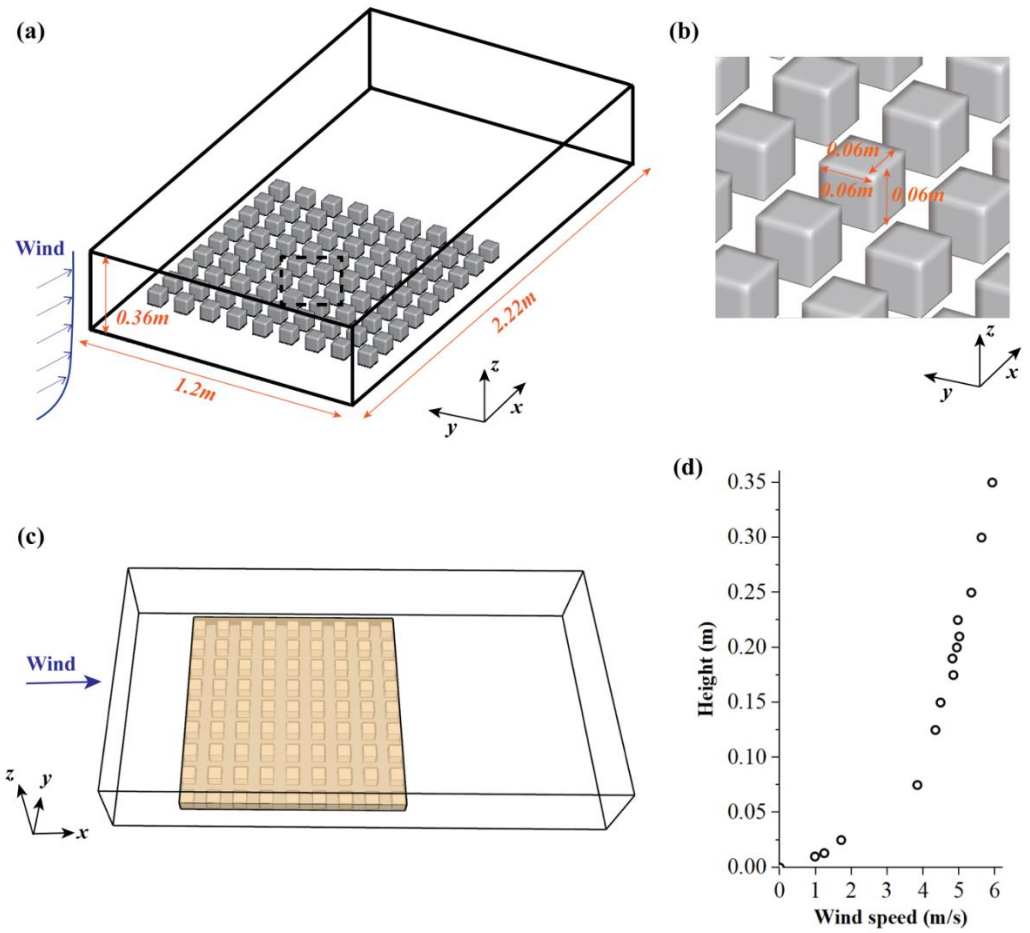

Fig. 5.3 (a) Schematic of Case 1, (b) dimensions of each building, (c) schematic of the urban canopy modelled as the porous medium, and (d) inflow wind profile obtained from wind tunnel test.

To evaluate the performance of the proposed method, CFD simulations were used as benchmarks. For the setup of the simulations, following the guidelines of COST 732 [97] and AIJ [59], the computational domain for the building array was defined as $2.22\ m\ (length) \times 1.2\ m\ (width) \times 0.36\ m\ (height)$, as shown in Fig. 5.3(a). The grid-independence test and validation of the CFD simulations can be found in our previous study [150]. The SST $k-\omega$ model was selected as the turbulence model due to its proven performance in predicting airflows in street canyons [49,150]. The boundary conditions and the solver settings, including the pressure-velocity coupling scheme and discretizing scheme for all variables, were consistent with those in our previous study [150]. All the CFD simulations in the present study were implemented in OpenFOAM 2.3.0 with an open-source CFD code, RapidCFD [87], on an NVIDIA GeForce RTX 3090Ti GPU.

5.2.1.2. Estimation and evaluation of urban wind profile for Case 1

To estimate the wind profile as airflow passes through the selected building array in Case 1, the urban morphology parameters required by the porosity model for calculating the pressure drop were first determined. As shown in Fig. 5.3(c), the total volume of the porous medium was 0.062 m^3, and the volume occupied by all buildings within the porous medium was 0.017 m^3. Thus, the porosity of the porous medium was calculated as 0.72. Next, the number (n) and tortuosity (τ) of fractures were determined. There were 8 straight fractures connecting the inlet and outlet planes, and based on the definition of fractures (see Section 5.1.3), n was 8 and τ was 1 for Case 1. The average width of the fractures was 0.06 m. The equivalent spherical diameter of the buildings (d_p) was then calculated using Eq. (5.19). When the building dimensions (0.06 m × 0.06 m × 0.06 m) were substituted into the equation, d_p was found to be 0.06 m. Finally, using the parameters obtained above, the pressure drop of airflow was calculated as 3.41 Pa for Case 1.

Subsequently, we calculated the values of u^* and z_0 for the wind profile in Case 1 using the momentum integral method. The calculations were based on the pressure drop obtained from the porosity model and the inflow wind profile measured in the wind tunnel test. As previously mentioned, the UBL depth for this case was 0.36 m, and the inflow wind profile indicated a

free-stream wind speed of 5.97 m/s at this height. When the UBL depth, the free-stream wind speed, and the pressure drop calculated by the porosity model were combined, the resulting u^* and z_0 for the urban wind profile in Case 1 were 0.51 m/s and 0.0038 m, respectively, as shown in Fig. 5.4.

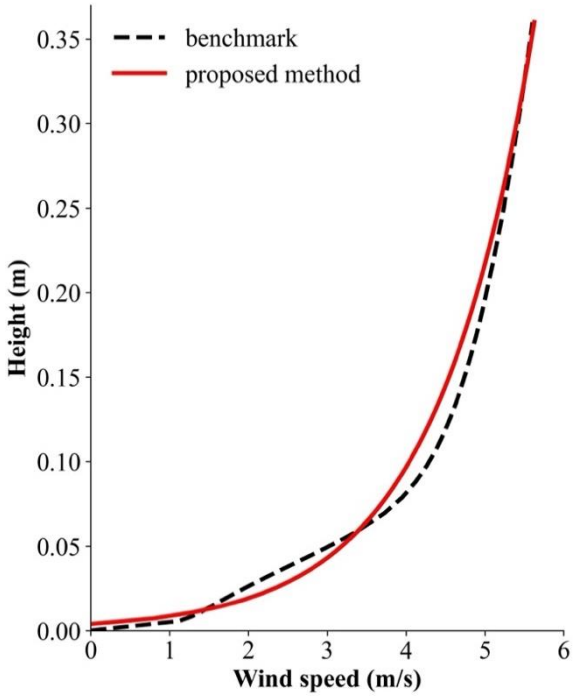

Fig. 5.4 Comparison between the benchmark and the wind profile calculated by the proposed method for Case 1.

For a comprehensive evaluation of the performance of the proposed method, both the calculated pressure drop and the urban wind profile were compared with their respective benchmarks. The benchmark pressure drop was obtained from the difference between the average pressure at the inlet and outlet planes of the porous medium, as indicated in Fig. 5.3(c). The benchmark wind profile was taken from the area downstream area of the building array, away from the wake regions. Using Eq. (5.1), the benchmark wind profile was fitted to derive $u^*_{\_CFD}$ and z_{0_CFD}, which were then compared with those from the proposed method for quantitative analysis.

For the assessment of pressure drop, the benchmark pressure drop was first extracted as 3.36 Pa from CFD simulations. The pressure drop calculated by the proposed method (3.41 Pa) was very close to the benchmark, with a difference of 1.49%. Regarding the wind profile, Fig. 5.4

compares the wind profile calculated by the proposed method and the benchmark. The $u^*_{\_CFD}$ and z_{0_CFD} obtained from the benchmark wind profile were 0.51 m/s and 0.0038 m, respectively, which closely matched the values obtained by the proposed method. Therefore, the proposed method performed well in estimating urban wind profiles for an aligned building array with uniform height.

5.2.2. Case 2: Staggered building array with uniform height

5.2.2.1. Case setup

Case 2 was a 9×9 staggered building array, where each building in the array has dimensions of $0.06\,m \times 0.06\,m \times 0.06\,m$. Along the streamwise direction, the buildings in adjacent rows were arranged in a staggered manner, as shown in Fig. 5.5(a) and (b). The method for modelling the selected urban canopy as a porous medium was the same as in Case 1 (see Fig. 5.3(c)), resulting in a canopy length of 1.02 m and a height of 0.06 m. The inflow wind profile was also the same as that in Case 1, which was obtained from the wind tunnel experiment [96]. Based on the inflow wind profile and the urban canopy height, the mean wind velocity within the urban canopy was calculated to be 1.83 m/s. For the CFD simulations used as benchmarks, the computational domain, boundary conditions, and solver settings were identical to those used in Case 1.

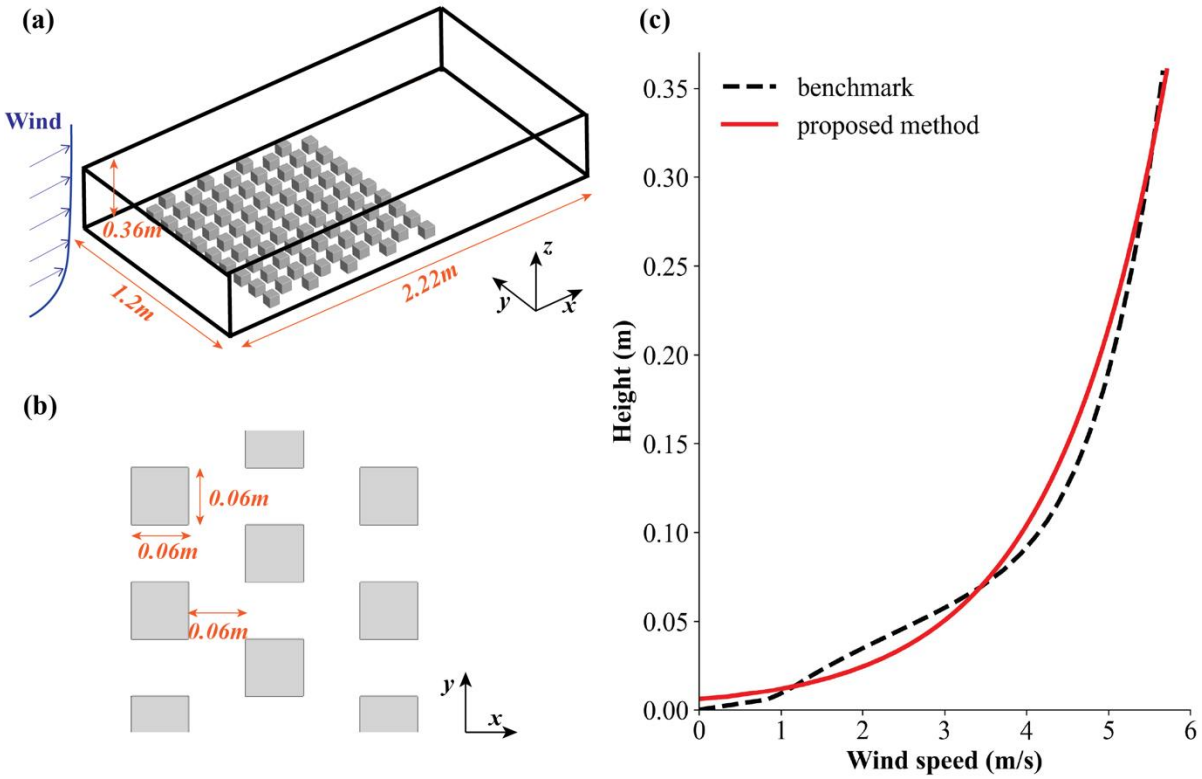

Fig. 5.5 (a) Schematic of the CFD domain; (b) top view of Case 2; and (c) comparison between the benchmark and the wind profile calculated by the proposed method for Case 2.

5.2.2.2. Estimation and evaluation of urban wind profile for Case 2

To estimate the pressure drop of airflow in Case 2, the urban morphology parameters were first analyzed based on the building configurations shown in Fig. 5.5(a) and (b). The total volume of the porous medium and the volume occupied by all the buildings were the same as those in Case 1, and were 0.062 m^3 and 0.017 m^3, respectively. Following the steps described in Section 5.2.1.2, the porosity of the staggered building array was calculated as 0.77. For the number of fractures (n), there were 8 tortuous fractures connecting the inlet and outlet planes, each with a length of 1.5 m. Consequently, n was 8, and the tortuosity was calculated as 1.47. The average width of the fractures was 0.06 m. Since the building dimensions in Case 2 were the same as those in Case 1, the equivalent spherical diameter of the buildings (d_p) was also 0.06 m. Based on the parameters above, the pressure drop of airflow was calculated as 5.01 Pa for Case 2.

For the estimation of the wind profile, in addition to the calculated pressure drop, the free-stream wind speed and its corresponding height were required. As described above, the UBL depth for this case was 0.36 m, and the free-stream wind speed was 5.97 m/s. Using the calculated pressure drop and the inflow wind profile, the values of u^* and z_0 can be calculated by applying the momentum integral method. The resulting u^* was 0.56 m/s, and z_0 was 0.0057 m, for the wind profile after passing through the staggered building array with uniform height, as shown in Fig. 5.5(c).

To evaluate the performance of the proposed method, we compared the pressure drop and wind profile obtained from the proposed method with the benchmarks. The methods used to extract the benchmark pressure drop and wind profile were consistent with those described in Section 5.2.1.2. For Case 2, the benchmark pressure drop was 5.09 Pa, and the pressure drop calculated by the proposed method exhibited a deviation of -1.57% from the benchmark. For evaluation of the wind profile, Fig. 5.5(c) compares the wind profile calculated by the proposed method with the benchmark. The benchmark wind profile resulted in $u^*_{\_CFD} = 0.54\ m/s$ and $z_{0\_CFD} = 0.0061\ m$. With the proposed method, the deviations in u^* and z_0 from the benchmark were 3.70% and -6.56%, respectively. Therefore, the proposed method exhibited good agreement in estimating urban wind profiles for a staggered building array with uniform height.

5.2.3. Case 3: Staggered building array with non-uniform height

5.2.3.1. Case setup

Case 3 consisted of a 9×9 staggered building array with varying building heights, as shown in Fig. 5.6(a) to (c). In the streamwise direction, buildings in adjacent rows were arranged in a staggered pattern. Within each row, all buildings had the same height; however, the height varied between adjacent rows. Specifically, the building dimensions were $0.06\,m \times 0.06\,m \times 0.06\,m$ for one row and $0.06\,m \times 0.06\,m \times 0.12\,m$ for the next. The average building height was 0.086 m, and thus the canopy height was set to 0.086 m when the selected urban canopy was modelled as a porous medium. The inflow wind profile was the same as in Case 1. According to the inflow wind profile and canopy height, the mean wind velocity within

the urban canopy was 2.42 m/s. For the CFD simulations used as benchmarks, the computational domain for Case 3 was defined as $2.22\,m\,(length) \times 1.2\,m\,(width) \times 0.72\,m\,(height)$, based on the guidelines from COST 732 [97] and AIJ [59], as shown in Fig. 5.6(a). The boundary conditions and solver settings were the same as those applied in Case 1 (see Section 5.2.1.1).

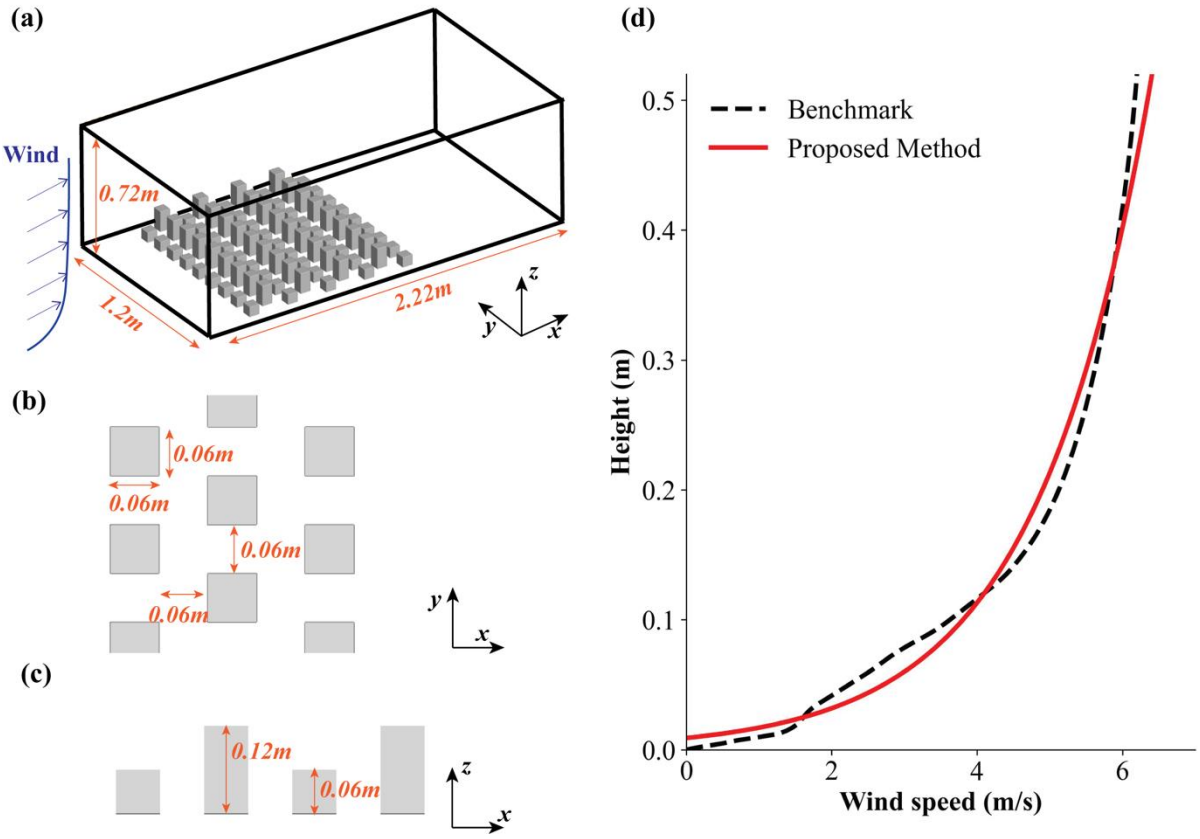

Fig. 5.6 (a) Schematic of the CFD domain; (b) top view; (c) side view of Case 3; and (d) comparison between the benchmark and the wind profile calculated by the proposed method for Case 3.

5.2.3.2. Estimation and evaluation of urban wind profile for Case 3

For calculation of the pressure drop by the porosity model, the urban morphology parameters for Case 3 were first determined. As shown in Fig. 5.6(a) to (c), the volume of the porous medium was 0.089 m^3, and the volume occupied by all buildings within the porous medium was 0.021 m^3. Consequently, the porosity of the urban canopy was 0.76. In regard to the fracture settings, there were 8 fractures with a tortuosity of 1.47 and an average width of 0.06

m, as the building arrangement was the same as that in Case 2. Using Eq. (5.19), the equivalent spherical diameter of the buildings (d_p) was calculated to be 0.11 m for Case 3. Using the information above, the pressure drop across the staggered building array with non-uniform height was calculated to be 7.55 Pa by the proposed method. We then estimated the wind profile based on the calculated pressure drop and inflow wind profile. For Case 3, the UBL depth was 0.72 m, and the corresponding free-stream wind speed was 6.59 m/s. The resulting u^* and z_0 for the urban wind profile in Case 3 were 0.65 m/s and 0.009 m, respectively, as shown in Fig. 5.6(c).

To evaluate the performance of the proposed method in Case 3, we first extracted the benchmark pressure drop and wind profile from the CFD simulations following the same procedure as described in Case 1 (see Section 5.2.1.2). The benchmark pressure drop for Case 3 was 7.74 Pa, and the pressure drop calculated by the proposed method (7.55 Pa) exhibited a deviation of -2.45% from the benchmark. For assessment of the calculated wind profile, Fig. 5.6(d) compares the wind profile calculated by the proposed model and the benchmark. The benchmark wind profile resulted in $u^*_{\_CFD} = 0.64\ m/s$ and $z_{0\_CFD} = 0.0090\ m$. The proposed method exhibited deviations of 1.56% for u^* and -13.46% for z_0 compared to the benchmark. Therefore, the proposed method showed good agreement in estimating urban wind profiles for a staggered building array with non-uniform height.

5.3. Application in a real urban layout

To assess the applicability of the proposed method in a real urban layout, Kowloon district in Hong Kong was selected as the study area. Kowloon is characterized by a complex and dense urban morphology [74], presenting a challenging environment for wind profile estimation. As described in Section 5.1.1, for the real urban layout, the inflow wind profiles for the proposed method were obtained from the WRF simulations at the urban edge. To determine urban morphology parameters for the real urban layout, building geometries and road networks were used for analysis (see Fig. 5.7(a)). Finally, to evaluate the applicability of the proposed method, the wind profile measured by radiosonde in the built-up area was used as the benchmark. Moreover, the wind profile calculated by the validated WRF model was included for

comparison. Each step for estimating wind profiles in the real urban layout is described in detail in the following subsections.

5.3.1. The inflow wind profile from WRF

The King's Park (KP) station, located in the built-up area and surrounded by high-rise buildings, was chosen as the target area in this study. Radiosonde measurements were conducted at the KP station at 00:00 and 12:00 each day. Therefore, the wind profile at the KP station at the time of 00:00 on 19 September 2023 was selected to evaluate the performance of the proposed method in estimating urban wind profiles in the built-up area. At this selected time, the wind direction was 120°. The distance from the target area to the urban edge along the streamwise direction was 2,350 m. For the width of the selected area, based on recommendations from the literature [61], at least three layers of buildings surrounding the target area should be considered. Therefore, the selected urban area was 2,350 m long and 643 m wide, as shown in Fig. 5.7(b). The inflow wind profile required for the proposed method was extracted from WRF simulations at the edge of this area, as showed in Fig. 5.7(b).

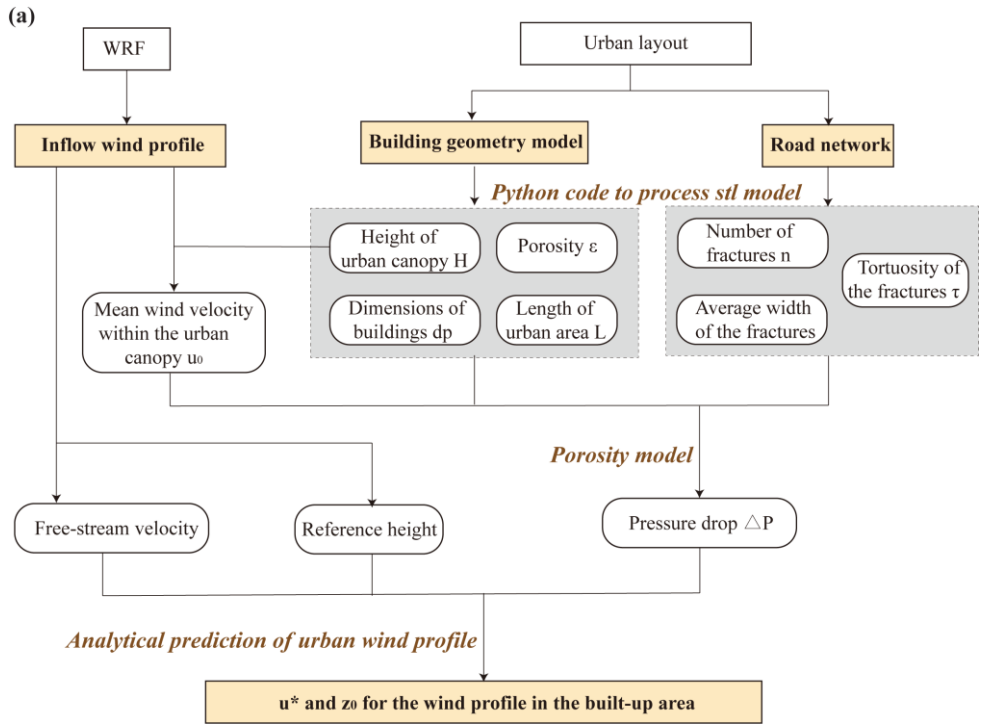

Fig. 5.7 (a) Flow chart of the proposed method for estimation of wind profiles in the real urban layout, and (b) the selected urban areas in the real urban layout.

For the setup of the WRF simulations, the Kowloon peninsula region was selected as the WRF study domain, as shown in Fig. 5.8. Three meteorological stations were located within this area. Specifically, the King's Park station was used to assess the performance of the proposed method, and measurements from two coastal meteorological stations, Star Ferry (SF) and Kai Tak (KT), were used to validate the WRF simulations. The geographical locations of these meteorological stations can be found in Fig. 5.8(a). We used WRFv4.0 to calculate the meteorological conditions. Three days (from 20:00 on 17 September to 02:00 on 20 September, 2023) were simulated, and the first 24 hours were taken as the spin-up period. To rationally reproduce the meteorological phenomena, the selected physical parameterization and the boundary conditions for WRF were set the same as in our previous study [74]. As shown in Fig. 5.8(b), three-nested domains were configured for WRF calculation using grid spacings of 1.8 km (128 × 128 grid points), 0.6 km (148 × 148 grid points), and 0.2 km (148 × 148 grid points) for a parent domain (d01) and two nested domains (d02, d03), respectively. The selected urban layout was located in the innermost domain of the WRF simulation. Note that although the width of the selected area exceeded the WRF grid size in d03, wind speed variations in the lateral direction were not considered, and the average wind profile was used in this study. WRF results were recorded every 10 minutes.

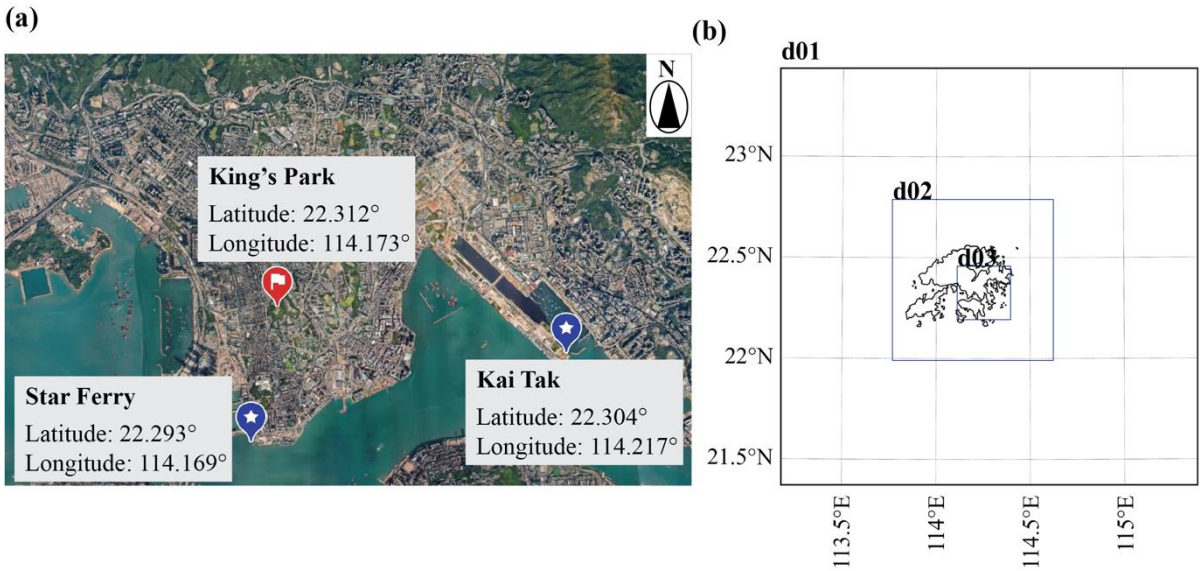

Fig. 5.8 (a) The locations of the weather stations in the innermost domain, and (b) the domain setup of WRF simulation.

To evaluate the performance of the WRF simulations, we compared the WRF outputs with measured data from two coastal meteorological stations (SF and KT) during the simulation period. The most recent 10-minute averaged wind speed, provided by local authorities, was used to represent the wind speed at each time point. For example, the wind speed at 20:00 was calculated as the average from 19:51 to 20:00. Fig. 5.9 compares the measured wind velocity and WRF outputs at the SF and KT stations.

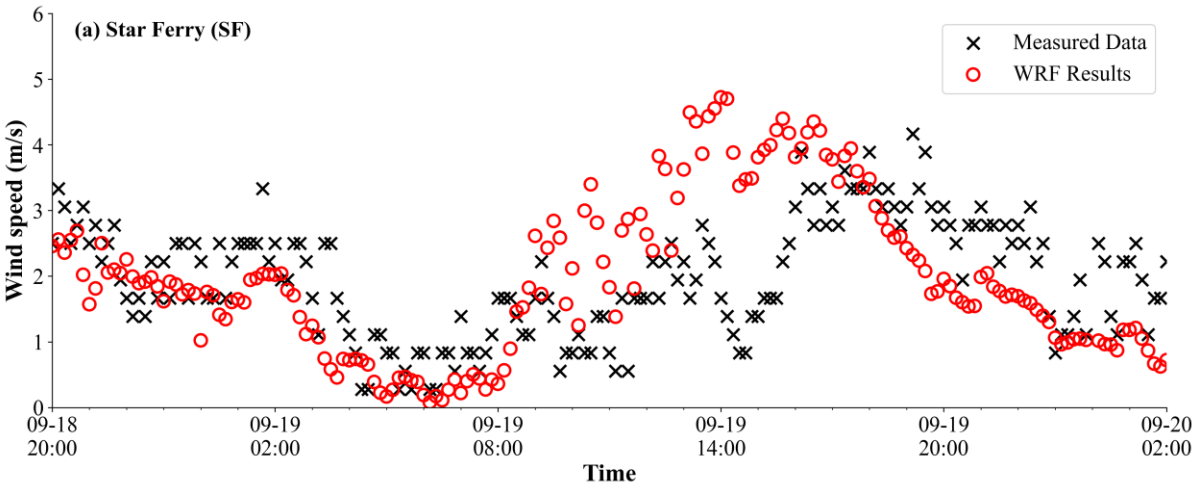

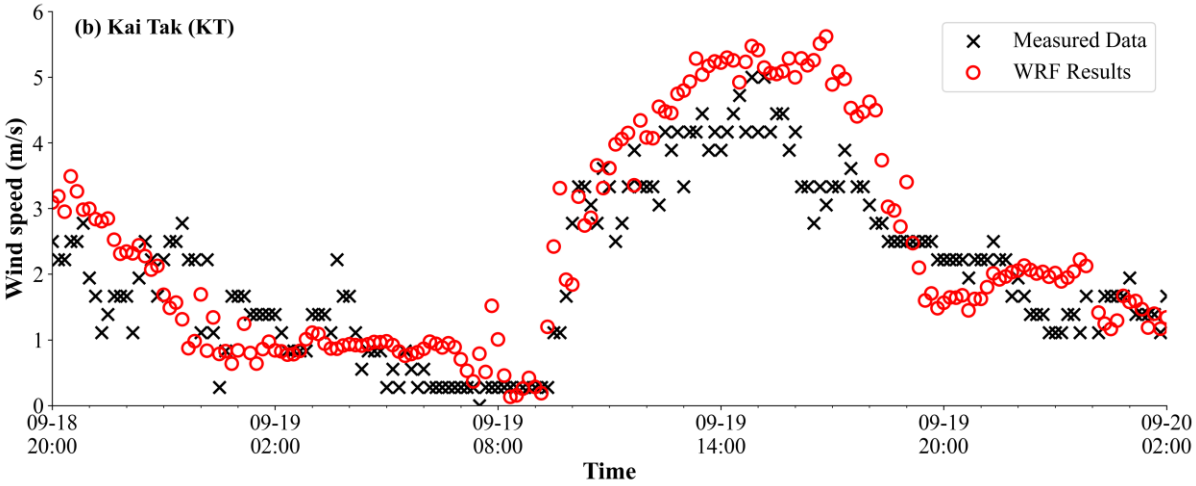

Fig. 5.9 Comparison of measured wind speed and WRF-simulated results over time for (a) SF station and (b) KT station.

To quantitatively evaluate the performance of the WRF, the RMSE has commonly been used to indicate the deviation of the simulated results compared with measured data [74]. The RMSE is expressed by Eq. (4.11). In this study, the number of measured data points was 181. The RMSE between the WRF results and measured data was 1.13 m/s at SF and 0.85 m/s at KT. In our previous study, we compared WRF results with measured data for 4 locations in Hong Kong, and the RMSE values ranged from 1.79 to 5.49 m/s [74]. Thus, the WRF simulations in this study provided acceptable results in calculating urban wind fields. Finally, the inflow wind profile of the proposed method was extracted from the WRF simulation at the edge of the selected urban area (see Fig. 5.7(b)), and the free-stream velocity was 4.6 m/s.

5.3.2. Urban morphology parameters for the urban layout

To estimate the urban wind profile by the proposed method, we determined the urban morphology parameters based on the building geometry and road networks, as shown in Fig. 5.10(a). The geometric data was generated by GIS technologies [127]. Note that only the building geometry was explicitly modelled, while the terrain and greenery were neglected. We developed a Python program to extract the footprint shapes and heights of buildings from the STL-format geometric model of the selected urban area. We analyzed these extracted data and calculated the average building height as 48.2 m. Thus, the height of the urban canopy (H) was 48.2 m. Combined with the inflow wind profile extracted from the WRF simulation, the mean

wind velocity within the urban canopy (u_0) was determined to be 1.92 m/s. Next, using the building dimensions obtained by Python code, the volume occupied by the buildings was calculated to be $1.09 \times 10^7\ m^3$. Based on the total volume of the porous medium, which was $7.28 \times 10^7\ m^3$, the porosity of the selected area (ε) was calculated to be 0.85. Additionally, the equivalent spherical diameter of the buildings (d_p) was calculated to be 31.23 m by analyzing building dimensions obtained by Python code.

We then determined the number of fractures (n), the tortuosity (τ), and the average width of fractures within the urban canopy ($\bar{B}$) based on the road network. As shown in Fig. 5.10(b), there were 4 fractures connecting the inlet and outlet of the porous medium, and the average length of the fractures was 3,097 m. With reference to the definitions of fractures (see Sections 2.2.4), n and τ were determined to be 4 and 1.31, respectively. Meanwhile, $\bar{B}$ was estimated based on road classifications and their corresponding widths. According to the regulations [151], the widths of major carriageways and minor carriageways are 7.3 m and 5.5 m, respectively, and the widths of major footpaths and minor footpaths are 3.7 m and 2.75 m, respectively. Therefore, the average road width in the selected area was calculated to be 4.61 m. Note that the road network does not include all the gaps between buildings, meaning that the closely connected building clusters were simplified as a single structure, as illustrated in Fig. 5.10(c).

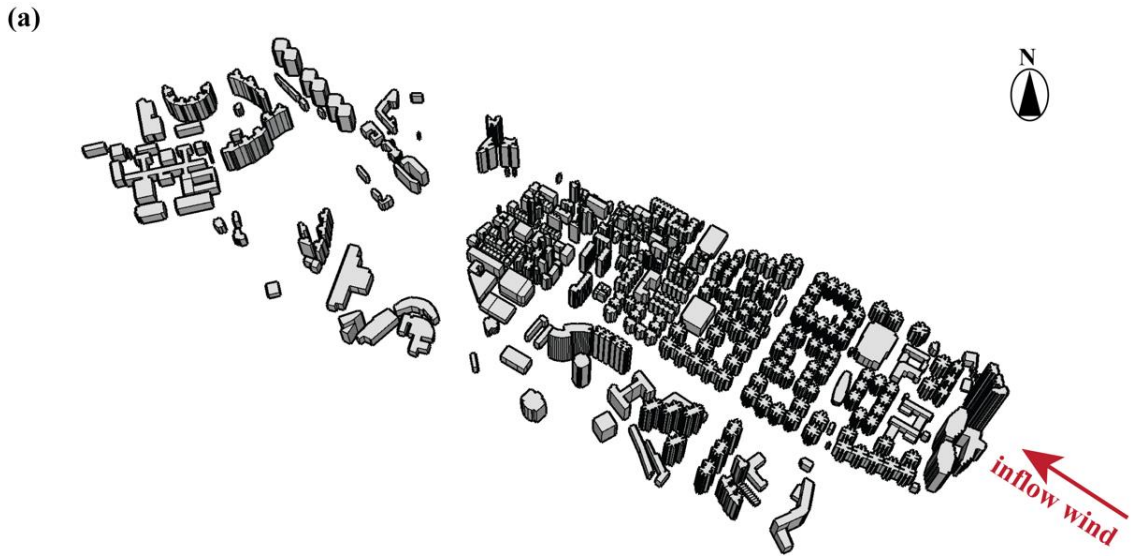

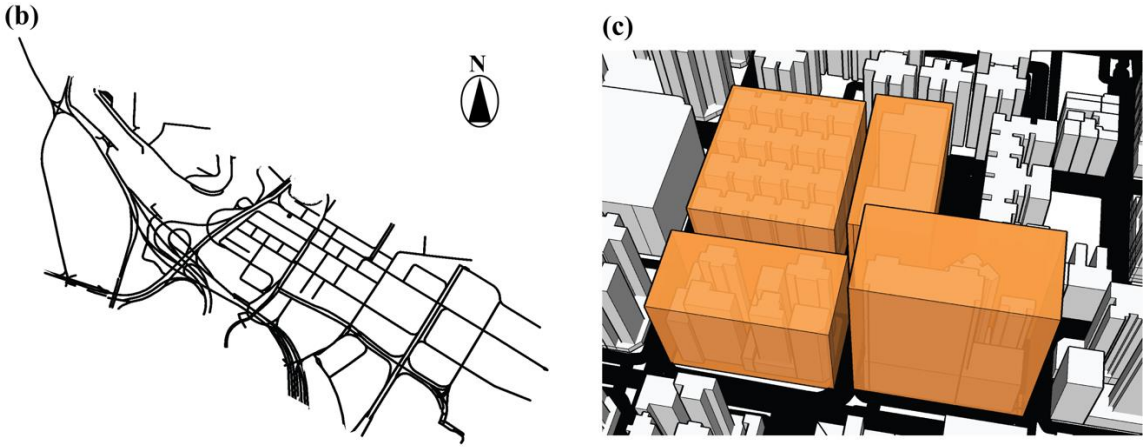

Fig. 5.10 (a) Building geometry model and (b) road networks in the selected urban area; (c) schematic of the simplification of building clusters.

5.3.3. Urban wind profile in built-up area

To obtain the wind profile in the target area using the proposed method, the values of the u^* and z_0 for the urban wind profile were estimated based on the inflow wind profiles and the urban morphology parameters obtained in Sections 4.1 and 4.2. The resulting u^* and z_0 for the wind profile in the target area were 0.67 m/s and 45.06 m, respectively. The value of z_0 is comparable to values reported in previous studies [152,153]. For instance, Gál and Unger [152] investigated the roughness length in Szeged, Hungary and found that in built-up areas with high-rise buildings, z_0 was around 37.

To evaluate the performance of the proposed method in the real urban layout, the measured data and WRF results were first fitted using Eq. (5.1) to derive their respective u^* and z_0 values. These fitted values were then compared with those calculated by the proposed method. Since WRF did not provide data on pressure drop across the selected urban layout, only the calculated wind profile was used for comparison with benchmarks. Fig. 5.11 compares the wind profile calculated by the proposed method with the measured data and WRF results. Note that for the measured wind profile, no data were available below 66 m, as the radiosonde balloon was released from that height. The u^* derived from measurement was 0.48 m/s, and WRF predicted a u^* of 0.65 m/s. It can be seen that the u^* values predicted by the proposed method (0.67 m/s) and by WRF (0.65 m/s) exhibited similar deviations from the measured value, approximately 36%. In terms of z_0, the value fitted from the measured data was 54.06 m. The proposed method

calculated a z_0 of 45.06 m, with a deviation of -16.59% from the measured data. In contrast, WRF produced a z_0 of 16.44 m, which deviated by -69.59% from the measurement. To sum up, the proposed method was found to be applicable in real urban layouts. It can estimate urban wind profiles reasonably well in densely built-up areas with complex building configurations, and it was found to perform better than WRF.

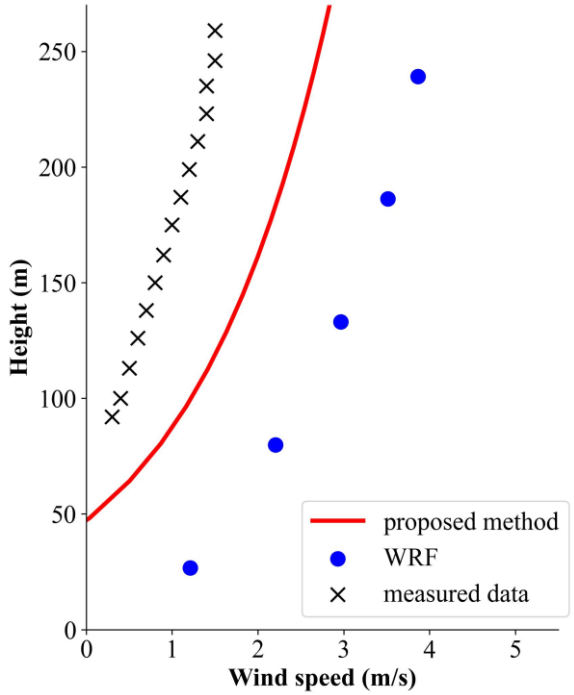

Fig. 5.11 Comparison between the benchmarks and the wind profile calculated by the proposed method for the real urban layout.

5.4. Discussion

In this study, we proposed a method for efficiently estimating wind profiles in built-up areas in real urban layouts. The selected urban area was modelled as a fractured porous medium, and the height of the medium was set to the average building height of the selected urban area. The variation in building heights was not considered in the proposed method. However, in real urban environments, variations in building heights are highly complex and can significantly impact the pressure drop of airflow. Accordingly, the wind profiles in built-up areas can be affected. For example, Sützl et al. [154] found that the drag force of uniform urban layouts can be nearly twice as low as that of areas with significant variations in building height. Hence, the

impact of variations in building heights should be considered in order to further improve the estimation of urban wind profiles in built-up areas. Additionally, road networks were used to estimate urban morphology parameters, such as the number of fractures, tortuosity, and average fracture width within the urban canopy. However, not all gaps between buildings were represented by road networks. As shown in Fig. 5.10(c), gaps between closely placed buildings were neglected. Therefore, further improvements are needed to better capture the complex geometry in real urban layouts. To sum up, the overestimation of urban wind profiles in the real urban layout can be attributed to the simplification in modelling urban morphology.

The proposed method allows for the rapid and flexible calculation of wind profiles in built-up areas. In practice, wind profiles in built-up areas are often used as inlet boundary conditions for CFD simulations to calculate urban wind distributions and pollutant dispersion [20,150,155]. Typically, the inlet boundary conditions are set empirically, approximated by logarithmic or power laws [17,22,61], rather than being specifically determined based on the building configurations and wind conditions in upstream areas. Therefore, the proposed method can be further used to provide inlet boundary conditions for CFD simulations. By considering the urban morphology and wind conditions in regions upstream from the target areas, we can improve the accuracy of CFD results.

5.5. Summary

This study proposed a method based on WRF and a porosity model to efficiently estimate wind profiles in built-up areas. First, WRF was used to simulate the wind profiles at the urban edge, and provided the inflow wind profiles for the proposed method. Next, the porosity model was employed to calculate the pressure drop of the airflow as it passed through the selected urban layout. Finally, the momentum integral method was applied to determine the urban wind profile in the built-up area. The performance of the proposed method was assessed in three generic urban layouts, with validated CFD simulations serving as benchmarks. We also demonstrated the application of the proposed method in a real urban layout. The measured wind profile was used as the benchmark. WRF-calculated wind profiles in this built-up area were also included for comparison. Within the scope of this study, the following conclusions can be drawn:

- For the generic urban layouts of an aligned building array with uniform height, a staggered building array with uniform height, and a staggered building array with non-uniform height, the proposed method accurately estimated the urban wind profile in the built-up areas.
- For the real urban layout, the proposed method estimated the urban wind profile reasonably well in the densely built-up area with complex building configurations and performed better than WRF.
- The proposed method significantly improves the accuracy of WRF-calculated wind profiles in built-up areas, thereby enhancing the applicability of the multiscale modelling approach for predicting urban wind distributions in real urban environments.

CHAPTER 6. Application of a combined analytical model and CFD method for calculating pedestrian-level wind distributions in real urban environments, with field measurements as the benchmark

In this chapter, the potential of a multiscale modelling approach for calculating pedestrian-level wind distributions was evaluated by combining CFD simulations with inflow wind profiles estimated using the method proposed in Chapter 5 (analytical-inlet-CFD). To assess the performance of the multiscale simulations, a public housing estate covering an area of $578\,m \times 560\,m$ was selected as the target area, and field measurements were conducted to collect pedestrian-level wind data in this real urban environment. The collected data then served as the benchmark for evaluating the accuracy of the analytical-inlet-CFD for outdoor wind simulations. Additionally, results from CFD with inflow boundary conditions directly extracted from WRF outputs (WRF-inlet-CFD) were also analyzed for comparison.

6.1. Methodology

6.1.1. Simulations for wind distribution at pedestrian level

To calculate wind distributions at the pedestrian level, the CFD method was adopted in this study. As discussed in Chapter 3, although LES performed best for calculating wind speed in the real urban layout, it was the most time-consuming model. To compromise between computational accuracy and efficiency, SRANS with SST $k-\omega$ model was used in this study to simulate pedestrian-level wind distributions. The governing equations and two partial differential transport equations for turbulence kinetic energy (k) and dissipation rate (ω) for the SST $k-\omega$ model turbulence model were shown in Eqs (3.1), (3.2), (3.6) and (3.7).

This investigation was implemented in an open-source CFD code, OpenFOAM v7 [156]. The solver settings, including wall function and pressure-velocity coupling scheme, were the same as those described in Section 3.1.5. The solutions were considered converged when the scaled

residuals reached their minimum values: 10^{-8} for continuity, 10^{-5} for momentum and turbulence.

6.1.2. Inflow boundary conditions for CFD

To evaluate the performance of urban wind profiles estimated through analytical prediction (see Chapter 5) in calculating pedestrian-level wind distributions, two methods were employed in this investigation to generate inflow wind profiles for the CFD simulations: analytical prediction (referred to as analytical-inlet-CFD) and mesoscale modelling (referred to as WRF-inlet-CFD). This section details these two methods for setting inflow boundary conditions for CFD simulations. Note that WRF outputs were required for both methods, and the physical parameterization schemes used in the WRF simulations can be found in Section 4.1.2.2.

6.1.2.1. Analytical-inlet-CFD

In this method, the urban wind profile estimated through the analytical prediction using a combined approach of WRF and a porosity model was set as the inflow boundary condition for the CFD simulation. As described in Chapter 5, wind profiles at the windward urban edge nearest to the target area were first extracted from WRF. Based on these extracted wind profiles and the urban morphology between the urban edge and the target area, the u^* and z_0 values for the wind profile within the built-up area was estimated. The calculated urban wind profile was subsequently used as the inflow wind profile for the CFD simulations.

As demonstrated in Section 5.3, the analytical prediction approach modelled the real urban layout as a porous medium, which did not allow for the calculation of wind profiles within the urban canopy (i.e. the region below the average building height). Consequently, wind profiles within the urban canopy are not directly provided by analytical predictions. Based on the study by Yao et al. [157], wind profiles within the urban canopy approximately follow an exponential distribution. Therefore, in this study, the wind profiles within the urban canopy were defined according to Eq. (6.1).

$$u(z) = u_H \exp(a(z/H - 1)) \quad (6.1)$$

where $u(z)$ is the wind speed (m/s) at the height z. H is the height of urban canopy (m), which can be calculated based on the average building height, and u_H is the wind speed (m/s) at height of urban canopy. a is an empirical constant related to urban morphology, typically ranging from 2 to 3 [158].

For the setting of the turbulence boundary conditions, turbulence kinetic energy (k) and turbulence dissipation rate (ε) was estimated by Eqs. (6.2) and (6.3) [98]:

$$k(\mathrm{z}) = \frac{u^{*2}}{\sqrt{C_\mu}} \quad (6.2)$$

$$\varepsilon(\mathrm{z}) = \frac{u^{*3}}{\kappa(z + z_0)} \quad (6.3)$$

where u^* and z_0 represent the friction velocity and roughness length, respectively, and their values were obtained from the analytical prediction. The von Karman constant (κ) was set to 0.41 [12,16,46], and the model constant (C_μ) was set to 0.085 [80] in this investigation.

6.1.2.2. WRF-inlet-CFD

For the WRF-inlet-CFD method, the vertical wind profile from the windward WRF grid nearest to the CFD domain was directly interpolated and applied as the inflow boundary for the CFD simulations. When the width of the target area exceeded the size of a single WRF grid, the averaged wind profile from multiple grids corresponding to the inlet of the target area was considered for setting the inflow boundary condition. The setup of k and ε was the same as shown in Eqs. (6.2) and (6.3).

In WRF simulations, the vertical grid size is determined by hydrostatic pressure [116], resulting in the height of the first vertical grid of WRF typically ranging from 30 m to 50 m above ground level [19,23]. Therefore, the wind profiles within the urban canopy cannot directly obtained

from WRF outputs. In this method, the wind profile within the urban canopy layer is defined using the same exponential distribution as shown in Eq. (6.1).

6.2. Field measurement

To evaluate the performance of analytical-inlet-CFD in calculating pedestrian-level wind distributions in real urban environments, it was necessary to compare the CFD simulation results with field measurement data. For this purpose, field measurements were conducted in this study. A public housing estate in Kwun Tong District, Hong Kong, was selected as the study area, as it is located within a typical built-up environment surrounded by dense buildings. As shown in Fig. 6.1, measurement points were placed in four public areas frequently used by residents within the estate: the landscape garden, the plaza, the playground and the sports field. An ultrasonic anemometer (Li560, LI-COR, USA) was individually placed at each measurement point to record wind speeds at a height of 1.6 m, representing pedestrian level. The data were collected with a temporal resolution of 40 Hz and an accuracy of ±1%.

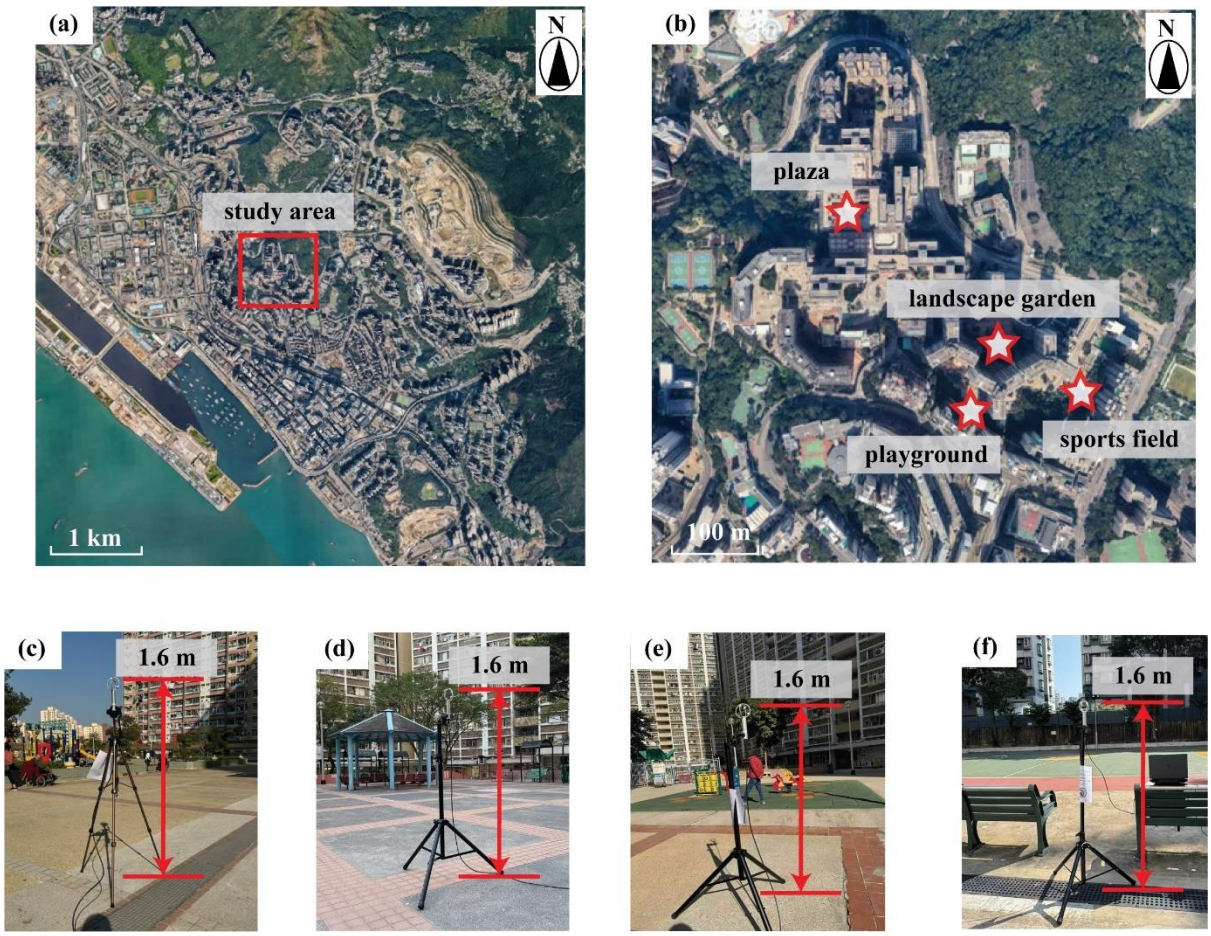

Fig. 6.1 Schematic of the field measurement: (a) Location and surrounding environment of the experiment site adopted from the Google earth; (b) Location of the measurement points; (c) The instrument placed in the plaza, (d) the landscape garden, (e) the playground and (f) the sports field.

The experiment was conducted between 09:00 and 17:00 on 18 January 2025. Note that during the measurement period, the instruments were continuously monitored by researchers to avoid unexpected wind speed deviations caused by nearby intense pedestrian activities, such as running or playing football.

6.3. Case setup

During the time period between 12:00 and 16:20 on 18 January 2025, the wind direction remained stable from the southeast. Therefore, this time period was chosen for the CFD

simulation. This section details the setup for CFD simulations, including the computational domain and grid, as well as the two methods for setting the inflow boundary conditions.

6.3.1. Computational domain and grid

The selected study area covered $578\ m \times 560\ m$, with the tallest building reaching a height of 102 m. According to recommendations by Liu et al. [61], three layers surrounding the target area should be explicitly established to accurately calculate wind distributions in CFD simulations. Based on this, the modeled area was set to $1200\ m \times 900\ m$. The geometric data was transformed from public sources such as OpenStreetMap, NASA, and USGS [127], as shown in Fig. 6.2(a). All buildings were explicitly resolved in this model; other obstacles, such as terrain, greenery and roads, were neglected. Following the guidelines of COST 732 [97] and AIJ [59], the computational domain for the selected study area was defined to be $3230\ m\ (length) \times 1909\ m\ (width) \times 612\ m\ (height)$, as shown in Fig. 6.2(b).

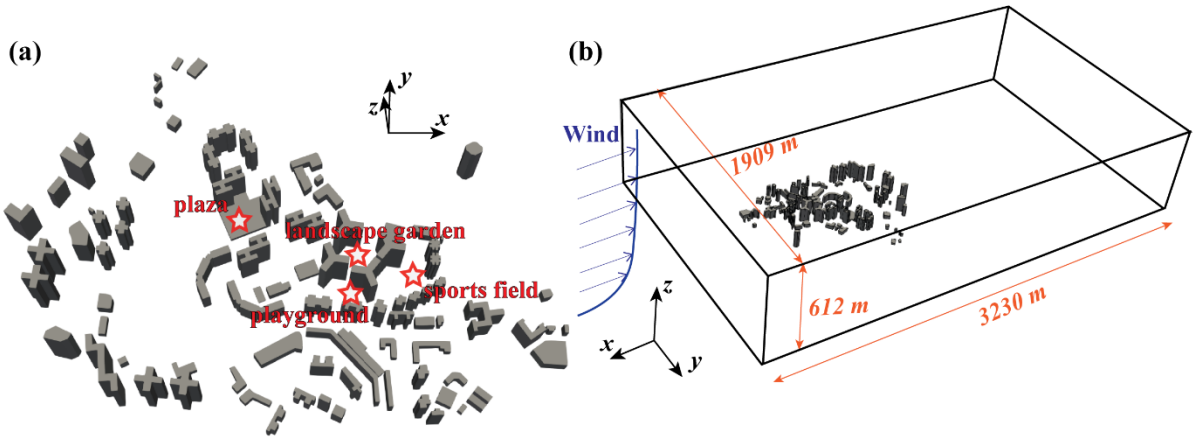

Fig. 6.2 (a) Building geometry and (b) computational domain of the study area.

The grid resolution near buildings and the ground surface was set to 1 m horizontally and 0.01 m vertically. The grid size gradually increased to 40 m in all directions with a stretching ratio of 1.2. The total grid number was 13.2 million, as shown in Fig. 6.3. The wall function used in this investigation was consistent with the one described in Section 3.1.5. The y+ values near the wall were around 3, indicating that the mesh resolution was sufficiently good for simulations using the SST $k-\omega$ model. The boundary conditions for bottom, top, lateral and

outlet surfaces of the computational domain were set the same as those in Section 4.2.2. The detailed setup for inflow boundary conditions can be found in the following subsections.

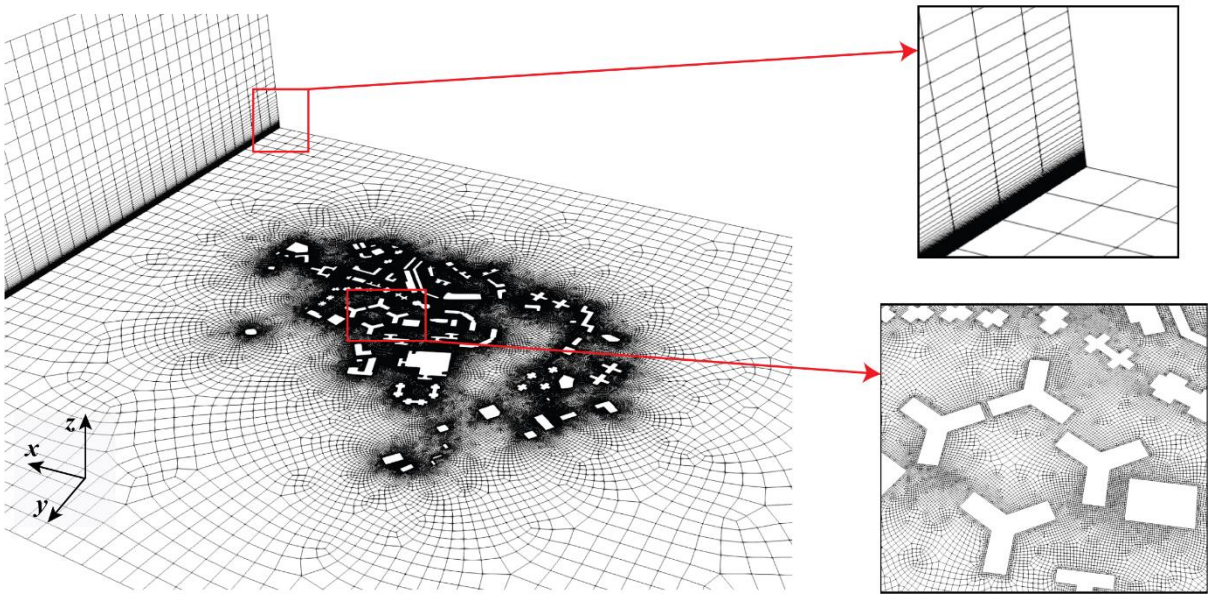

Fig. 6.3 Grid distribution for the study area.

6.3.2. Inflow boundary conditions

For both WRF-inlet-CFD and analytical-inlet-CFD, WRF outputs were required to generate the inflow boundary conditions for CFD simulations. the WRF simulation setup followed the same configuration as described in Section 5.3.1, and the validation of the WRF results is presented in Fig. 5.9. Unsteady simulation was conducted for WRF simulation, and the results were extracted with an interval of 20 minutes. The inflow boundary was defined as a velocity inlet, and the details of the two sets of inflow boundary conditions are described below.

6.3.2.1. Analytical-inlet-CFD

In analytical-inlet-CFD, the inflow boundary conditions were estimated based on WRF results at the urban edge and the urban morphology of the region through which the wind passed (i.e., the upstream area of the study area). As shown in Fig. 6.4, the urban edge located upstream of the study area was the mountainous terrain without buildings. Therefore, in this study, the WRF

results extracted from this urban edge were used in the analytical prediction method to estimate the wind profiles used for CFD simulations. The black solid lines in Fig. 6.4 represent WRF grids. Given that the length of the inlet surface was 1909 m, seven WRF grid cells were involved in defining the inflow boundary conditions. The averaged wind profiles from these seven grids were subsequently used to estimate the inflow boundary conditions for CFD simulations.

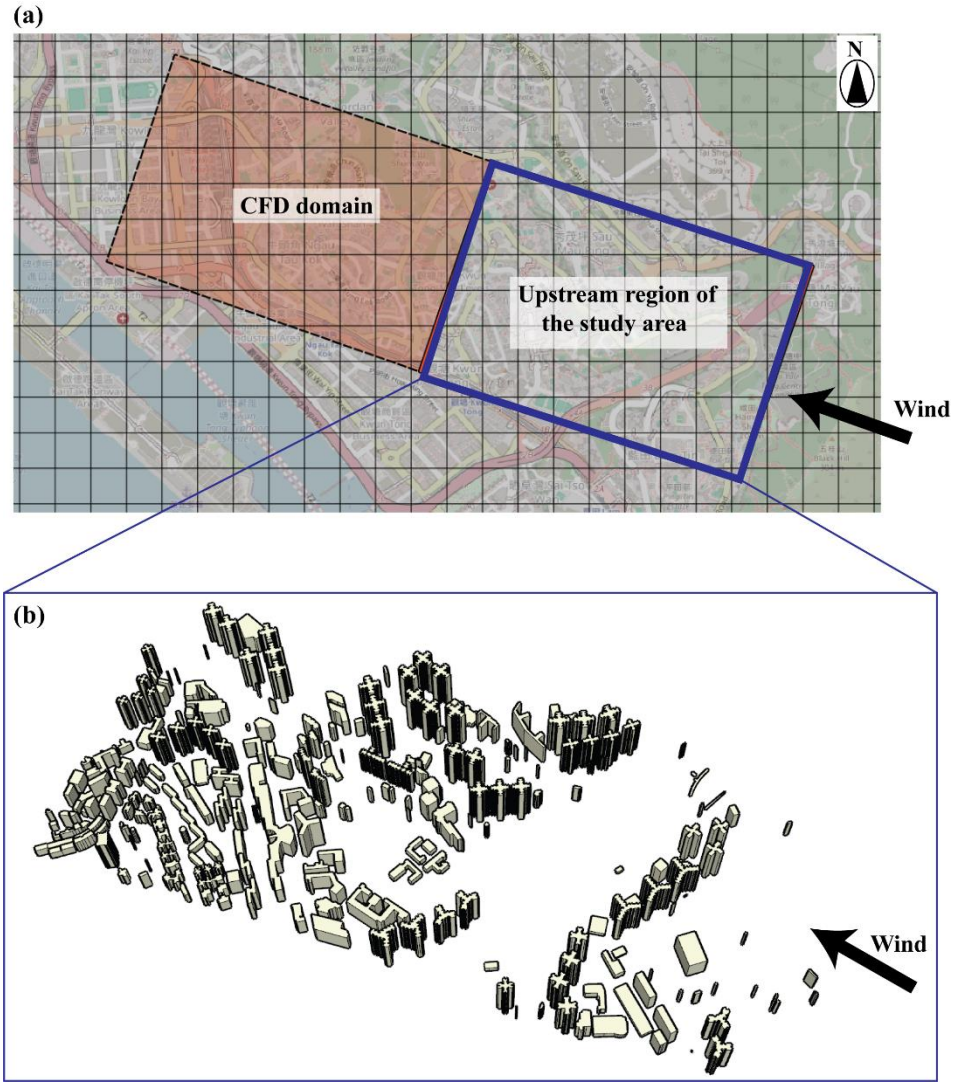

Fig. 6.4 (a) WRF data extraction location for analytical prediction and position of the CFD domain (black solid lines represent WRF grids), and (b) building geometry model used in the analytical prediction of wind profiles.

To calculate urban wind profiles using the analytical prediction method, the building geometry model of the upstream region of the study area was required, as shown in Fig. 6.4(b). Based on the building geometries, urban morphology parameters can be obtained. Specifically, the height of urban canopy was 69.53 m, porosity of the selected area (ε) was 0.82, the equivalent

spherical diameter of the buildings (d_p) was calculated to be 41.44 m, number of fractures (n) was 5, the tortuosity (τ) was 1.33, and the average width of fractures was 3.74 m. Using these urban morphology parameters along with the extracted WRF results, the u^* and z_0 values for urban wind profiles between 12:00 and 16:20 on 18 January 2025 were obtained, as presented in Table 6.1. The detailed methodology for deriving the urban morphology parameters and estimating the urban wind profiles is provided in Section 5.1.

Table 6.1 The u* and z_0 values for urban wind profiles between 12:00 and 16:20 on 18 January 2025

Time	12:00	12:20	12:40	13:00	13:20	13:40	14:00
u^*	0.54	0.57	0.55	0.45	0.49	0.56	0.48
z_0	45.96	42.41	45.94	45.49	45.96	42.93	45.96

Time	14:20	14:40	15:00	15:20	15:40	16:00	16:20
u^*	0.53	0.61	0.65	0.63	0.58	0.62	0.57
z_0	41.59	45.49	45.92	44.91	44.19	45.91	45.93

For the wind profiles within the urban canopy, the distribution was defined according to Eq. (6.1), with the value of a set to 2.3, based on results from a previous study conducted in built-up areas of Hong Kong with urban morphologies similar to the study region selected in this investigation [157].

6.3.2.2. WRF-inlet-CFD

In the WRF-inlet-CFD method, the inflow wind profile was directly extracted from the WRF wind profile closest to the inlet surface. As shown in Fig. 6.2(a), the inlet of the CFD domain spanned seven WRF grid cells. Therefore, the averaged wind profiles from these seven grids were used as the inflow wind profiles for WRF-inlet-CFD. For the wind profiles within the urban canopy, the distribution was set the same as described in Section 6.3.2.2.

6.4. Results

To evaluate the performance of urban wind profiles estimated through analytical prediction in calculating pedestrian-level wind distributions, we compared the simulated wind speeds from WRF-inlet-CFD and analytical-inlet-CFD with the field measurement data as the benchmark, as shown in Fig. 6.5. Wind measurement data with a temporal resolution of 40 Hz was averaged into 20 - minute data to compare with the CFD results, as the SRANS scheme was adopted for CFD simulations. Note that the most recent 20-minute averaged wind speed was used to represent the wind speed at each time point. For example, the wind speed at 12:00 was calculated as the average from 11:51 to 12:00. The results of analytical-inlet-CFD were mostly comparable with the measured values at plaza and sports field, while those of the WRF-inlet-CFD significantly deviated from the measured data at some time points. For example, at 13:40 for the plaza, the wind speed predicted by analytical-inlet-CFD was 0.80 m/s, closely matching the measured value of 0.88 m/s. In contrast, WRF-inlet-CFD predicted a wind speed of 0.32 m/s, which was 63.6% lower than the benchmark. For the sports fields, at 13:00, the measured wind speed was 0.35 m/s. Analytical-inlet-CFD provided a comparable result of 0.44 m/s, while WRF-inlet-CFD significantly overpredicted the wind speed at 1.47 m/s.

For both the landscape garden and the playground, discrepancies were observed between the CFD simulation results under both inflow conditions and the field measurements. At the landscape garden, for instance, the measured wind speed at 15:20 was 2.25 m/s. The result predicted by analytical-inlet-CFD was 1.01 m/s, underestimating the wind speed by 55.1%, while the results obtained from WRF-inlet-CFD was 0.59 m/s, underestimating by 73.8%. The large deviation at this point may be attributed to its location within a semi-enclosed cavity formed by surrounding buildings. In such configurations, wind distributions are sensitive to inflow wind direction. However, wind conditions in real urban environments are inherently transient, which makes them difficult to capture accurately using SRANS simulations. As for the playground, the site was located within a flow separation region, where accurately resolving the airflow remains challenging for CFD models. Tominaga et al. [24] conducted CFD simulations based on real urban layouts and validated the results using wind tunnel experiments. Their findings showed that CFD significantly underestimated wind speeds in flow separation zones. Overall, analytical-inlet-CFD showed better agreement with field measurements than WRF-inlet-CFD, although challenges remain in accurately predicting wind conditions in

complex urban configurations such as the area enclosed by buildings and flow separation regions.

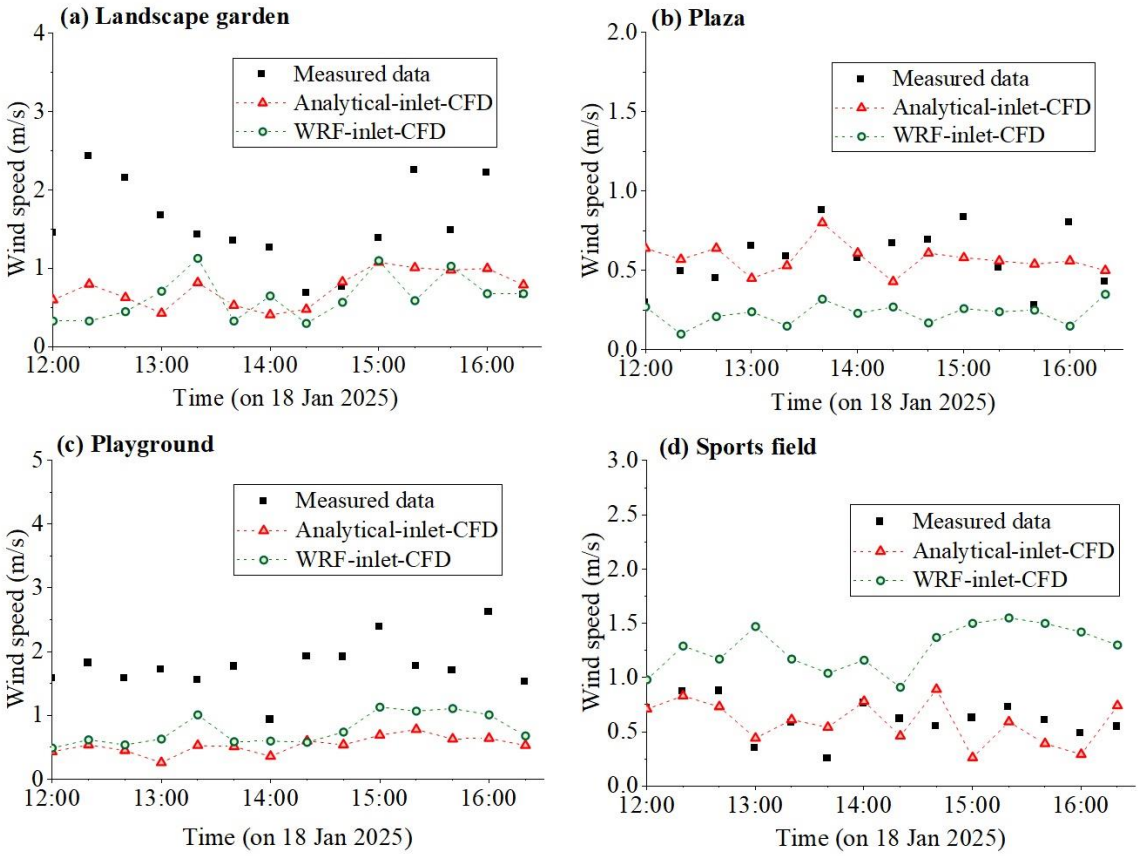

Fig. 6.5 Comparisons of the WRF-inlet-CFD results and Analytical-inlet-CFD results with the wind speed measured at (a) the landscape garden and (b) the plaza on 19 September 2023.

To quantitively assess the performance of the two methods, Table 6.2 presents the mean bias error (MBE) and root mean square error (RMSE) at the four measurement points. The formulas used to calculate these metrics are provided in Eqs. (10) and (11). As can be seen in Table 6.2, MBE and RMSE of the analytical-inlet-CFD method was lower than those of WRF-inlet-CFD at most of the sampling points. For example, at the plaza, analytical-inlet-CFD showed good agreement with measured data, with an MBE of -0.02 m/s and RMSE of 0.02 m/s. WRF-inlet-CFD had a larger underestimation compared to analytical-inlet-CFD, with MBE of -0.35 m/s and RMSE of 0.16 m/s. Therefore, analytical-inlet-CFD has greater potential than the WRF-inlet-CFD methods for accurately predicting pedestrian-level wind distributions in real urban environments.

Table 6.2 MBE and RMSE of wind speed at four measurement points.

Sampling point	Landscape garden		Plaza	
Method	Analytical-inlet-CFD	WRF-inlet-CFD	Analytical-inlet-CFD	WRF-inlet-CFD
MBE (m/s)	-0.79	-0.88	-0.02	-0.35
RMSE (m/s)	0.93	1.18	0.02	0.16

Sampling point	Playground		Sports field	
Method	Analytical-inlet-CFD	WRF-inlet-CFD	Analytical-inlet-CFD	WRF-inlet-CFD
MBE (m/s)	-1.27	-1.00	-0.05	0.66
RMSE (m/s)	1.72	1.11	0.03	0.51

6.5. Discussion

To evaluate the performance of the urban wind profiles obtained from the analytical prediction (see Chapter 5) in calculating the wind distributions at the pedestrian level, two methods were used to set the inflow boundary conditions for CFD simulations. In both methods, the wind profiles within the urban canopy followed exponential distributions, as shown in Eq. (6.1). However, previous research has adopted various laws to describe the wind distributions within the urban canopy [17,22,23,64]. For example, He et al. [17] used uniform-distributed wind profiles within the urban canopy to calculate the pedestrian-level wind distribution, while Blocken and Carmeliet [22] employed logarithmic-distributed wind profiles to define the inflow boundary conditions for CFD simulations. Therefore, it is essential to further investigate the impact of different wind distribution laws within the urban canopy on the accuracy of pedestrian-level wind simulations. Additionally, average wind profiles were used to define the inflow boundary conditions for the CFD simulations, rather than directly interpolating the outputs from the WRF grids involved. However, this simplification ignored the spanwise wind variations induced by complex land cover features in urban environments. For example, Blocken et al. [58] conducted CFD simulations to analyze wind flow over natural complex terrain consisting of irregular hills and found that such terrain produces significant wind speed gradients in the spanwise direction. Given these findings, it is important to incorporate

spanwise wind variations into the inflow boundary conditions of CFD simulations in future studies to improve the accuracy of urban wind simulations.

6.6. Summary

This investigation aimed to investigate the potential of a multiscale modelling approach for calculating pedestrian-level wind distributions. In this chapter, a public housing estate covering an area of $578\,m \times 560\,m$ was selected as the study area, and field measurements were conducted to collect wind speed at the pedestrian level. The measured data were then used as the benchmark to evaluate the performance of the analytical-inlet-CFD for calculating pedestrian-level wind distributions within the selected area. The simulated results obtained from the WRF-inlet-CFD were also included for comparison. Within the scope of this study, the following conclusions can be drawn:

- Wind profiles obtained directly from WRF and those estimated through analytical prediction can both be used to reproduce pedestrian-level wind distributions in real urban environments when combined with exponential wind profiles within the urban canopy.
- Analytical-inlet-CFD showed better agreement with field measurements than WRF-inlet-CFD, although challenges remain in accurately predicting wind conditions in complex urban configurations such as semi-enclosed spaces and flow separation regions.

CHAPTER 7. Conclusions and future work

This chapter summarizes the important conclusions and limitations of this study, and then discusses future work.

7.1. Conclusions

To apply the multiscale modelling approach for calculating pedestrian-level wind distributions in real urban environments, it is important to assess the applicability of various turbulence models used in computational fluid dynamics (CFD) method for outdoor wind simulations. This study first evaluated the performance of steady-state and unsteady-state Reynolds-averaged Navier-Stokes simulations (SRANS/URANS) and large-eddy simulation (LES) in predicting airflow and air pollutant dispersion in street canyons with both generic and real urban layouts, as presented in Chapter 3. For each layout, wind tunnel experiments with measured wind speed and pollutant concentration were available as benchmarks. In addition, instantaneous concentration fields were analyzed to assess the transient models. The results showed that in the generic urban layout, URANS with the SST $k-\omega$ model captured the large-scale fluctuations, while instantaneous results from URANS with the SST model did not change over time in the real urban layout. In both generic and real urban layouts, the RNG $k-\varepsilon$ model and SST $k-\omega$ model provided similar results for time-averaged wind speed and concentration distributions in SRANS and URANS simulations. Among all the selected RANS models, SRANS/URANS with the SST $k-\omega$ model showed best agreement with measured data in calculating wind speed. LES performed best in calculating wind speed and pollutant dispersion, but it was the most time-consuming model.

For calculation of the wind distributions in real urban environments, setting realistic inflow boundary conditions for CFD simulations is important. Wind profiles within the atmospheric boundary layer are significantly affected by local atmosphere circulation and diurnal variation. The Weather Research and Forecasting (WRF) model is a powerful mesoscale weather prediction model that can be used to provide realistic inflow boundary conditions. In Chapter

4, the potential of a combined WRF and CityFFD method (WRF-CityFFD) for calculating urban wind distributions was evaluated. We first validated the WRF and CityFFD models and then used the validated models in WRF-CityFFD to calculate the wind distribution in the Kowloon district of Hong Kong within an area of $3.5\ km \times 2.4\ km$. The wind speed data at two weather stations were used as a benchmark, and CityFFD with inflow boundary conditions from a semi-empirical method (semi-empirical-CityFFD) was also investigated for comparison. The WRF-CityFFD performed better than the semi-empirical-CityFFD in calculating wind velocities in urban microclimates. The power-law exponent for wind profiles should be carefully defined when conducting CFD simulations for complex urban layouts. Coastal areas with onshore wind conditions were more suitable for selection as inflow boundary conditions for WRF-CityFFD.

To improve the accuracy and efficiency of estimating wind profiles in built-up areas using WRF simulations, we proposed a method that combines WRF with a porosity model in Chapter 5. In this method, WRF provides the wind profile at the urban edge, and the porosity model calculates the airflow pressure drop across the selected urban area using a parametrized urban layout. The urban wind profile is then analytically determined with the momentum integral method. The performance of the proposed method was first evaluated in three generic urban layouts, with validated CFD simulations used as benchmarks. The proposed method was then applied in a real urban layout to demonstrate its performance, and the Kowloon district of Hong Kong, with an area of $2{,}350\ \mathrm{m} \times 643\ \mathrm{m}$, was selected as the target area. The wind profile measured with a radiosonde in the same region was used as a benchmark, and the WRF-calculated wind profile in the built-up area was also evaluated for comparison. The results showed that the method accurately estimated wind profiles in the generic urban layouts. In the real urban layout, the proposed method estimated the urban wind profile reasonably well in the densely built-up area with complex building configurations and performed better than WRF.

With the appropriate turbulence models investigated in Chapter 3, and the improved inflow boundary conditions proposed in Chapter 5, a multiscale modelling approach (analytical-inlet-CFD) for calculating the pedestrian-level wind distributions in real urban environments was evaluated in Chapter 6. In this investigation, a public housing estate with an area of $578\ m \times 560\ m$ was selected as the study area, and field measurements were conducted to measure the pedestrian-level wind speed in this real urban environment. The collected data then

served as the benchmark for evaluating the accuracy of the analytical-inlet-CFD for outdoor wind simulations. Additionally, results from CFD with inflow boundary conditions directly extracted from WRF outputs (WRF-inlet-CFD) were also analyzed for comparison. The results showed that wind profiles obtained directly from WRF and those estimated through analytical prediction can both be used to reproduce pedestrian-level wind distributions in real urban environments when combined with exponential wind profiles within the urban canopy. Analytical-inlet-CFD showed better agreement with field measurements than WRF-inlet-CFD, although challenges remain in accurately predicting wind conditions in complex urban configurations such as semi-enclosed spaces and flow separation regions.

7.2. Limitations

This study developed and validated a multiscale modelling approach for predicting pedestrian-level wind distributions in real urban environments; however, several limitations remain.

Although WRF outputs were used to define the inflow boundary conditions for CFD simulations, wind profiles within the urban canopy layer (i.e. below the average building height) cannot be directly obtained from WRF. Chapter 6 addressed this gap by approximating the near-ground wind profile using an exponential law, but the actual wind structure within the urban canopy remains insufficiently understood. The distribution of wind speed in this region is strongly influenced by complex urban morphology, and simplified assumptions may introduce uncertainties when simulating near-surface flow in built-up areas.

In addition to mean wind speed, turbulence characteristics are also critical in the urban wind environment [33]. Turbulence affects pollutant dispersion, pedestrian safety, and thermal comfort. Key parameters such as turbulent kinetic energy (TKE) and turbulence intensity can significantly influence pollutant transport and localized airflow variability. Although this study collected high-frequency wind speed data using ultrasonic anemometers, these turbulence metrics were not comprehensively analyzed in this study. Moreover, the performance of different turbulence closure models was not evaluated in detail, limiting the understanding of model suitability in reproducing turbulence dynamics in real urban conditions.

For model validation, field measurements from a single residential estate with relatively regular geometry and steady wind direction were used as a benchmark. While this site is representative of a typical residential setting in Hong Kong, the generalizability of the findings to other urban typologies or climatic contexts remains uncertain. Additional field validations across diverse urban layouts and environmental conditions are necessary to strengthen the robustness and applicability of the proposed approach.

In summary, the main limitations include insufficient understanding of wind profiles within the urban canopy, a lack of detailed evaluation of turbulence characteristics, and limited field validation. These issues suggest the need for further investigations to support the broader applicability of the multiscale modelling approach in accurately estimating pedestrian-level wind distributions in real urban environments.

7.3. Future work

Building upon the findings and limitations of this study, future work can proceed along the following directions to further advance urban wind environment modelling.

As described in Section 7.2, future research should aim to deepen the understanding of wind behavior within the urban canopy layer. This can be achieved through field measurements in urban environments to capture near-surface wind profiles, particularly within the canopy layer. Technologies such as LiDAR, SODAR, or vertically mounted sensor arrays can be utilized to obtain high-resolution data closer to the ground. These measurements will not only enhance the understanding of near-ground wind behavior but also support the validation and calibration of multiscale models, ensuring their accuracy in predicting pedestrian-level wind distributions. Second, advanced modelling approaches should be developed to better capture the complex interactions between wind flow and urban geometries. The high-resolution field data collected from near-surface measurements can serve as a benchmark for validating these models, such as the analytical prediction method in Chapter 5. These studies will facilitate the accuracy for urban wind simulations.

Second, future studies should focus on collecting and modelling key turbulence parameters, such as turbulent kinetic energy (TKE) and turbulence intensity, through both CFD simulations and field measurements. Additionally, the applicability of different turbulence closure models in simulating urban-scale turbulence should be further evaluated to improve the reliability of CFD predictions. To achieve these improvements, future efforts should be made to obtain accurate turbulence data in real urban environments. In Chapter 6, ultrasonic anemometers were used to collect high-resolution wind speed data at a frequency of 40 Hz. These datasets provide valuable opportunities for analyzing turbulence characteristics such as turbulence intensity, TKE, and other turbulence-related parameters at the pedestrian level. In addition to analyzing turbulence characteristics, the collected field data can also be used to evaluate and validate turbulence models in CFD simulations, ensuring that the models accurately capture turbulence behavior in real urban environments.

By applying the multiscale modelling approach proposed in this study, the accuracy of reproducing pedestrian-level wind distributions in real urban environments can be enhanced. Improving the accuracy of wind field simulations will have a significant impact on pollutant dispersion studies in urban environments. Specifically, accurate wind modelling is essential for predicting how pollutants are transported, diluted, and accumulated within complex urban geometries. Urban wind patterns directly affect the dispersion of pollutants in street canyons and open spaces, influencing both air quality and public health. Therefore, incorporating multiscale modelling approaches into pollutant dispersion simulations will enable future research to deliver more reliable predictions of pollutant concentration hotspots, exposure levels, and the overall dynamics of urban air quality. This integration would greatly enhance the practical application for pedestrian-level wind simulations in urban environments.

Supplementary Material

Grid-independence tests were conducted for both the generic urban layout and the real urban layout shown in Section 3.2. Since the RNG $k-\varepsilon$ model and SST $k-\omega$ model provided similar results for SRANS and URANS simulations, only the results of SRANS with the RNG $k-\varepsilon$ model and SRANS with the SST $k-\omega$ model are shown here.

For the generic urban layout, the height of the plotting line was 0.06 m, and it was located at $x = -0.27$ m and $y = 0$ m. A 2.46-million-cell grid was sufficiently fine for simulations with various turbulence models. The results for the generic urban layout case are shown in Fig. S.1.

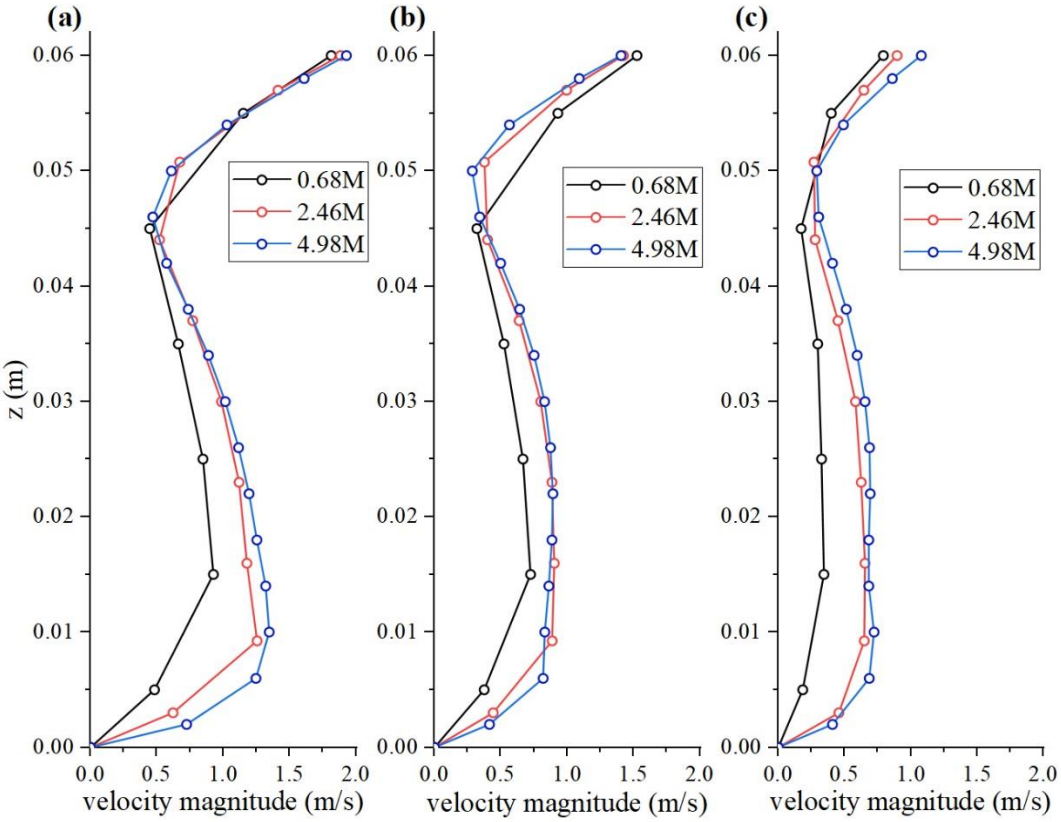

Fig. S.1 Grid-independence test for selected turbulence models: (a) SRANS with the RNG k-ε model, (b) SRANS with the SST k-ω model, and (c) LES.

For the real urban layout, the height of the plotting line was 0.2 m, and it was located at $x = -0.5$ m and $y = 0$ m. At this position, the ground surface started from 0.05 m. A 3.94-million-cell grid was used for simulations with various turbulence models. The results for the real urban layout case are shown in Fig. S.2.

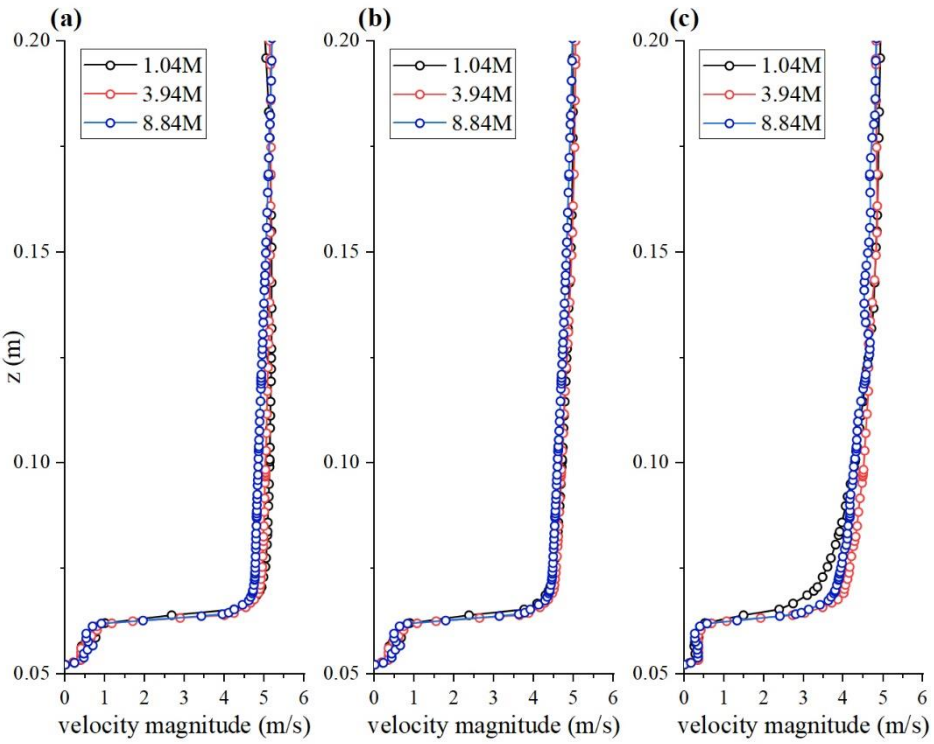

Fig. S.2 Grid-independence test for selected turbulence models: (a) SRANS with the RNG k-ε model, (b) SRANS with the SST k-ω model, and (c) LES.

BIBLIOGRAPHY

BIBLIOGRAPHY

[1] Climate Change 2014: Synthesis Report., in: Geneva, Switzerland, p. 151.

[2] K.S. Jon, Y. Luo, C.H. Sin, P. Cui, Y. Huang, J. Tokgo, Impacts of wind direction on the ventilation and pollutant dispersion of 3D street canyon with balconies, Build. Environ. 230 (2023) 110034. https://doi.org/10.1016/j.buildenv.2023.110034.

[3] A. Mochida, I.Y.F. Lun, Prediction of wind environment and thermal comfort at pedestrian level in urban area, J. Wind Eng. Ind. Aerodyn. 96 (2008) 1498–1527. https://doi.org/10.1016/j.jweia.2008.02.033.

[4] P. Moonen, T. Defraeye, V. Dorer, B. Blocken, J. Carmeliet, Urban Physics: Effect of the micro-climate on comfort, health and energy demand, Front. Archit. Res. 1 (2012) 197–228. https://doi.org/10.1016/j.foar.2012.05.002.

[5] Y. Zhou, Y. An, W. Huang, C. Chen, R. You, A combined deep learning and physical modelling method for estimating air pollutants' source location and emission profile in street canyons, Build. Environ. 219 (2022) 109246. https://doi.org/10.1016/j.buildenv.2022.109246.

[6] S. Fellini, L. Ridolfi, P. Salizzoni, Street canyon ventilation: Combined effect of cross-section geometry and wall heating, Q. J. R. Meteorol. Soc. 146 (2020) 2347–2367. https://doi.org/10.1002/qj.3795.

[7] N. Antoniou, H. Montazeri, H. Wigo, M.K.-A. Neophytou, B. Blocken, M. Sandberg, CFD and wind-tunnel analysis of outdoor ventilation in a real compact heterogeneous urban area: Evaluation using "air delay," Build. Environ. 126 (2017) 355–372. https://doi.org/10.1016/j.buildenv.2017.10.013.

[8] B. Blocken, J. Carmeliet, Pedestrian Wind Environment around Buildings: Literature Review and Practical Examples, J. Therm. Envel. Build. Sci. 28 (2004) 107–159. https://doi.org/10.1177/1097196304044396.

[9] B. Blocken, J. Carmeliet, T. Stathopoulos, CFD evaluation of wind speed conditions in passages between parallel buildings—effect of wall-function roughness modifications for the atmospheric boundary layer flow, J. Wind Eng. Ind. Aerodyn. 95 (2007) 941–962. https://doi.org/10.1016/j.jweia.2007.01.013.

[10] T. van Druenen, T. van Hooff, H. Montazeri, B. Blocken, CFD evaluation of building geometry modifications to reduce pedestrian-level wind speed, Build. Environ. 163 (2019) 106293. https://doi.org/10.1016/j.buildenv.2019.106293.

[11] J. Liu, J. Niu, CFD simulation of the wind environment around an isolated high-rise building: An evaluation of SRANS, LES and DES models, Build. Environ. 96 (2016) 91–106. https://doi.org/10.1016/j.buildenv.2015.11.007.

[12] X. Zheng, J. Yang, CFD simulations of wind flow and pollutant dispersion in a street canyon with traffic flow: Comparison between RANS and LES, Sustain. Cities Soc. 75 (2021) 103307. https://doi.org/10.1016/j.scs.2021.103307.

[13] Y. Tominaga, T. Stathopoulos, Steady and unsteady RANS simulations of pollutant dispersion around isolated cubical buildings: Effect of large-scale fluctuations on the concentration field, J. Wind Eng. Ind. Aerodyn. 165 (2017) 23–33. https://doi.org/10.1016/j.jweia.2017.02.001.

[14] Š. Nosek, V. Fuka, L. Kukačka, Z. Kluková, Z. Jaňour, Street-canyon pollution with respect to urban-array complexity: The role of lateral and mean pollution fluxes, Build. Environ. 138 (2018) 221–234. https://doi.org/10.1016/j.buildenv.2018.04.036.

[15] C. Yuan, E. Ng, L.K. Norford, Improving air quality in high-density cities by understanding the relationship between air pollutant dispersion and urban morphologies, Build. Environ. 71 (2014) 245–258. https://doi.org/10.1016/j.buildenv.2013.10.008.

[16] S. Liu, W. Pan, H. Zhang, X. Cheng, Z. Long, Q. Chen, CFD simulations of wind distribution in an urban community with a full-scale geometrical model, Build. Environ. 117 (2017) 11–23. https://doi.org/10.1016/j.buildenv.2017.02.021.

[17] Y. He, C. Yuan, C. Ren, E. Ng, Urban ventilation assessment with improved vertical wind profile in high-density cities – Comparisons between LiDAR and conventional methods, J. Wind Eng. Ind. Aerodyn. 228 (2022) 105116. https://doi.org/10.1016/j.jweia.2022.105116.

[18] Zhang X., Bao J.-W., Chen B., Grell E.D., A Three-Dimensional Scale-Adaptive Turbulent Kinetic Energy Scheme in the WRF-ARW Model, (2018). https://doi.org/10.1175/MWR-D-17-0356.1.

[19] R.F. Banks, J. Tiana-Alsina, J.M. Baldasano, F. Rocadenbosch, A. Papayannis, S. Solomos, C.G. Tzanis, Sensitivity of boundary-layer variables to PBL schemes in the WRF model based on surface meteorological observations, lidar, and radiosondes during the HygrA-CD campaign, Atmospheric Res. 176–177 (2016) 185–201. https://doi.org/10.1016/j.atmosres.2016.02.024.

[20] K. An, J.C.H. Fung, S.H.L. Yim, Sensitivity of inflow boundary conditions on downstream wind and turbulence profiles through building obstacles using a CFD approach, J. Wind Eng. Ind. Aerodyn. 115 (2013) 137–149. https://doi.org/10.1016/j.jweia.2013.01.004.

[21] M. Balogh, A. Parente, C. Benocci, RANS simulation of ABL flow over complex terrains applying an Enhanced k-ε model and wall function formulation: Implementation and comparison for fluent and OpenFOAM, J. Wind Eng. Ind. Aerodyn. 104–106 (2012) 360–368. https://doi.org/10.1016/j.jweia.2012.02.023.

[22] B. Blocken, J. Carmeliet, Pedestrian wind conditions at outdoor platforms in a high-rise apartment building: generic sub-configuration validation, wind comfort assessment and uncertainty issues, Wind Struct. 11 (2008) 51–70. https://doi.org/10.12989/WAS.2008.11.1.051.

[23] C. Huang, J. Yao, B. Fu, J.K. Calautit, C. Zhao, J. Huang, Q. Ban, Sensitivity analysis of WRF-CFD-based downscaling methods for evaluation of urban pedestrian-level wind, Urban Clim. 49 (2023) 101569. https://doi.org/10.1016/j.uclim.2023.101569.

[24] Y. Tominaga, R. Yoshie, A. Mochida, H. Kataoka, K. Harimoto, T. Nozu, Cross Comparisons of CFD Prediction for Wind Environment at Pedestrian Level around Buildings Part 2 : Comparison of Results for Flowfield around Building Complex in Actual Urban Area, Sixth Asia-Pac. Conf. Wind Eng. APCWE-VI (2005).

[25] L. Shen, Y. Han, M. Lihua, L. Xu, G. Xu, C.S. Cai, Assessment of the influences of post-construction facilities on pedestrian-level wind environment: An experimental study in Changsha, China, Urban Clim. 47 (2023) 101366. https://doi.org/10.1016/j.uclim.2022.101366.

[26] B. Blocken, T. Stathopoulos, J.P.A.J. van Beeck, Pedestrian-level wind conditions around buildings: Review of wind-tunnel and CFD techniques and their accuracy for wind comfort assessment, Build. Environ. 100 (2016) 50–81. https://doi.org/10.1016/j.buildenv.2016.02.004.

[27] Takumi Tachibana, Ryuichiro Yoshie, Satoru Nakayama, Koichi Mitashita, Comparison between field measurement and wind tunnel experiments of gas dispersion in an urban area and verification of similarity law, J. Wind Eng. 47 (2022) 39–52. http://dx.doi.org/10.5359/jwe.47.39.

[28] Hong Kong Observatory Open Data, (n.d.). https://www.hko.gov.hk/en/abouthko/opendata_intro.htm (accessed July 24, 2024).

[29] S.E. Belcher, I.N. Harman, J.J. Finnigan, The Wind in the Willows: Flows in Forest Canopies in Complex Terrain, Annu. Rev. Fluid Mech. 44 (2012) 479–504. https://doi.org/10.1146/annurev-fluid-120710-101036.

[30] A. Ricci, B. Blocken, On the reliability of the 3D steady RANS approach in predicting microscale wind conditions in seaport areas: The case of the IJmuiden sea lock, J. Wind Eng. Ind. Aerodyn. 207 (2020) 104437. https://doi.org/10.1016/j.jweia.2020.104437.

[31] A. Christen, R. Vogt, M.W. Rotach, Profile measurements of selected turbulence characteristics over different urban surfaces.

[32] I. Eliasson, B. Offerle, C.S.B. Grimmond, S. Lindqvist, Wind fields and turbulence statistics in an urban street canyon, Atmos. Environ. 40 (2006) 1–16. https://doi.org/10.1016/j.atmosenv.2005.03.031.

[33] J. Zou, Y. Yu, J. Liu, J. Niu, K. Chauhan, C. Lei, Field measurement of the urban pedestrian level wind turbulence, Build. Environ. 194 (2021) 107713. https://doi.org/10.1016/j.buildenv.2021.107713.

[34] F.T. DePaul, C.M. Sheih, Measurements of wind velocities in a street canyon, Atmospheric Environ. 1967 20 (1986) 455–459. https://doi.org/10.1016/0004-6981(86)90085-5.

[35] T. van Hooff, B. Blocken, Coupled urban wind flow and indoor natural ventilation modelling on a high-resolution grid: A case study for the Amsterdam ArenA stadium, Environ. Model. Softw. 25 (2010) 51–65. https://doi.org/10.1016/j.envsoft.2009.07.008.

[36] Y. Toparlar, B. Blocken, P. Vos, G.J.F. van Heijst, W.D. Janssen, T. van Hooff, H. Montazeri, H.J.P. Timmermans, CFD simulation and validation of urban microclimate: A case study for Bergpolder Zuid, Rotterdam, Build. Environ. 83 (2015) 79–90. https://doi.org/10.1016/j.buildenv.2014.08.004.

[37] A. Mazzoldi, T. Hill, J.J. Colls, CFD and Gaussian atmospheric dispersion models: A comparison for leak from carbon dioxide transportation and storage facilities, Atmos. Environ. 42 (2008) 8046–8054. https://doi.org/10.1016/j.atmosenv.2008.06.038.

[38] Y. Tominaga, T. Stathopoulos, CFD Modeling of Pollution Dispersion in Building Array: Evaluation of turbulent scalar flux modeling in RANS model using LES results, J. Wind Eng. Ind. Aerodyn. 104–106 (2012) 484–491. https://doi.org/10.1016/j.jweia.2012.02.004.

[39] B. Blocken, W.D. Janssen, T. van Hooff, CFD simulation for pedestrian wind comfort and wind safety in urban areas: General decision framework and case study for the Eindhoven University campus, Environ. Model. Softw. 30 (2012) 15–34. https://doi.org/10.1016/j.envsoft.2011.11.009.

[40] T. Shui, J. Liu, Q. Yuan, Y. Qu, H. Jin, J. Cao, L. Liu, X. Chen, Assessment of pedestrian-level wind conditions in severe cold regions of China, Build. Environ. 135 (2018) 53–67. https://doi.org/10.1016/j.buildenv.2018.03.006.

[41] N. Antoniou, H. Montazeri, M. Neophytou, B. Blocken, CFD simulation of urban microclimate: Validation using high-resolution field measurements, Sci. Total Environ. 695 (2019) 133743. https://doi.org/10.1016/j.scitotenv.2019.133743.

[42] S. Yang, L. (Leon) Wang, T. Stathopoulos, A.M. Marey, Urban microclimate and its impact on built environment – A review, Build. Environ. 238 (2023) 110334. https://doi.org/10.1016/j.buildenv.2023.110334.

[43] P. Gousseau, B. Blocken, T. Stathopoulos, G.J.F. van Heijst, CFD simulation of near-field pollutant dispersion on a high-resolution grid: A case study by LES and RANS for a building group in downtown Montreal, Atmos. Environ. 45 (2011) 428–438. https://doi.org/10.1016/j.atmosenv.2010.09.065.

[44] Y. Tominaga, T. Stathopoulos, CFD simulation of near-field pollutant dispersion in the urban environment: A review of current modeling techniques, Atmos. Environ. 79 (2013) 716–730. https://doi.org/10.1016/j.atmosenv.2013.07.028.

[45] Y. Tominaga, T. Stathopoulos, Numerical simulation of dispersion around an isolated cubic building: Comparison of various types of k–ε models, Atmos. Environ. 43 (2009) 3200–3210. https://doi.org/10.1016/j.atmosenv.2009.03.038.

[46] L. He, J. Hang, X. Wang, B. Lin, X. Li, G. Lan, Numerical investigations of flow and passive pollutant exposure in high-rise deep street canyons with various street aspect ratios and viaduct settings, Sci. Total Environ. 584–585 (2017) 189–206. https://doi.org/10.1016/j.scitotenv.2017.01.138.

[47] B. Blocken, LES over RANS in building simulation for outdoor and indoor applications: A foregone conclusion?, Build. Simul. 11 (2018) 821–870. https://doi.org/10.1007/s12273-018-0459-3.

[48] H. Yu, J. Thé, Simulation of gaseous pollutant dispersion around an isolated building using the k–ω SST (shear stress transport) turbulence model, J. Air Waste Manag. Assoc. 67 (2017) 517–536. https://doi.org/10.1080/10962247.2016.1232667.

[49] Y. Tominaga, Flow around a high-rise building using steady and unsteady RANS CFD: Effect of large-scale fluctuations on the velocity statistics, J. Wind Eng. Ind. Aerodyn. 142 (2015) 93–103. https://doi.org/10.1016/j.jweia.2015.03.013.

[50] S.M. Salim, K.C. Ong, Performance of RANS, URANS and LES in the Prediction of Airflow and Pollutant Dispersion, in: H.K. Kim, S.-I. Ao, B.B. Rieger (Eds.), IAENG Trans. Eng. Technol. Spec. Ed. World Congr. Eng. Comput. Sci. 2011, Springer Netherlands, Dordrecht, 2013: pp. 263–274. https://doi.org/10.1007/978-94-007-4786-9_21.

[51] Y. Tominaga, T. Stathopoulos, CFD modeling of pollution dispersion in a street canyon: Comparison between LES and RANS, J. Wind Eng. Ind. Aerodyn. 99 (2011) 340–348. https://doi.org/10.1016/j.jweia.2010.12.005.

[52] L. Wang, W. Tian, P. Zheng, Review of the Numerical Simulation of the Wind and Pollutant Diffusion in Urban Street Canyon under the Influence of Trees, Buildings 13 (2023) 1088. https://doi.org/10.3390/buildings13041088.

[53] R. Yoshie, G. Jiang, T. Shirasawa, J. Chung, CFD simulations of gas dispersion around high-rise building in non-isothermal boundary layer, J. Wind Eng. Ind. Aerodyn. 99 (2011) 279–288. https://doi.org/10.1016/j.jweia.2011.01.006.

[54] H.W. Tieleman, Strong wind observations in the atmospheric surface layer, J. Wind Eng. Ind. Aerodyn. 96 (2008) 41–77. https://doi.org/10.1016/j.jweia.2007.03.003.

[55] Q.S. Li, L. Zhi, F. Hu, Boundary layer wind structure from observations on a 325 m tower, J. Wind Eng. Ind. Aerodyn. 98 (2010) 818–832. https://doi.org/10.1016/j.jweia.2010.08.001.

[56] N.J. Cook, The Deaves and Harris ABL model applied to heterogeneous terrain, J. Wind Eng. Ind. Aerodyn. 66 (1997) 197–214. https://doi.org/10.1016/S0167-6105(97)00034-2.

[57] B. Blocken, T. Stathopoulos, J. Carmeliet, CFD simulation of the atmospheric boundary layer: wall function problems, Atmos. Environ. 41 (2007) 238–252. https://doi.org/10.1016/j.atmosenv.2006.08.019.

[58] B. Blocken, A. van der Hout, J. Dekker, O. Weiler, CFD simulation of wind flow over natural complex terrain: Case study with validation by field measurements for Ria de Ferrol, Galicia, Spain, J. Wind Eng. Ind. Aerodyn. 147 (2015) 43–57. https://doi.org/10.1016/j.jweia.2015.09.007.

[59] Y. Tominaga, A. Mochida, R. Yoshie, H. Kataoka, T. Nozu, M. Yoshikawa, T. Shirasawa, AIJ guidelines for practical applications of CFD to pedestrian wind environment around buildings, J. Wind Eng. Ind. Aerodyn. 96 (2008) 1749–1761. https://doi.org/10.1016/j.jweia.2008.02.058.

[60] J. Wieringa, Updating the Davenport roughness classification, J. Wind Eng. Ind. Aerodyn. 41 (1992) 357–368. https://doi.org/10.1016/0167-6105(92)90434-C.

[61] S. Liu, W. Pan, X. Zhao, H. Zhang, X. Cheng, Z. Long, Q. Chen, Influence of surrounding buildings on wind flow around a building predicted by CFD simulations, Build. Environ. 140 (2018) 1–10. https://doi.org/10.1016/j.buildenv.2018.05.011.

[62] M. Huang, Z. Gao, S. Miao, F. Chen, M.A. LeMone, J. Li, F. Hu, L. Wang, Estimate of Boundary-Layer Depth Over Beijing, China, Using Doppler Lidar Data During SURF-2015, Bound.-Layer Meteorol. 162 (2017) 503–522. https://doi.org/10.1007/s10546-016-0205-2.

[63] M.M.F. Wong, J.C.H. Fung, J. Ching, P.P.S. Yeung, J.W.P. Tse, C. Ren, R. Wang, M. Cai, Evaluation of uWRF performance and modeling guidance based on WUDAPT and NUDAPT UCP datasets for Hong Kong, Urban Clim. 28 (2019) 100460. https://doi.org/10.1016/j.uclim.2019.100460.

[64] Y. He, C. Ren, H.W.L. Mak, C. Lin, Z. Wang, J.C.H. Fung, Y. Li, A.K.H. Lau, E. Ng, Investigations of high-density urban boundary layer under summer prevailing wind conditions with Doppler LiDAR: A case study in Hong Kong, Urban Clim. 38 (2021) 100884. https://doi.org/10.1016/j.uclim.2021.100884.

[65] C.H. Halios, J.F. Barlow, Observations of the Morning Development of the Urban Boundary Layer Over London, UK, Taken During the ACTUAL Project, Bound.-Layer Meteorol. 166 (2018) 395–422. https://doi.org/10.1007/s10546-017-0300-z.

[66] J. Lim, Y. Akashi, R. Ooka, H. Kikumoto, Y. Choi, A probabilistic approach to the energy-saving potential of natural ventilation: Effect of approximation method for approaching wind velocity, Build. Environ. 122 (2017) 94–104. https://doi.org/10.1016/j.buildenv.2017.06.008.

[67] S. Du, X. Zhang, X. Jin, X. Zhou, X. Shi, A review of multi-scale modelling, assessment, and improvement methods of the urban thermal and wind environment, Build. Environ. 213 (2022) 108860. https://doi.org/10.1016/j.buildenv.2022.108860.

[68] J.G. Powers, J.B. Klemp, W.C. Skamarock, C.A. Davis, J. Dudhia, D.O. Gill, J.L. Coen, D.J. Gochis, R. Ahmadov, S.E. Peckham, G.A. Grell, J. Michalakes, S. Trahan, S.G. Benjamin, C.R. Alexander, G.J. Dimego, W. Wang, C.S. Schwartz, G.S. Romine, Z. Liu, C. Snyder, F. Chen, M.J. Barlage, W. Yu, M.G. Duda, The Weather Research and Forecasting Model: Overview, System Efforts, and Future Directions, (2017). https://doi.org/10.1175/BAMS-D-15-00308.1.

[69] V. Masson, W. Heldens, E. Bocher, M. Bonhomme, B. Bucher, C. Burmeister, C. de Munck, T. Esch, J. Hidalgo, F. Kanani-Sühring, Y.-T. Kwok, A. Lemonsu, J.-P. Lévy, B. Maronga, D. Pavlik, G. Petit, L. See, R. Schoetter, N. Tornay, A. Votsis, J. Zeidler, City-descriptive input data for urban climate models: Model requirements, data sources and challenges, Urban Clim. 31 (2020) 100536. https://doi.org/10.1016/j.uclim.2019.100536.

[70] N.H. Wong, Y. He, N.S. Nguyen, S.V. Raghavan, M. Martin, D.J.C. Hii, Z. Yu, J. Deng, An integrated multiscale urban microclimate model for the urban thermal environment, Urban Clim. 35 (2021) 100730. https://doi.org/10.1016/j.uclim.2020.100730.

[71] M. Tewari, H. Kusaka, F. Chen, W.J. Coirier, S. Kim, A.A. Wyszogrodzki, T.T. Warner, Impact of coupling a microscale computational fluid dynamics model with a mesoscale model on urban scale contaminant transport and dispersion, Atmospheric Res. 96 (2010) 656–664. https://doi.org/10.1016/j.atmosres.2010.01.006.

[72] M. Mortezazadeh, Z. Jandaghian, L.L. Wang, Integrating CityFFD and WRF for modeling urban microclimate under heatwaves, Sustain. Cities Soc. 66 (2021) 102670. https://doi.org/10.1016/j.scs.2020.102670.

[73] O. Coceal, S.E. Belcher, WRF ground_A canopy model of mean winds through urban areas, Q. J. R. Meteorol. Soc. 130 (2004) 1349–1372. https://doi.org/10.1256/qj.03.40.

[74] J. Wang, L. (Leon) Wang, R. You, Evaluating a combined WRF and CityFFD method for calculating urban wind distributions, Build. Environ. 234 (2023) 110205. https://doi.org/10.1016/j.buildenv.2023.110205.

[75] A. Ricci, M. Burlando, M.P. Repetto, B. Blocken, Simulation of urban boundary and canopy layer flows in port areas induced by different marine boundary layer inflow conditions, Sci. Total Environ. 670 (2019) 876–892. https://doi.org/10.1016/j.scitotenv.2019.03.230.

[76] L. Peng, J.-P. Liu, Y. Wang, P. Chan, T. Lee, F. Peng, M. Wong, Y. Li, Wind weakening in a dense high-rise city due to over nearly five decades of urbanization, Build. Environ. 138 (2018) 207–220. https://doi.org/10.1016/j.buildenv.2018.04.037.

[77] A. Awol, G. Bitsuamlak, F. Tariku, A new analytical model for wind flow in canopies, J. Wind Eng. Ind. Aerodyn. 225 (2022) 105003. https://doi.org/10.1016/j.jweia.2022.105003.

[78] X.I.A. Yang, J. Sadique, R. Mittal, C. Meneveau, Exponential roughness layer and analytical model for turbulent boundary layer flow over rectangular-prism roughness elements, J. Fluid Mech. 789 (2016) 127–165. https://doi.org/10.1017/jfm.2015.687.

[79] N. Ikegaya, Momentum-Flux Determination for Boundary Layers with Sufficient Fetch Based on Integral Equations, Bound.-Layer Meteorol. 182 (2022) 225–250. https://doi.org/10.1007/s10546-021-00651-z.

[80] V. Yakhot, S.A. Orszag, Renormalization group analysis of turbulence. I. Basic theory, J. Sci. Comput. 1 (1986) 3–51. https://doi.org/10.1007/BF01061452.

[81] F. Menter, Zonal Two Equation k-w Turbulence Models For Aerodynamic Flows, in: 23rd Fluid Dyn. Plasmadynamics Lasers Conf., American Institute of Aeronautics and Astronautics, 1993. https://doi.org/10.2514/6.1993-2906.

[82] B. Devolder, P. Troch, P. Rauwoens, Performance of a buoyancy-modified k-ω and k-ω SST turbulence model for simulating wave breaking under regular waves using

OpenFOAM®, Coast. Eng. 138 (2018) 49–65. https://doi.org/10.1016/j.coastaleng.2018.04.011.

[83] A.F. Melaku, G.T. Bitsuamlak, A divergence-free inflow turbulence generator using spectral representation method for large-eddy simulation of ABL flows, J. Wind Eng. Ind. Aerodyn. 212 (2021) 104580. https://doi.org/10.1016/j.jweia.2021.104580.

[84] OpenFOAM: User Guide: Smagorinsky, (n.d.). https://www.openfoam.com/documentation/guides/latest/doc/guide-turbulence-les-smagorinsky.html#sec-turbulence-les-smagorinsky-model-equations (accessed October 4, 2023).

[85] S. Jayanti, Computational Fluid Dynamics for Engineers and Scientists, Springer Netherlands, Dordrecht, 2018. https://doi.org/10.1007/978-94-024-1217-8.

[86] S.M. Salim, R. Buccolieri, A. Chan, S. Di Sabatino, Numerical simulation of atmospheric pollutant dispersion in an urban street canyon: Comparison between RANS and LES, J. Wind Eng. Ind. Aerodyn. 99 (2011) 103–113. https://doi.org/10.1016/j.jweia.2010.12.002.

[87] RapidCFD, (2023). https://github.com/SimFlowCFD/RapidCFD-dev (accessed October 11, 2023).

[88] R.F. Warming, R.M. Beam, Upwind Second-Order Difference Schemes and Applications in Aerodynamic Flows, AIAA J. 14 (1976) 1241–1249. https://doi.org/10.2514/3.61457.

[89] R.I. Issa, Solution of the implicitly discretised fluid flow equations by operator-splitting, J. Comput. Phys. 62 (1986) 40–65. https://doi.org/10.1016/0021-9991(86)90099-9.

[90] The Finite Volume Method in Computational Fluid Dynamics: An Advanced Introduction with OpenFOAM® and Matlab | SpringerLink, (n.d.). https://link.springer.com/book/10.1007/978-3-319-16874-6 (accessed July 1, 2024).

[91] E. Robertson, V. Choudhury, S. Bhushan, D.K. Walters, Validation of OpenFOAM numerical methods and turbulence models for incompressible bluff body flows, Comput. Fluids 123 (2015) 122–145. https://doi.org/10.1016/j.compfluid.2015.09.010.

[92] P. Gousseau, B. Blocken, T. Stathopoulos, G.J.F. van Heijst, Near-field pollutant dispersion in an actual urban area: Analysis of the mass transport mechanism by high-resolution Large Eddy Simulations, Comput. Fluids 114 (2015) 151–162. https://doi.org/10.1016/j.compfluid.2015.02.018.

[93] T. Dai, S. Liu, J. Liu, N. Jiang, W. Liu, Q. Chen, Evaluation of fast fluid dynamics with different turbulence models for predicting outdoor airflow and pollutant dispersion, Sustain. Cities Soc. 77 (2022) 103583. https://doi.org/10.1016/j.scs.2021.103583.

[94] M.S. Thordal, J.Chr. Bennetsen, H.H.H. Koss, Review for practical application of CFD for the determination of wind load on high-rise buildings, J. Wind Eng. Ind. Aerodyn. 186 (2019) 155–168. https://doi.org/10.1016/j.jweia.2018.12.019.

[95] W. Zuo, Q. Chen, Real-time or faster-than-real-time simulation of airflow in buildings, Indoor Air 19 (2009) 33–44. https://doi.org/10.1111/j.1600-0668.2008.00559.x.

[96] Guidebook for CFD Predictions of Urban Wind Environment, (n.d.). https://www.aij.or.jp/jpn/publish/cfdguide/index_e.htm.

[97] J. Franke, A. Hellsten, H. Schlünzen, B. Carissimo, Best practice guideline for the CFD simulation of flows in the urban environment, COST European Cooperation in Science and Technology, 2007. https://hal.science/hal-04181390 (accessed October 10, 2023).

[98] P.J. Richards, R.P. Hoxey, Appropriate boundary conditions for computational wind engineering models using the k-ϵ turbulence model, J. Wind Eng. Ind. Aerodyn. 46–47 (1993) 145–153. https://doi.org/10.1016/0167-6105(93)90124-7.

[99] B.E. Launder, D.B. Spalding, The numerical computation of turbulent flows, Comput. Methods Appl. Mech. Eng. 3 (1974) 269–289. https://doi.org/10.1016/0045-7825(74)90029-2.

[100] H.G. Weller, G. Tabor, H. Jasak, C. Fureby, A tensorial approach to computational continuum mechanics using object-oriented techniques, Comput. Phys. 12 (1998) 620–631. https://doi.org/10.1063/1.168744.

[101] A.V. Barve, S. Sahu, K. Anupindi, Effect of co-flow velocity ratio on evolution of poly-disperse particles in coaxial turbulent jets: A large-eddy simulation study, Phys. Fluids 32 (2020) 093303. https://doi.org/10.1063/5.0017663.

[102] R.N. Meroney, Guidelines for fluid modeling of dense gas cloud dispersion, J. Hazard. Mater. 17 (1987) 23–46. https://doi.org/10.1016/0304-3894(87)85040-9.

[103] H. Jia, H. Kikumoto, Partially averaged Navier-Stokes simulation of flow around an isolated building model with a 1:1:2 shape, Build. Environ. 223 (2022) 109506. https://doi.org/10.1016/j.buildenv.2022.109506.

[104] Farzad Bazdidi-Tehrani, Dariush Bodaghi, Mohsen Kiamansouri, Large eddy simulation of flow and pollutant dispersion in a street canyon: analysis of performance of various inflow turbulence generation techniques, Environ. Fluid Mech. 23 (2023) 1283–1312. https://doi.org/10.1007/s10652-023-09944-y.

[105] M. Mortezazadeh, L. (Leon) Wang, An adaptive time-stepping semi-Lagrangian method for incompressible flows, Numer. Heat Transf. Part B Fundam. 75 (2019). https://doi.org/10.1080/10407790.2019.1591860.

[106] Z. Wangda, C. Qingyan, Improvements on the fast fluid dynamic model for indoor airflow simulation, Proc. SimBuild 4 (2010) 539–546.

[107] M. Mortezazadeh, L.L. Wang, M. Albettar, S. Yang, CityFFD – City fast fluid dynamics for urban microclimate simulations on graphics processing units, Urban Clim. 41 (2022) 101063. https://doi.org/10.1016/j.uclim.2021.101063.

[108] S. Zheng, Z.J. Zhai, Y. Wang, Y. Xue, L. Duanmu, W. Liu, Evaluation and comparison of various fast fluid dynamics modeling methods for predicting airflow around buildings, Build. Simul. 15 (2022) 1083–1095. https://doi.org/10.1007/s12273-021-0860-1.

[109] M. Mortezazadeh, L.L. Wang, A high-order backward forward sweep interpolating algorithm for semi-Lagrangian method, Int. J. Numer. Methods Fluids 84 (2017) 584–597. https://doi.org/10.1002/fld.4362.

[110] M. Mortezazadeh, L. (Leon) Wang, Solving city and building microclimates by fast fluid dynamics with large timesteps and coarse meshes, Build. Environ. 179 (2020) 106955. https://doi.org/10.1016/j.buildenv.2020.106955.

[111] R. Li, Z. Liu, L. Feng, N. Gao, Fast fluid dynamics simulation of the airflow distributions in urban residential areas, Energy Build. 255 (2022) 111635. https://doi.org/10.1016/j.enbuild.2021.111635.

[112] M. Mortezazadeh, L. (Leon) Wang, SLAC – a semi-Lagrangian artificial compressibility solver for steady-state incompressible flows, Int. J. Numer. Methods Heat Amp Fluid Flow 29 (2019) 1965–1983. https://doi.org/10.1108/HFF-05-2018-0181.

[113] J. Smagorinsky, General circulation experiments with the primitive equations: i. The basic experiment, Mon. Weather Rev. 91 (1963) 99–164. https://doi.org/10.1175/1520-0493(1963)091<0099:GCEWTP>2.3.CO;2.

[114] Z. Jandaghian, H. Akbari, Effects of increasing surface reflectivity on aerosol, radiation, and cloud interactions in the urban atmosphere, Theor. Appl. Climatol. 139 (2020) 873–892. https://doi.org/10.1007/s00704-019-03006-4.

[115] Z. Jandaghian, A.G. Touchaei, H. Akbari, Sensitivity analysis of physical parameterizations in WRF for urban climate simulations and heat island mitigation in Montreal, Urban Clim. 24 (2018) 577–599. https://doi.org/10.1016/j.uclim.2017.10.004.

[116] User's Guide for the Advanced Research WRF (ARW) Modeling System Version 4.0, (n.d.). https://www2.mmm.ucar.edu/wrf/users/docs/user_guide_v4/v4.0/contents.html.

[117] National Centers for Environmental Prediction/National Weather Service/NOAA/U.S. Department of Commerce. 2015, updated daily. NCEP GDAS/FNL 0.25 Degree Global Tropospheric Analyses and Forecast Grids. Research Data Archive at the National Center for Atmospheric Research, Computational and Information Systems Laboratory., (n.d.). https://doi.org/10.5065/D65Q4T4Z.

[118] M.B. Ek, K.E. Mitchell, Y. Lin, E. Rogers, P. Grunmann, V. Koren, G. Gayno, J.D. Tarpley, Implementation of Noah land surface model advances in the National Centers for Environmental Prediction operational mesoscale Eta model, J. Geophys. Res. Atmospheres 108 (2003). https://doi.org/10.1029/2002JD003296.

[119] F. Chen, H. Kusaka, R. Bornstein, J. Ching, C.S.B. Grimmond, S. Grossman-Clarke, T. Loridan, K. Manning, A. Martilli, S. Miao, D. Sailor, F. Salamanca, H. Taha, M. Tewari, X. Wang, A. Wyszogrodzki, C. Zhang, The Integrated WRF/Urban Modeling System: Development, Evaluation, and Applications to Urban Environmental Problems, Mech. Mater. Eng. Fac. Publ. Present. (2011). https://pdxscholar.library.pdx.edu/mengin_fac/45.

[120] Z.I. Janjić, The Step-Mountain Eta Coordinate Model: Further Developments of the Convection, Viscous Sublayer, and Turbulence Closure Schemes, (1994). https://journals.ametsoc.org/view/journals/mwre/122/5/1520-0493_1994_122_0927_tsmecm_2_0_co_2.xml (accessed January 15, 2025).

[121] Y.-L. Lin, R.D. Farley, H.D. Orville, Bulk Parameterization of the Snow Field in a Cloud Model, (1983). https://journals.ametsoc.org/view/journals/apme/22/6/1520-0450_1983_022_1065_bpotsf_2_0_co_2.xml (accessed February 4, 2025).

[122] G.A. Grell, D. Dévényi, A generalized approach to parameterizing convection combining ensemble and data assimilation techniques, Geophys. Res. Lett. 29 (2002) 38-1-38–4. https://doi.org/10.1029/2002GL015311.

[123] M.J. Iacono, J.S. Delamere, E.J. Mlawer, M.W. Shephard, S.A. Clough, W.D. Collins, Radiative forcing by long-lived greenhouse gases: Calculations with the AER radiative transfer models, J. Geophys. Res. Atmospheres 113 (2008). https://doi.org/10.1029/2008JD009944.

[124] H. Kris, B. Oscar, M. Alberto, M. Ardeshir, Implications of employing detailed urban canopy parameters for mesoscale climate modelling: a comparison between WUDAPT and GIS databases over Vienna, Austria, Int. J. Climatol. (2018). https://doi.org/10.1002/joc.5447.

[125] N. Luo, X. Luo, M. Mortezazadeh, M. Albettar, W. Zhang, D. Zhan, L. (Leon) Wang, T. Hong, A data schema for exchanging information between urban building energy models and urban microclimate models in coupled simulations, J. Build. Perform. Simul. 0 (2022) 1–18. https://doi.org/10.1080/19401493.2022.2142295.

[126] Hong Kong 2011 Population Census—Summary Results, The Goveronment of the Hong Kong Administrative Region, Hong Kong, 2011.

[127] CADMAPPER., (n.d.). https://cadmapper.com/. (accessed September 10, 2024).

[128] K. An, S.-M. Wong, J.C.-H. Fung, E. Ng, Revisit of prevailing practice guidelines and investigation of topographical treatment techniques in CFD-Based air ventilation assessments, Build. Environ. 169 (2020) 106580. https://doi.org/10.1016/j.buildenv.2019.106580.

[129] G. Rosatti, R. Chemotti, L. Bonaventura, High order interpolation methods for semi-Lagrangian models of mobile-bed hydrodynamics on Cartesian grids with cut cells, Int. J. Numer. Methods Fluids 47 (2005) 1269–1275. https://doi.org/10.1002/fld.910.

[130] B. Blocken, Computational Fluid Dynamics for urban physics: Importance, scales, possibilities, limitations and ten tips and tricks towards accurate and reliable simulations, Build. Environ. 91 (2015) 219–245. https://doi.org/10.1016/j.buildenv.2015.02.015.

[131] K.H. Schlünzen, D. Grawe, S.I. Bohnenstengel, I. Schlüter, R. Koppmann, Joint modelling of obstacle induced and mesoscale changes—Current limits and challenges, J. Wind Eng. Ind. Aerodyn. 99 (2011) 217–225. https://doi.org/10.1016/j.jweia.2011.01.009.

[132] K.-H. Kwak, S.-H. Lee, J.M. Seo, S.-B. Park, J.-J. Baik, Relationship between rooftop and on-road concentrations of traffic-related pollutants in a busy street canyon: Ambient wind effects, Environ. Pollut. 208 (2016) 185–197. https://doi.org/10.1016/j.envpol.2015.07.030.

[133] Y. Gao, Z. Wang, C. Liu, Z.-R. Peng, Assessing neighborhood air pollution exposure and its relationship with the urban form, Build. Environ. 155 (2019) 15–24. https://doi.org/10.1016/j.buildenv.2018.12.044.

[134] J. Bear, Dynamics of Fluids in Porous Media, Courier Corporation, 2013.

[135] Q. Bucquet, I. Calmet, L. Perret, M. Maché, Large-eddy simulation of the urban boundary layer using drag-porosity modeling, J. Wind Eng. Ind. Aerodyn. 238 (2023) 105432. https://doi.org/10.1016/j.jweia.2023.105432.

[136] J. Hang, Y. Li, Macroscopic simulations of turbulent flows through high-rise building arrays using a porous turbulence model, Build. Environ. 49 (2012) 41–54. https://doi.org/10.1016/j.buildenv.2011.09.013.

[137] A. Berger, An introduction to boundary layer meteorology.

[138] R. Mellis, W.N. Gill, G. Belfort, Fluid dynamics in a turbular membrane: theory and experiment, Chem. Eng. Commun. 122 (1993) 103–125. https://doi.org/10.1080/00986449308936152.

[139] T. Wei, Z. Li, Y. Wang, New momentum integral equation applicable to boundary layer flows under arbitrary pressure gradients, J. Fluid Mech. 984 (2024) A64. https://doi.org/10.1017/jfm.2024.207.

[140] F.H. Clauser, The Turbulent Boundary Layer, (n.d.).

[141] H. Cheng, I.P. Castro, Near Wall Flow over Urban-like Roughness, Bound.-Layer Meteorol. 104 (2002) 229–259. https://doi.org/10.1023/A:1016060103448.

[142] Y.-K. Ho, C.-H. Liu, M.S. Wong, Preliminary study of the parameterisation of street-level ventilation in idealised two-dimensional simulations, Build. Environ. 89 (2015) 345–355. https://doi.org/10.1016/j.buildenv.2015.02.042.

[143] G. Brearley, C. McAlpine, S. Bell, A. Bradley, Influence of urban edges on stress in an arboreal mammal: a case study of squirrel gliders in southeast Queensland, Australia, Landsc. Ecol. 27 (2012) 1407–1419. https://doi.org/10.1007/s10980-012-9790-8.

[144] J. Hang, Y. Li, Wind conditions in idealized building clusters: macroscopic simulations using a porous turbulence model, Bound.-Layer Meteorol. 136 (2010) 129–159. https://doi.org/10.1007/s10546-010-9490-3.

[145] J.O. Duguid, P.C.Y. Lee, Flow in fractured porous media, Water Resour. Res. 13 (1977) 558–566. https://doi.org/10.1029/WR013i003p00558.

[146] H. Darcy, Recherches expérimentales relatives au mouvement de l’eau dans les tuyaux, Mallet - Bachelier, 1857.

[147] A. Lenci, F. Zeighami, V. Di Federico, Effective Forchheimer Coefficient for Layered Porous Media, Transp. Porous Media 144 (2022) 459–480. https://doi.org/10.1007/s11242-022-01815-2.

[148] P.M. Adler, J.-F. Thovert, V.V. Mourzenko, Fractured Porous Media, Oxford University Press, 2012. https://doi.org/10.1093/acprof:oso/9780199666515.001.0001.

[149] S.P. Burke, W.B. Plummer, Gas Flow through Packed Columns, Ind. Eng. Chem. 20 (1928) 1196–1200. https://doi.org/10.1021/ie50227a025.

[150] J. Wang, R. You, Evaluating different categories of turbulence models for calculating air pollutant dispersion in street canyons with generic and real urban layouts, J. Wind Eng. Ind. Aerodyn. 255 (2024) 105948. https://doi.org/10.1016/j.jweia.2024.105948.

[151] Cap. 123G Building (Private Streets and Access Roads) Regulations, (n.d.). https://www.elegislation.gov.hk/hk/cap123G!en?xpid=ID_1438402649235_001&INDEX_CS=N (accessed October 14, 2024).

[152] T. Gál, J. Unger, Detection of ventilation paths using high-resolution roughness parameter mapping in a large urban area, Build. Environ. 44 (2009) 198–206. https://doi.org/10.1016/j.buildenv.2008.02.008.

[153] N.S. Darmanto, A.C.G. Varquez, M. Kanda, Urban roughness parameters estimation from globally available datasets for mesoscale modeling in megacities, Urban Clim. 21 (2017) 243–261. https://doi.org/10.1016/j.uclim.2017.07.001.

[154] B.S. Sützl, G.G. Rooney, M. van Reeuwijk, Drag Distribution in Idealized Heterogeneous Urban Environments, Bound.-Layer Meteorol. 178 (2021) 225–248. https://doi.org/10.1007/s10546-020-00567-0.

[155] J. Hang, X. Wang, J. Liang, X. Zhang, L. Wu, Y. Du, Y. Zhang, R. Buccolieri, Numerical investigation of the impact of urban trees on O3–NOx–VOCs chemistry and pollutant

dispersion in a typical street canyon, Atmos. Environ. 311 (2023) 119998. https://doi.org/10.1016/j.atmosenv.2023.119998.

[156] OpenFOAM v7, (n.d.). https://openfoam.org/version/7/.

[157] L. Yao, C.-H. Liu, G.P. Brasseur, C.Y.H. Chao, Winds and eddy dynamics in the urban canopy layer over a city: A parameterization based on the mixing-layer analogy, Build. Environ. 246 (2023) 110962. https://doi.org/10.1016/j.buildenv.2023.110962.

[158] R.W. Macdonald, Modelling The Mean Velocity Profile In The Urban Canopy Layer, Bound.-Layer Meteorol. 97 (2000) 25–45. https://doi.org/10.1023/A:1002785830512.